

Doctoral thesis

Doctoral theses at NTNU, 2023:377

Jessica Gaucherand

Direct Numerical Simulation of premixed ammonia/hydrogen flames: the effects of thermo-diffusive instabilities.

NTNU
Norwegian University of Science and Technology
Thesis for the Degree of
Philosophiae Doctor
Faculty of Engineering
Department of Energy and Process Engineering



Norwegian University of
Science and Technology

Jessica Gaucherand

Direct Numerical Simulation of premixed ammonia/hydrogen flames: the effects of thermo-diffusive instabilities.

Thesis for the Degree of Philosophiae Doctor

Trondheim, November 2023

Norwegian University of Science and Technology
Faculty of Engineering
Department of Energy and Process Engineering



Norwegian University of
Science and Technology

NTNU

Norwegian University of Science and Technology

Thesis for the Degree of Philosophiae Doctor

Faculty of Engineering

Department of Energy and Process Engineering

© Jessica Gaucherand

ISBN 978-82-326-7454-1 (printed ver.)

ISBN 978-82-326-7453-4 (electronic ver.)

ISSN 1503-8181 (printed ver.)

ISSN 2703-8084 (online ver.)

Doctoral theses at NTNU, 2023:377

Printed by NTNU Grafisk senter

Preface

This doctoral thesis is carried out at the Norwegian University of Science and Technology (NTNU), as well as at the Centre Européen de Recherche et de Formation Avancée en Calcul Scientifique (CERFACS) under the supervision of Associate Professor Corinna Schulze-Netzer, Professor Terese Løvås, Professor Thierry Poinsot and Associate Professor David Emberson.

This thesis is submitted to the Norwegian University of Science and Technology (NTNU) for partial fulfillment of the requirements for the degree of philosophiae doctor. The research works are conducted within the Low Emission Research Center, performed under the Norwegian research program PETROSENTER.

UNINET Sigma2 and NTNU HPC Group provided high-performance computational resources for CFD simulations. Further computational resources were provided by CERFACS in Toulouse and using HPC resources of GENCI-TGCC.

Abstract

In order to phase out traditional fuel from the energy mix to reduce CO₂ emissions and meet the large energy demand, the combustion of carbon-free fuels needs to be considered. This thesis investigates the combustion of premixed ammonia/hydrogen mixtures in order to gain insights into their fundamental structure. In particular, the work focuses on 1) dispersion relation in the linear phase as an indicator of thermo-diffusive instabilities propensity and 2) turbulence interaction with flames which are thermo-diffusively unstable. This work is performed numerically through Direct Numerical Simulations using the CFD code AVBP.

Different mixture ratios of ammonia to hydrogen in the fuels are investigated, as well as different equivalence ratios, with a focus on lean conditions. The initial pressure and temperature imposed focus mostly on atmospheric conditions. The work aims to investigate the fundamental properties of the combustion of these carbon-free fuels, to develop models for simulations of combustion processes, and to gain insights into what to expect in experimental or industrial apparatus. Preferential diffusion of light hydrogen atoms is seen to have a great impact in ammonia/hydrogen premixed flames, leading to instabilities, super adiabaticity, higher flame speed and heat release rate.

Acknowledgement

I would like to express my sincere gratitude to my supervisors, Corinna Schulze-Netzer, Thierry Poinso, David Emberson and Terese Løvås. Terese, along with David, provided me with an incredible opportunity by choosing me for this work. The flexibility and autonomy you granted me throughout my Ph.D. allowed me to explore a wide range of topics, from various numerical tools to a (very) short time in the lab. I am immensely thankful to you for the knowledge and skills I have acquired during these three years, all while being guided to follow this ever-so-important “red line”. Terese and Corinna, your unwavering support has been indispensable to me. You have consistently guided my work, offering support, advice, assistance, and meticulous reviews. I am truly grateful for the trust you have placed in me, your kindness and your expertise. I cannot adequately express my gratitude for having you as my supervisors.

To Thierry Poinso, I am immensely grateful that you received me at CERFACS and then guided me through three papers. Your availability, expertise, and insights have been invaluable resources, and I am sincerely grateful for your support. I would also like to thank Davide Laera for your assistance, help, reviews, and advice throughout this work, even after your departure to Italy.

I would also like to thank the opponents, Carmen Jiménez and Ossi Kaario, for assessing my thesis work.

To the Comkin team, both old and new members, I want to express my gratitude for the sense of belonging I felt at Gløshaugen. Despite the challenging circumstances of starting a Ph.D. during COVID, the time I spent with you was always a pleasant one. Every moment was a delightful mix of enriching discussions, laughter, and, of course, the occasional indulgence in cake. Special thanks to Michal for your

help with SRM simulations and CONVERGE. I extend my heartfelt thanks to Karl Oskar, Ning, Jingyuan, David Zilles, Keivan, Eva-Maria, Krister, Tian, Shivang, and Olav. I would also like to mention Bima, with whom I had the pleasure of sharing an office during the first month of my Ph.D., thank you for your kindness and for the chocolates. I would also like to express my thanks to Andrea Grubber for your valuable advice. A special thank you goes to Eilif Pedersen for your guidance and teachings on bond graphs. I take pride in the work that was produced from these teachings. My gratitude also extends to Eugen Uthaug and the IT team of EPT for their assistance throughout these three years. I am grateful to the administrative team at EPT for helping me throughout my time in Norway and for facilitating my relocation back to France.

On the Toulouse side, I extend my sincere thanks to Victor Coulon. Working with you was a pleasure, and I am grateful to have had this opportunity. Thank you for the work on Paper 1 of this thesis. I would also like to acknowledge Victor Xing for your support on Paper 1, and Corentin Lapeyre for your contribution to this work. Alexandre Coudray also provided great help when I arrived, handing over some of the work on ammonia done during his internship. Thank you for the help, especially with Cantera and Arcane. A special mention goes to Jean-Jacques Hok and Nicolas Detomaso for the insightful discussions, which greatly aided the redaction of Paper 2. Gabriel Staffelbach and Olivier Vermorel provided invaluable assistance with AVBP, your help was greatly appreciated. To the remarkable CSG team of CERFACS, I cannot emphasize enough my appreciation for your reliability and expertise in IT support. To Isabelle, Fabrice, Nicolas, Gérard, Fred, and Patrick, thank you. I would also like to express my gratitude to the colleagues with whom I shared the E0 office. Antony, Alexis, and especially Ilan, Justin, and Hector. Our interactions blended fun and seriousness. Crossed fingers that our podcast "Instability and Turbulence" will someday come out. To the people at CERFACS with whom I shared countless lunches, enjoyed some chocolates, solved crossword puzzles, and enjoyed some after-work, thank you for creating such a pleasant atmosphere at CERFACS. To the guys from the internship: Clément, Yann, Jean-Jacques, Jean, and Benjamin (though you joined us later), thank you. To those I had the pleasure to meet during my second time in CERFACS in 2021, Antoine, Thomas Naess, Alexandre Dukta, Eloïse, Francis, Loïc, Raphaël,

Guillaume, Lukas, Pierre-Antoine, Arthur, Felicia, Marcos, Yoann, Remi, Nathanael, Patrick, Eric, Yecine, Louis, and everyone else – I extend my heartfelt thanks. I am also grateful for the administrative team at CERFACS, whose assistance in various capacities ensured the smooth operation of this journey.

I would also like to extend my gratitude to my professors from the University of Orléans, especially to Alain Charlet and others who have inspired me to pursue a Ph.D. in the field of combustion. A special mention goes to Pierre Brequigny and Christine Rousselle, it was always a pleasure to cross paths during conferences. Thank you for your guidance and support, even beyond my time at the University of Orléans.

To my friends from Toulouse, Marseille, Orléans, and Luleå, I want to express my appreciation for your presence in my life. Your friendship has formed an invaluable support system upon which I can always rely. I sincerely wish all of you the very best.

To my family, my sister Béatrice and my brother Gabriel, thank you. To my parents, Pierre and Maya, I cannot thank you enough. Your support, encouragement, and dedication to teaching your children the values of hard work, perseverance, and kindness have been inspiring. I am forever grateful to have you in my life.

Finally, to Mehdi. Throughout these three years, you have been an unwavering source of support. I am immensely grateful for your presence in my life, your belief in my abilities -especially when it is hard to believe in myself-, your reminders not to be too dramatic, and the help you provided whenever I needed it. Thank you for the journey we share together.

Publications

This thesis is based on the following selected joint papers:

- Paper 1: Victor Coulon, Jessica Gaucherand, Victor Xing, Davide Laera, Corentin Lapeyre, Thierry Poinso (2023). *Direct Numerical Simulation of methane, ammonia-hydrogen and hydrogen turbulent premixed flames*, Combustion and Flame, Vol. 256, Page 112933.
- Paper 2: Jessica Gaucherand, Davide Laera, Corinna Schulze-Netzer, Thierry Poinso (2023). *Intrinsic instabilities of hydrogen and hydrogen/ammonia premixed flames: influence of equivalence ratio, fuel composition and pressure.*, Combustion and Flame, Vol. 256, Page 112986.
- Paper 3: Jessica Gaucherand, Davide Laera, Corinna Schulze-Netzer, Thierry Poinso (2023). *DNS of turbulent premixed ammonia/hydrogen flames: the effects of thermo-diffusive instabilities.*, submitted to Flow, Turbulence and Combustion, under review.

Additional publication

- Jessica Gaucherand, Michal Lewandowski, Corinna Netzer, Terese Løvås (2022), *Modelling of liquid injection of ammonia in a direct injector using Reynolds-averaged Navier–Stokes simulation (paper and presentation)*, 63rd International Conference of Scandinavian Simulation Society, 20-21 September, Trondheim (Published in proceedings), DOI: <https://doi.org/10.3384/ecp192058>.
- Jessica Gaucherand, Eilif Pedersen, Corinna Netzer, Terese Løvås (2023), *Modelling of a solenoid injector for internal combustion engines and simu-*

lation using the bond graph methodology (paper), WCX SAE, 18-20 April, Detroit (Published in proceedings), DOI: <https://doi.org/10.4271/2023-01-0195>.

Conference contributions

- Jessica Gaucherand, Michal Lewandowski, Corinna Netzer, Terese Løvås (2021). *Emission prediction for low-carbon fuels in marine applications using detailed chemistry with stochastic reactor model (Poster and unpublished paper)*, 10th European Combustion Meeting, 14-15 April 2021, Online.
- Jessica Gaucherand, Victor Coulon, Victor Xing, Davide Laera, Corentin Lapeyre, Thierry Poinso, Corinna Netzer, Terese Løvås (2022), *Direct numerical simulation of a premixed turbulent ammonia/hydrogen-air flame in a slot burner configuration (presentation)*, 2nd Low Carbon conference, 5-6 April 2022, Cambridge.
- Jessica Gaucherand, Victor Coulon, Davide Laera, Thierry Poinso, Corinna Netzer, Terese Løvås (2023), *Direct numerical simulation of premixed turbulent ammonia/hydrogen-air flames (Poster and unpublished paper)*, 11th European Combustion Meeting, 26 -28 April 2023, Rouen.
- Jessica Gaucherand, Davide Laera, Corinna Netzer, Thierry Poinso(2023), *Intrinsic instabilities of hydrogen and hydrogen/ammonia premixed flames: influence of equivalence ratio, fuel composition and pressure. (presentation)*, 2nd Symposium on Ammonia Energy, 11-13 July 2023, Orléans.

Contents

Preface	i
Abstract	iii
Acknowledgement	v
Publications	ix
Nomenclature	xv
Abbreviations	xix
List of Figures	xxi
List of Tables	xxiii
1 Introduction	1
1.1 Ammonia for decarbonization	1
1.2 Research questions and thesis outline	5

2	Fundamentals	9
2.1	Turbulence	9
2.2	Premixed flames	10
2.2.1	Equivalence ratio	11
2.2.2	Diffusion of species and heat	12
2.2.3	Lewis number	13
2.2.4	Stretch definitions	14
2.3	Turbulence and chemistry interaction	15
2.4	Intrinsic instabilities in premixed flames	17
3	Computational tools	23
3.1	Governing equations	23
3.2	Numerical simulation for combustion	27
3.3	One-dimensional premixed flames	30
3.3.1	Unstrained flames	30
3.3.2	Strained flames	31
3.4	Stretch effects in premixed flame modeling	32
3.5	Direct Numerical Simulation	33
3.6	DNS resolution requirements	34
3.7	DNS solver	35
3.8	Numerical method	35
3.8.1	Time marching method	37
3.8.2	Cell-vertex convection schemes	38
3.8.3	Cell-vertex diffusion schemes	39

3.9	Boundary conditions	40
4	DNS specificities	41
4.1	Grid specificities in the simulations	41
4.2	Chemical mechanism scheme reduction and validation	42
4.3	Numerical methods	46
4.4	Boundary conditions	46
5	Summary of papers	49
5.1	Paper I: Direct Numerical Simulation of methane, ammonia-hydrogen and hydrogen turbulent premixed flames	50
5.2	Paper II: Intrinsic instabilities of hydrogen and hydrogen/ammonia premixed flames: influence of equivalence ratio, fuel composition and pressure.	53
5.3	Paper III: DNS of turbulent premixed ammonia/hydrogen flames: the effects of thermo-diffusive instabilities.	55
6	Conclusions and outlook	59
	Bibliography	63
	Bibliography	63
	Paper I	81
	Paper II	123
	Paper III	151

Nomenclature

D_k	Diffusion coefficient of k
Da	Damköler number
E	Total energy
Ka	Karlowitz number
Le	Lewis number
Ma	Markstein number
P	Pressure
Pr	Prandtl number
R	Perfect gas constant
Re	Reynolds number
Re_t	Turbulent Reynolds number
Sc	Schmidt number
T	Temperature
T_{ad}	Adiabatic temperature
W	Molecular weight

X	Molar fraction
Y	Mass fraction
Σ	Flame surface density
δ_D	Diffusion thickness
δ_L^0	Thermal thickness
δ_{ij}	Kronecker delta
$\dot{\omega}_T$	Heat release rate
$\dot{\omega}_k$	Species k reaction rate
ϵ	Dissipation
μ	Dynamic viscosity
ν	Kinematic viscosity
ϕ	Equivalence ratio
ρ	Density
τ_{ij}	Viscous tensor
\mathbf{q}	Heat flux vector
h	Enthalpy
k	Kinetic energy
l_η	Kolmogorov scales
l_t	Integral scales
s_L^0	Laminar flame speed
t	Time
u	Velocity

u' Turbulent intensity
 x Spatial coordinate

Abbreviations

CFD Computational Fluid Dynamics.

CFL Courant-Friedrich-Lewy.

DL Darrieus-Landau.

DNS Direct Numerical Simulations.

EGR Exhaust gas recirculation.

ICE Internal Combustion Engine.

LES Large Eddy Simulation.

LHV Lower Heating Value.

LW Lax-Wendroff.

MPI Message passing interface.

NSCBC Navier-Stokes Characteristic Boundary Condition.

PGS Pressure Gradient Scaling.

RANS Reynold-Averaged Navier-Stokes.

TTGC Two-step Taylor Galerkin.

List of Figures

1.1	Vision of the "Ammonia Economy" from MacFarlane et al. [1] with permission from Elsevier, license number 5578090702602.	2
2.1	Turbulence energy spectrum as a function of wave numbers κ	10
2.2	Borghi-Peters diagram for premixed turbulent combustion regimes.	16
2.3	Deviation of flow lines due to density jump between fresh and burned gases leading to hydrodynamic instability.	19
2.4	Streamline of light diffusing species focusing on convex flame zone toward burned mixture, leading to thermo-diffusive instabilities.	20
3.1	Turbulence and chemistry treatment trade-off in numerical tools.	28
3.2	Principle of the DNS, LES and RANS approaches. Adapted from [2].	29
3.3	A one-dimensional laminar flame, where reactant mass fraction, temperature and heat release rate have been normalized.	30
3.4	Cell vertex method: black dots are the node, the cell center is in white and the cell is colored in pink.	37

4.1	Scheme validation for the NH_3/H_2 blends for the laminar flame speed. Numerical data from CRECK [3] (detailed), and reduced ARC mechanism against experiment from Koroll et al. [4], Law et al. [5], Vagelopoulos et al. [6], Dowdy et al. [7], Kumar et al. [8], Zhou et al. [9], Han et al. [10], and Lhuillier et al. [11].	44
4.2	Scheme validation for the NH_3/H_2 blends for the adiabatic temperature. Numerical data from CRECK [3] (detailed) against reduced ARC mechanism.	45
5.1	Isosurfaces of $c = c^*$, extracted after two flow-through times $t = 2\tau$ and colored by heat release rate normalized by the maximum value in the corresponding 1-D unstretched laminar flame for all cases. Methane case at $c_{\text{CH}_4}^* = 0.72$ (left), ammonia/hydrogen case at $c_{\text{H}_2\text{O}}^* = 0.8$ (center), hydrogen case at $c_{\text{H}_2}^* = 0.85$ (right). .	51
5.2	Dispersion relation for varying equivalence ratio, at various NH_3 contents in volume in the fuel. Symbols correspond to the growth rates extracted from the simulations, dashed lines correspond to the second-order polynomial fit of these growth rates. The theoretical hydrodynamic growth rate $\omega_{DL}\tau$ is also shown in solid line for all blends.	54
5.3	Normalized heat release rate after two flow-through times with the corresponding joint probability density function of the quantity conditioned by the progress variable $c_{\text{H}_2\text{O}}$ for the four cases. A lighter shade in the colormap represents a greater probability of the PDF. The dashed line corresponds to the 1-D unstretched laminar flames and the solid line corresponds to the conditional mean of the quantity versus progress variable.	56

List of Tables

1.1 Ammonia properties and comparison with other fuels from [11] and [12].	3
---	---

Chapter 1

Introduction

1.1 Ammonia for decarbonization

Combustion currently plays a central role in global energy production as the main source of energy worldwide, accounting for 80 % of energy production [13, 14], generated from sources such as coal, gas, oil, biomass, ... Combustion is used to generate energy using the chemical bond energy stored in various fuels. It finds applications both in industry and private use in aeronautics, road transport, sea transport, stationary power generation, industrial application, heating, and so on. However, the impact of combustion on climate change needs to be considered and alternative power generation with lower CO₂ productions must become part of the energy mix to mitigate its negative impact [15]. Nonetheless, the adoption of complete electrification across all energy systems faces challenges regarding energy storage produced from renewable sources and the volumetric constraints of materials like batteries, especially when replacing large-scale combustion systems like marine engines. Process heat applications such as metallurgy, cement production or glass melting require chemical bond breaking possible through combustion but not through electrification as of now. Due to its major contribution to meeting the energy demand, and its irreplaceability in some domains, combustion is not expected to be phased out of existence. Therefore, in order to reduce CO₂ in combustion processes, the investigation of carbon-free fuels has been at the center of research topics in recent years [16, 17, 18].

Alternative fuels, such as ammonia (NH₃), can be used as an energy vector and

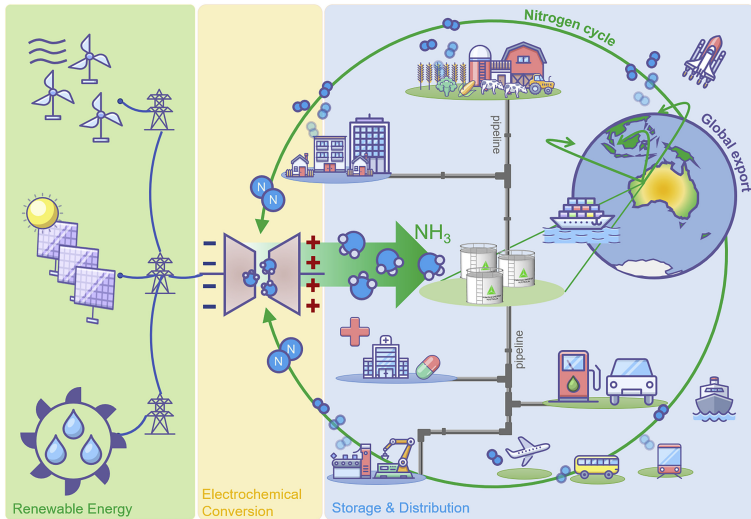


Figure 1.1: Vision of the "Ammonia Economy" from MacFarlane et al. [1] with permission from Elsevier, license number 5578090702602.

does not contain carbon atoms, a crucial aspect to transition combustion from fossil fuels (hydrocarbon-based) towards carbon-free fuels. As of today, ammonia is most commonly produced through the Haber-Bosch process, where hydrogen is combined with nitrogen from the air, and the two form ammonia. Hydrogen is not found in Earth's atmosphere but is found in nature combined with other molecules such as water or hydrocarbons. Therefore, using hydrogen first requires extracting it from another gas, typically methane. Furthermore, the process requires a large amount of energy, often provided by fossil fuel-powered systems. However, other technologies to extract hydrogen are in development, such as water electrolysis [19], production from fossil fuels coupled with carbon capture storage [20], and methane pyrolysis [21]. Therefore, ammonia has the potential to be an efficient electro-fuel (e-fuel), which could come from renewable hydrogen produced through water electrolysis. In this scenario, the energy needed to electrolyze water could come from renewable energy such as wind or solar power in times when there would be a surplus of energy production (Fig. 1.1) to limit the CO₂ produced during ammonia production.

Ammonia as a fuel has proven its feasibility. A historical example dates from the Second World War when a fleet of Belgian buses ran on ammonia due to gasoline

shortages. However, ammonia was then put aside as a fuel and has since been widely used as a fertilizer. In recent years, research on ammonia to power vehicles has resurfaced. For example, in Korea, the AmVeh, an ammonia-gasoline fueled car prototype fueled with 70 % of ammonia [22], was developed. Similarly, at the University of Michigan, a pick-up truck operating with up to 80 % ammonia was developed [23].

Table 1.1 shows the advantages and challenges of ammonia compared to other fuels in order to explore its combustion characteristics.

	Hydrogen	Methane	Gasoline	Ammonia
Boiling temperature 1 atm (°C)	-253	-161	-42.1	-33.4
Condensation pressure at 25 °C (atm)	N/A	N/A	9.4	9.9
Lower heating value LHV (MJ/kg)	120	50	46.4	18.6
Air/fuel ratio at stoichiometry (-)	34.2	17.65	14.6	6.06
Flammability limits (Equivalence ratio)	0.1-7.1	0.5-1.7	0.5-2.5	0.63-1.4
Adiabatic flame temperature (°C)	2110	1950	2000	1800
Maximum laminar burning velocity (m/s)	2.91	0.37	0.43	0.07
Maximum auto ignition temperature (°C)	520	630	450	650
Octane number (-)	>120	120	88-98	>120

Table 1.1: Ammonia properties and comparison with other fuels from [11] and [12].

Storage at ambient temperature is possible in liquid form for ammonia, making it easily transportable in similar conditions as gasoline. Ammonia’s low range of flammability limits is a safety benefit that mitigates the risk of fire and explosion in case of leakage. However, as a fuel, ammonia presents several drawbacks. It has a low heat of combustion and slow laminar burning velocity which are unfavorable combustion properties. The narrow flammability range is both a safety benefit and a drawback for ammonia ignition when an excess of air or of fuel is introduced in a combustion system. Despite these drawbacks, the advantages of ammonia in terms of greenhouse gas and as a hydrogen carrier make it compelling to pursue the study of ammonia as a fuel for engines, turbines and burners.

Strategies such as pilot injection, turbocharging, ignition systems, increased compression ratio, or hydrogen addition take advantage of ammonia properties and enhance ammonia flames. Ammonia’s high ignition temperature makes it a poor candidate for auto-ignited engines or needs to be compensated by high compres-

sion ratios in compression-ignited engines. Large engines with a high compression ratio (above 35:1) [24], such as those for power generation or marine applications, make ammonia a potential fuel for these applications. For compression ignition engines of lower compression ratios, dual-fuel utilization with ammonia rates of up to 95 % can be found in the literature [25]. Multiple injections strategy is a potential solution to reduce NO_x and unburned ammonia for compression ignition engines [26]. The high octane number of ammonia reduces the risk of knocking, an advantage for spark-ignition engines. Ammonia for spark-ignition engines enables to counter ammonia's high auto-ignition property: chambers with a compression ratio of 10:1 are sufficient to burn ammonia at full load [27]. Work on ammonia for gas turbines is also carried out [28, 29] finding efficient performance with exhaust gas recirculation and preheating, as well as for industrial burners [30]. In order to retrofit already existing infrastructure, comparing ammonia with methane flame is relevant as methane flame behavior can be considered an objective for ammonia flames to be a suitable fuel. Compared to methane/air flames, ammonia/air flames are less stable, and have a lower laminar burning velocity, heat release rate, flame temperatures, and extinction stretch rates. Enhancing ammonia flames is, therefore, necessary, which can be done with the help of promoters [12, 31] such as hydrogen.

Hydrogen can be obtained by cracking ammonia before combustion, to avoid supplementary storage for hydrogen and conserving the fuel's carbon-free nature. The unstretched laminar burning velocity of ammonia/hydrogen flames increases with the addition of hydrogen, burning performances of ammonia are improved, and burning velocity can reach a similar value to methane/air flames with a hydrogen proportion of 40 % in volume at the stoichiometry, and NO_x emissions are reduced [32]. Other studies have shown the benefits of adding hydrogen to enhance the combustion of ammonia in both internal combustion engines, gas turbines, and burners [33, 34, 35, 36, 37, 38, 39, 40, 41, 42, 43].

Premixed flame is a term used to describe a mixture that is ignited after the fuel and air have been mixed, and investigation of premixed ammonia/hydrogen flames remains a scarce topic in the literature, especially regarding their fundamental flame structure. Both laminar (when the fluid is not disturbed by vortices) and turbulent flows (when the fluid is comprised of vortices that counteract each other) are relev-

ant to study, as they appear in combustion apparatus. The work done in this thesis can benefit internal combustion engines, gas turbine applications and industrial furnace design. It also informs on safety scenarios and consequences, especially for hydrogen, where leaking of this odorless and colorless very flammable gas could have grave consequences. Understanding the combustion of such gases can support the design of combustion systems, highlight retrofitting needs, and ensure safe storage and distribution facilities. In this work, the fundamental aspects of the combustion of ammonia/hydrogen flames are investigated using numerical tools, focusing on laminar and turbulent flows to provide a better understanding of the intrinsic instabilities of these flames.

1.2 Research questions and thesis outline

In this work, both laminar and turbulent premixed ammonia/hydrogen flames are investigated. In premixed lean flames, a concern is the development of intrinsic instabilities such as hydrodynamic or thermo-diffusive instabilities. These instabilities may be beneficial, increasing mixing and burning rate, but may also lead to damage and failure. For example, for ICEs, Oppong et al. [44] warned against higher risks of explosion due to increased pressure and temperature due to the flames' intrinsic instabilities. For burners and gas turbines [45, 46, 47], the stability of the flame is an important parameter to control the combustion, and for explosion scenarios [48, 49], the understanding of the impact of instabilities on the flame propagation must be considered for satisfactory safety measures to be taken. Furthermore, for combustion modeling, the impact of the intrinsic instabilities should be accounted for, and insights from experiments or Direct Numerical Simulations can inform the development of these models. Therefore, the main research question that is investigated in this thesis is the following:

How does thermo-diffusive instability develop and impact ammonia/hydrogen flames in laminar and turbulent premixed flames?

Indeed, lean hydrogen flames are known to exhibit thermo-diffusive instabilities: these are intrinsic instabilities due to the fast diffusion of light species. The question of thermo-diffusive instabilities in ammonia/hydrogen blends is an open one and several behaviors might be expected as ammonia does not diffuse the same

way as hydrogen does. Hydrogen in the fuel blend could control the flame behavior and a hydrogen/ammonia flame may behave like a pure hydrogen one. A second hypothesis may be that the opposite behavior occurs where ammonia dominates the flame front behavior and the flame behaves like a pure ammonia flame. Third, it might be that ammonia dissociates into hydrogen, and ammonia/hydrogen flames become more unstable than pure hydrogen flames at the same equivalence ratio. Finally, it might be that ammonia addition dampens the intrinsic thermo-diffusive instabilities. [Paper 2 and 3]

Other research questions accompany this main one. First, the flame characteristic of ammonia/hydrogen compared to other fuels is relevant. In order to investigate this, a turbulent premixed ammonia/hydrogen fuel is compared with a turbulent premixed methane flame, and a pure hydrogen one. The turbulence intensity is kept the same for these three flames in order to perform this comparison and investigate the fuel nature, which requires tuning the equivalence ratio and mixture to keep the same laminar flame speed. [Paper 1]

The question of the definition of a suited progress variable for ammonia/hydrogen blends is relevant. As will be seen later, the progress variable is important to define the combustion state, and describe the flame evolution from unburned to burned gas and is at the core of many combustion models. Progress variable based on the fuel species is commonly used. In the case of a fuel blend, the progress variable may be defined by the fuel or by a combustion product. Progress variables may also be based on the temperature or other properties of the flame. The progress variable definition is investigated in this thesis in regard to ammonia/hydrogen mixtures. [Paper 3]

Similarly, the effective Lewis number definition of ammonia/hydrogen blends is an open question that this thesis targets. Indeed, the Lewis number is often needed for theoretical models, but in the case of a mixture, the question of which Lewis number definition should be used is an open one that has scarcely been investigated [50]. Three typical definitions of a mixture-weighted Lewis number have been proposed in the literature and are investigated in this thesis in regard to ammonia/hydrogen mixtures. [Paper 2]

Thermo-diffusive instabilities will be shown to have a strong impact on the flame

structure and consumption speed, especially in turbulent cases. This is captured in the Direct Numerical Simulation performed, but needs to be accounted for in LES modeling in combustion models. The question of the modeling implication that thermo-diffusive instabilities entail is also investigated with tools suggested based on the DNS database to identify where ammonia/hydrogen flames will exhibit thermo-diffusive instabilities and which correction should be applied to the flame speed to account for their impact. [Papers 1, 2 and 3]

Finally, an objective of this thesis work is to increase the database of DNS of ammonia/hydrogen premixed flames and to share them. Indeed, the large computational expense DNS requires the user's responsibility to share those data for other users to perform their own research. For example, in the work performed in this thesis, the impact of pollutant emission was not investigated. However, the data to investigate these pollutants and notably NO_x are available in the database created and can be shared for other groups to perform their research on the topic. Furthermore, DNS data for machine learning-related methods have been emerging, and the availability and sharing of databases such as the one generated in this thesis could be used for this purpose [51, 52]. [Papers 1, 2 and 3]

This manuscript summarizes the work carried out on combustion with Direct Numerical Simulations during this thesis to answer the previously detailed research questions. Chapter 2 introduces fundamental concepts about turbulence and premixed flame structures and definitions and concepts about intrinsic flame instabilities. Chapter 3 presents the governing equation for numerical combustion, the existing numerical tools, the benefit of DNS, the grid requirements for DNS computation, and the numerical schemes and boundary conditions needed in simulations. Chapter 4 details the specificity of the simulations performed in Chapter 5, justifying choices on the grid resolution chosen, the chemical mechanism, and other details on how the simulations were set up. Chapter 5 introduces the paper collection that constitutes the work performed by the author and collaborators in regard to this thesis work. Three papers are presented: one on the intrinsic instability of lean premixed laminar ammonia/hydrogen flames and their dispersion relation, and two papers on lean turbulent premixed flames, the first of these papers investigates three different fuels (methane, pure hydrogen, and an ammonia/hydrogen blend), while the second paper investigates four blends of ammonia/hydrogen at

different fuel content and equivalence ratio.

Chapter 2

Fundamentals

This Chapter first introduces fundamental notions on turbulence, then on premixed flames, presenting definitions. Then, turbulent combustion regimes are presented. Finally, notions and definitions of intrinsic instabilities are introduced. The equations were taken from Poinso and Veynante [2], unless stated otherwise.

2.1 Turbulence

Turbulence has been extensively investigated for reacting and non-reacting flows [53, 54, 55]. Turbulent flows are characterized by the Reynolds number:

$$Re = \frac{uL}{\nu}, \quad (2.1)$$

with u the flow velocity, L the characteristic size of the flow, and ν the kinematic viscosity. For small values of Re , the flow is laminar, whereas for high Reynolds numbers, swirls are created that deviate from the mean flow. These swirls are called turbulent eddies. Turbulence involves a continuous spectrum of different scales of eddies from the largest eddies, depending on the topology of the flow, down to the smallest eddies that dissipate into energy, a theory formalized by Kolmogorov [56]. The break up of the largest eddies into smaller ones and so on is called the energy cascade (Fig. 2.1). The largest scales due to the largest eddies are called the integral length scale l_t and are characteristic of the flow size, and the smallest ones are called the Kolmogorov length scales η_k . The largest scales are controlled by inertia only, and viscous dissipation dominates the inertial effect as the eddies get smaller, and an equilibrium is reached between inertial and dissip-

ative flux. The energy flux flowing from the large scales to the smallest scales is constant along the scales and is given by the dissipation of the kinetic energy:

$$\epsilon = \frac{k^{3/2}}{l_t}, \quad (2.2)$$

where ϵ is the dissipation, and k the kinetic energy. The energy cascade of the energy spectrum as a function of the wave number is illustrated in Fig. 2.1. The turbulent kinetic energy is the contribution of the energy spectrum over all the wave numbers. Most of the turbulent kinetic energy is contained in the integral scales, and in the inertial subrange, the energy cascade evolves proportionally to $\kappa^{-5/3}$ [53]. In the viscous, or dissipative range, the turbulent eddies are characterized by the Kolmogorov length $\eta_k = (\nu^3/\epsilon)^{1/4}$, time $\tau_\eta = (\nu/\epsilon)^{1/2}$ and velocity $u_\eta = (\nu\epsilon)^{1/4}$.

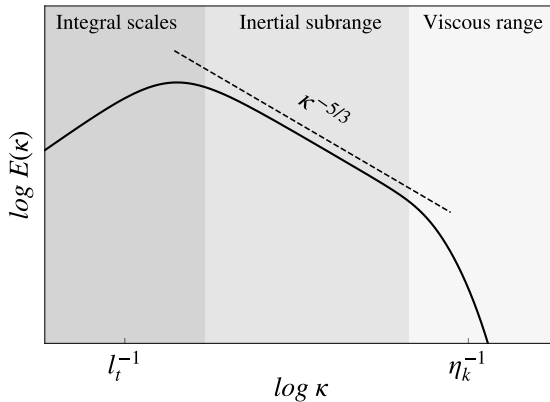


Figure 2.1: Turbulence energy spectrum as a function of wave numbers κ .

2.2 Premixed flames

In this section, gaseous premixed combustion is discussed, which is where the reactants (fuel and oxidizer) are fully premixed before combustion. During the combustion of premixed gases, a flame front separates burned and unburned gases. This flame front has a thickness (δ), which definitions will be discussed later, and a flame speed, (s_L^0), which is the speed at which the flame front propagates normal to itself towards the unburned mixture [57], and is called the laminar flame speed. Definitions of the laminar flame speed will also be provided in a later section.

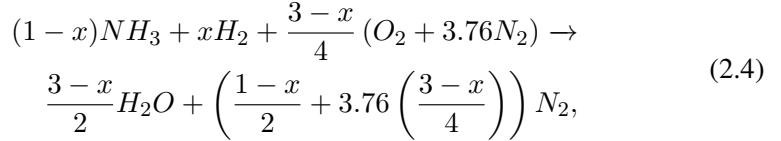
The temperature increases from the temperature of the unburned mixture until it reaches the adiabatic flame temperature (T_{ad}) in the burned gases where the equilibrium composition has been reached as the fuel has been fully consumed. In the flame front, high reaction rates are reached. The laminar flame speed can be derived, assuming complete combustion, from a balance equation between unburned and burned gases: the mass entering the flame front at speed s_L^0 needs to be burnt within the flame front of thickness δ :

$$\rho s_L^0 = \dot{\omega} \delta, \quad (2.3)$$

where $\dot{\omega}$ is the reaction rate [58], which will be defined later. Definitions are needed to describe the combustion of premixed flames, which are presented in this section.

2.2.1 Equivalence ratio

An important parameter to characterize a flame is the equivalence ratio, which indicates if the fuel is in excess or if the oxidizer is. To determine the stoichiometric ratio and the equivalence ratio of an ammonia/hydrogen fuel blend with air, the global reaction is written at stoichiometry, assuming complete combustion, as follows:



where $x = \frac{X_{H_2}}{X_{H_2} + X_{NH_3}}$ is the mole fraction of hydrogen in the fuel. In this case, we can calculate $s_{NH_3-X_2}$, the stoichiometric number of ammonia/hydrogen fuel blend:

$$s_{NH_3-X_2} = \frac{3-x}{4}. \quad (2.5)$$

The equivalence ratio of the fuel blend is defined as :

$$\phi = \frac{\frac{X_F}{X_O}}{\left(\frac{X_F}{X_O}\right)_{st}} = s \frac{X_F}{X_O} \quad (2.6)$$

If $\phi = 1$, the combustion process will be stoichiometric. If $\phi > 1$, there will be a rich combustion, and if $\phi < 1$, a lean combustion. Throughout this work, stoichiometric and lean conditions are considered, in order to be representative of most practical burners and limit soot, unburned fuels and NO_x emissions.

Although it is not used in Chapter 5, we can define the energy fraction of each fuel in the mixture using their Lower Heating Value (LHV) such as defined by Okafor et al. [59], using the mass fraction of species k , Y_k :

$$E_{H_2} = \frac{Y_{H_2} LHV_{H_2}}{Y_{H_2} LHV_{H_2} + Y_{NH_3} LHV_{NH_3}}. \quad (2.7)$$

The energy fraction is useful for understanding the energy share of the respective fuels to the total energy, which is typically more relevant for practical applications [60].

2.2.2 Diffusion of species and heat

Adimensional quantities need to be defined to characterize the interaction between the diffusion of momentum, species, and heat during combustion. The momentum rate of evolution is characterized by the kinematic viscosity ($\nu = \mu/\rho$), the species rate of evolution is characterized by the species diffusivity D_k , and the heat rate of evolution is characterized by the thermal diffusivity $\alpha = \lambda/(\rho c_p)$, the magnitude of each effect can be compared with the Prandtl number (Pr), the Schmidt number (Sc) and the Lewis number (Le).

$$Pr = \frac{\nu}{\alpha} = \frac{\mu c_p}{\lambda}, \quad (2.8)$$

compares the momentum and heat diffusion,

$$Sc = \frac{\nu}{D_k}, \quad (2.9)$$

compares the momentum and species diffusion, and finally,

$$Le = \frac{\alpha}{D_k} = \frac{\lambda}{\rho c_p D_k}, \quad (2.10)$$

compares the heat and species diffusion, and definitions for theoretical applications are detailed hereafter.

2.2.3 Lewis number

The Lewis number of a flame with a fuel typically defines the diffusivity of the fuel (the deficient reactant) into the mixture-averaged fresh gases. However, in the case of a fuel blend, the question of a fuel Lewis number definition is an open one, due to the presence of several deficient reactants. Several definitions have been suggested and validated against experiment [61, 62]. The three most common definitions are presented here. The first one (Le_V) was proposed by Muppala et al. [63], who suggested a volume-based formulation of the fuel's Lewis number (Le_V), based on the fuel volumetric, or mole fraction (X_i) of each fuel in the fuel blend:

$$Le_V = \sum_{n=1}^f X_i Le_i, \quad (2.11)$$

with f the number of fuels in the fuel blend. This was initially developed for fuel blends of CH_4/H_2 and $\text{C}_3\text{H}_8/\text{H}_2$ flames and tested for turbulent flame speed correlations. The formulation gave reasonable results between flame speed modeling and experimental data for low levels of turbulence, but not for high levels. Dinkelacker et al. [64] proposed a diffusion-based (Le_D) formula:

$$\frac{1}{Le_D} = \sum_{n=1}^f \frac{X_i}{Le_i}. \quad (2.12)$$

This definition was derived from the assumption of enrichment of the fastest diffusive fuel in the fuel blend into a positive curvature zone for CH_4/H_2 flames. Law et al. [65] used a heat release-based formulation (Le_Q), where the Lewis number of each fuel is weighted by the nondimensional heat release (q_i) based on the consumption of each fuel:

$$Le_Q = 1 + \frac{\sum_{n=1}^f q_i (Le_i - 1)}{\sum_{n=1}^f q_i}, \quad (2.13)$$

with

$$q_i = \frac{Q_i Y_{i,u}}{C_p T_u}, \quad (2.14)$$

where Q_i is the heat of reaction of the fuel i and $Y_{i,u}$ its mass fraction far upstream. This relation was derived from asymptotic analysis of $\text{C}_3\text{H}_8/\text{H}_2$ spherical

flames and was then commonly employed especially with regards to discussion on thermo-diffusive instabilities of hydrocarbons and hydrogen blends [64, 66].

There is no definitive conclusion as to which of the three definitions is most suited for hydrogen/ammonia blend. Zitouni et al. [50] carried out a theoretical and experimental investigation of this question and found that Le_V was most suited for a large range of equivalence ratio while Le_D was most suited for lean conditions. In the work realized in this thesis, these three definitions have been investigated numerically.

For premixed flames, theoretical relations and flame phenomenology requires not only the Lewis number but also definitions for the Lewis number of the fresh gases, called the effective Lewis number (Le_{eff}), defined by Joulin and Mitani [67] for two reactant flames. Le_{eff} is given by:

$$Le_{eff} = \begin{cases} \frac{Le_O + ALe_F}{1+A}, & A = 1 + \beta(\phi^{-1} - 1) \quad \text{if } \phi < 1, \\ \frac{Le_F + ALe_O}{1+A}, & A = 1 + \beta(\phi - 1) \quad \text{if } \phi > 1, \end{cases} \quad (2.15)$$

where Le_F and Le_O are the fuel's and oxidant's Lewis numbers. This provides an indicator of the diffusion of the overall mixture and how it is influenced by the equivalence ratio.

2.2.4 Stretch definitions

In describing the flame front in a flow, there is the need to define the stretch, as the flame structure can be affected by it. The total stretch of the flame K is defined as the sum of the tangential strain rate, K_s , and the curvature-induced propagation rate K_c [2]:

$$K = K_s + K_c, \quad (2.16)$$

$$K_c = \kappa s_d, \quad (2.17)$$

$$K_s = \nabla \cdot \mathbf{u} - \mathbf{n} \cdot \nabla \mathbf{u} \cdot \mathbf{n}, \quad (2.18)$$

where $\kappa = \nabla \cdot \mathbf{n}$ is the curvature, \mathbf{u} is the gas velocity and $\mathbf{n} = -\nabla c/|\nabla c|$ is the normal vector to the flame front pointing towards the fresh gases, where c is the progress variable. The progress variable describes the combustion progress and two constraints are imposed on the progress variable: a monotonous growth from fresh ($c = 0$) to burn gas ($c = 1$) to uniquely describe each thermochemical state, and the thermochemical variables should vary at a moderate speed with the progress variable, since, if not verified, it would mean a small deviation in c would result in large errors in the thermochemical variables. Regarding the curvature, positive elements are convex towards the burned mixture, and negative elements are concave towards the burned mixture. s_d is the displacement speed, which is the flame front speed relative to the flow [2, 68] $s_d = (\mathbf{w} - \mathbf{u}) \cdot \mathbf{n}$, or it can also be computed as:

$$s_d = \frac{1}{|\nabla c|} \left(\frac{\partial c}{\partial t} + \mathbf{u} \cdot \nabla c \right). \quad (2.19)$$

2.3 Turbulence and chemistry interaction

Combustion is, on its own, a complex process with various time scales and length scales involved, which leads to a complex description. Adding turbulent flow interaction to combustion leads to an even more complex process where turbulence strongly modifies the flame structure, and may enhance the flame's reactivity or quench it. Furthermore, turbulence is affected by combustion due to the heat release accelerating the flow, and the large change of viscosity due to the variation of temperature further modifying the turbulence.

Premixed turbulent combustion regimes are presented hereafter, in Fig. 2.2. The Borghi-Peters diagram [69] presents combustion regimes using two quantities:

- u'/s_L^0 where the turbulence intensity $u' = \sqrt{2k/3}$ represents the turnover velocity of the large eddies over the laminar flame speed,
- l_t/δ_L^0 represents the integral length scale over the thermal flame thickness.

Other quantities bounding the diagram are:

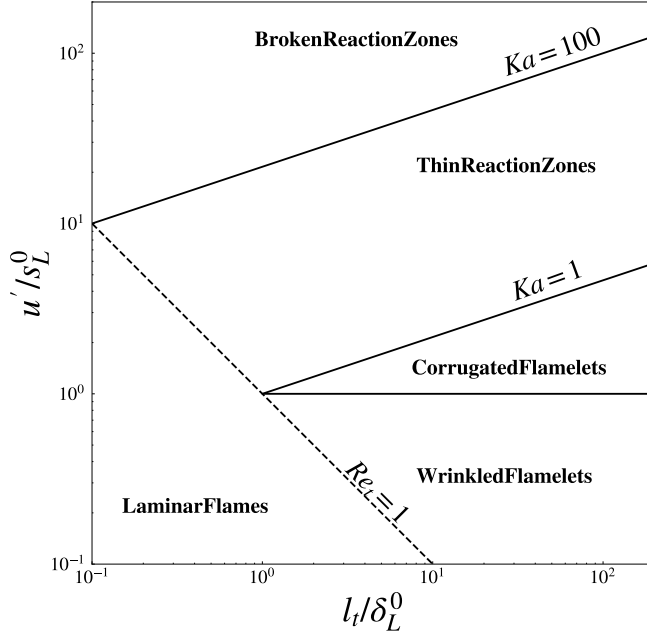


Figure 2.2: Borghi-Peters diagram for premixed turbulent combustion regimes.

- the turbulent Reynolds number:

$$Re_t = \frac{u'}{s_L^0} \frac{l_t}{\delta_L^0}, \quad (2.20)$$

- the Karlowitz number, which compares the flame time to the Kolmogorov time

$$Ka = \left(\frac{u'}{s_L^0} \right)^{3/2} \left(\frac{l_t}{\delta_L^0} \right)^{-1/2}. \quad (2.21)$$

The Borghi-Peters diagram serves as an indicator of the different regimes of turbulent combustion, but the boundaries are transition regions that should be interpreted with care [2, 57, 70, 71]. Five classifications are considered in the diagram:

- Laminar flame where $Re_t < 1$,
- Wrinkled flamelet where $u'/s_L^0 < 1$ and l_t/δ_L^0 is large, but the speed of the turbulent motions is too low to wrinkle the flame front: the flame propagation is driven by laminar burning rather than turbulent wrinkling,

- Corrugated flamelet regime, where $u' / s_L^0 > 1$ but below $Ka = 1$, where the turbulent motion velocities are higher than the flame speed and wrinkle the flame front. The smallest turbulent eddies are larger than the flame thickness and, therefore will not break into the flame front,
- The thin reaction zone, where Ka is between 1 and 100, and where turbulent motions are entering and modifying the flame preheat zone, but are still too large to modify the reaction zone,
- The broken reaction zone, where $Ka > 100$, where the smallest eddies of the turbulent motions are able to penetrate the inner reaction layer and disrupt the flame structure, no laminar structure can be identified.

2.4 Intrinsic instabilities in premixed flames

Concepts on intrinsic instabilities and state-of-the-art research on the topic of intrinsic instabilities in ammonia/hydrogen premixed flames are introduced hereafter. Instabilities may be beneficial to combustion systems, increasing mixing and burning rate, but may also lead to damage and failure of the combustion system. We concern ourselves with the intrinsic instabilities that are induced by the combustion process. Instabilities occurring as pressure fluctuations of acoustic nature occur in a combustion chamber are outside of the scope of this thesis work.

In the context of ICEs, Oppong et al. [44] highlight that instability leads to an increase of the flame surface as it becomes unstable, cells appear, and wrinkles form. They further indicate that the fuel is consumed faster and the mixing is improved, leading to improved efficiency. However, they highlight potential drawbacks, such as possible temperature increase and pressure caused by instabilities, that could increase the risk of explosion, knocking, or NO_x emissions. Other works have focused on intrinsic instabilities for burner applications [45], explosions scenarios [48], and in the context of gas turbine applications [47] all highlighting the importance of instabilities on the flame structure development.

In premixed flames, the intrinsic instabilities are due to two phenomena: hydrodynamic instabilities and thermo-diffusive (or diffusive-thermal as sometimes found in the literature) instabilities. Buoyancy instabilities due to gravity are also

present but not investigated here. Intrinsic instabilities are caused by the non-homogeneous flame speed that appears along a flame front due to the combustion dynamics itself and not by external influence. Hydrodynamic instability was discovered by Darrieus and Landau [72] (also called DL instabilities) and is illustrated in Fig. 2.3. The main concept is that the density jump from unburned to burned gases can destabilize the flame, leading to wrinkling of the flame front. The growth rate, which is obtained in the initial (or linear) phase of the flame is an indicator of the flame's response to a perturbation such as an instability, either growing or dampening the instability, is proportional to the thermal expansion (the density ratio of burned to unburned). The hydrodynamic instability ω_{DL} can be defined as:

$$\omega_{DL} = \frac{\sqrt{\sigma^3 + \sigma^2 - \sigma} - \sigma}{\sigma + 1}, \quad (2.22)$$

where $\sigma = \frac{\rho_u}{\rho_b}$ is the expansion ratio equal to unburned over burned density. The non-dimensional growth rate $\bar{\omega}$ dependency with respect to non-dimensional wave number \bar{k} can be written in a first estimation as:

$$\bar{\omega} = \omega_{DL} \bar{k}, \quad (2.23)$$

where $\bar{\omega} = \omega \tau$ and $\bar{k} = k \delta_L^0$. The flame time τ corresponds to the ratio of the flame thermal thickness δ_L^0 to the unstretched flame speed s_L^0 .

In the hydrodynamic instability mechanism, the flame front is considered to be infinitely thin and serves as an interface between burned and unburned gases, which have constant densities, respectively. If the flame front is perturbed (from a numerical or physical perturbation) it would result in the apparition of convex and concave parts towards the burned mixture along the flame front. The flow lines flowing from burned to unburned gases deviate, creating a flow divergence that leads to a velocity gradient. The flame front speed remains constant, but the unburned flow velocity near the flame front is affected, it increases in concave regions and decreases in convex regions. The increasing or decreasing velocity further increases the perturbation and the concave regions become increasingly concave and so do the convex regions. Eventually, the convex part disappears, the concave part flattens and the flame front divides into smaller cells. Darrieus-Landau instabilities

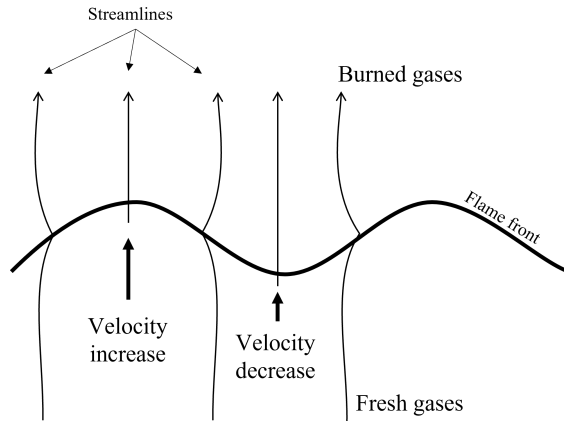


Figure 2.3: Deviation of flow lines due to density jump between fresh and burned gases leading to hydrodynamic instability.

are intrinsically unstable. However, planar flames and smooth cylindrical or spherical flames exist: this is due to the stabilizing effects induced by other instabilities such as buoyancy or thermo-diffusive instabilities.

Thermo-diffusive instabilities are caused by the preferential diffusion of mass versus heat: this is characterized by the aforementioned Lewis number. When the Lewis number is different from one, the thermal and molecular diffusivities individually influence the dynamics of the flame. A Lewis number higher than one leads to stable thermo-diffusive effects, while a Lewis number below one indicates an unstable effect of the flame. Figure 2.4 illustrates the streamline of species concentration leading to thermo-diffusive instabilities. A perturbed flame is concave and convex towards the burned mixture and leads to different concentrations of the reactant species, which will converge towards convex zones, while the heat conduction diverges from it: this leads to more reactant concentration and causes variation of equivalence ratio and flame speed, leading to instability.

Several parameters are then involved in the flame's intrinsic instability formation and evaluation: the density, the flame thickness, the Lewis number, the stretch (Markstein number and Karlowitz number), and the activation energy (or Zel'dovich number). Intrinsic instabilities can be investigated in the linear phase, where the instabilities start to develop, and in the nonlinear phase, where different scales in-

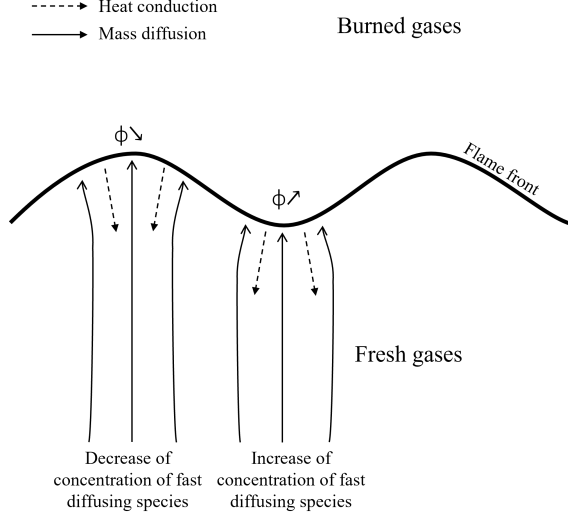


Figure 2.4: Streamline of light diffusing species focusing on convex flame zone toward burned mixture, leading to thermo-diffusive instabilities.

teract with one another and lead to more chaotic structure formation. In the linear phase, theoretical models aim to account for the stabilizing effects at large wave numbers:

- Matalon et al. [73] presented a theoretical model where a second-order term is added to account for a stabilizing -or destabilizing behavior due to Lewis number effects:

$$\bar{\omega} = \omega_{DL}\bar{k} - \delta [B_1 + \beta (Le_{eff} - 1) B_2 + P_r B_3] \bar{k}^2 = \omega_{DL}\bar{k} - \omega_2 \bar{k}^2. \quad (2.24)$$

The diffusive flame thickness δ_D , is needed to define $\delta = \delta_D/\delta_L^0$. The coefficients B_1 , B_2 , and B_3 are functions of the expansion ratio, the thermal conductivity evolution with temperature, and ω_{DL} [74]:

$$B_1 = \frac{\sigma}{2(\sigma + (\sigma + 1)\omega_{DL})} \left(\frac{\sigma(2\omega_{DL} + \sigma + 1)}{\sigma - 1} \int_1^\sigma \frac{\bar{\lambda}(x)}{x} dx + \int_1^\sigma \bar{\lambda}(x) dx \right), \quad (2.25)$$

$$B_2 = \frac{\sigma(1 + \omega_{DL})(\sigma + \omega_{DL})}{2(\sigma - 1)(\sigma + (\sigma + 1)\omega_{DL})} \int_1^\sigma \log\left(\frac{\sigma - 1}{x - 1}\right) \frac{\bar{\lambda}(x)}{x} dx, \quad (2.26)$$

$$B_3 = \frac{\sigma}{\sigma + (\sigma + 1)\omega_{DL}} \left((\sigma - 1)\bar{\lambda}(\sigma) - \int_1^\sigma \bar{\lambda}(x) dx \right), \quad (2.27)$$

where $\bar{\lambda} = \lambda/\lambda_u$ is the normalised thermal conductivity and $x = T/T_u$.

The Prandtl number P_r , the Zel'dovich number β , and the effective Lewis number Le_{eff} are also needed in Eq. (2.24). Zel'dovich number β for detailed chemistry is computed using the approach proposed by Law et al. [75] to evaluate the overall activation energy.

$$\frac{E_a}{R} = -2 \frac{d(\rho_u s_L^0)}{d(1/T_{ad})}, \quad (2.28)$$

where R is the universal gas constant. The Zel'dovich number β is given by:

$$\beta = \frac{E_a(T_{ad} - T_u)}{RT_{ad}^2}. \quad (2.29)$$

Matalon et al.'s dispersion relation Eq. (2.24) is derived for Lewis numbers close to unity, where the second term of the expression ω_2 has a stabilizing effect. However, for lower values of Lewis number, ω_2 is positive: the dispersion relation becomes destabilizing for all wave numbers.

- Sivashinsky [76, 77] derived a dispersion relation for the linear phase accounting for a fourth-order term that is stabilizing regardless of the Lewis number:

$$\bar{\omega} = \delta \left[\frac{\beta}{2}(1 - Le) - 1 \right] \bar{k}^2 - 4\delta^3 \bar{k}^4. \quad (2.30)$$

Hydrogen flames' intrinsic instabilities have been extensively investigated in the literature, where lean flames were found to be destabilized by thermo-diffusive phenomena, whereas rich and stoichiometric flames were found to be destabilized by DL instabilities [44, 78, 79, 80, 81, 82]. Hydrogen in turbulent flows also exhibited thermo-diffusive instabilities effect that led to faster flame consumption [83, 84, 85, 86]. Other studies of hydrogen mixed with different fuels have

been investigated, Vu et al. [87] investigated the addition of hydrocarbon on instabilities of syngas (H_2 and CO mixture), and found that heavy hydrocarbons such as propane and butane suppressed the instabilities whereas methane addition enhanced it. Reyes et al. [88] found that instabilities in methane/hydrogen premixed flame led to higher wrinkling and flame surface formation when more H_2 was added. These instabilities were controlled by DL instabilities at stoichiometry, whereas for the lean cases, the wrinkling and instabilities were due to thermo-diffusive instabilities. Smaller cell radii seem to appear for small methane content in the fuel, smaller even than for the pure H_2 . Okafor et al. [89] found in lean H_2/CH_4 blends that the flames became more unstable with increasing H_2 and pressure. The Markstein number as an indicator of the stretch influence on instabilities has been investigated by Okafor et al. [90] who found a non-monotonic evolution of the Markstein number with H_2 content, which also led to instability following this trend. However, the intrinsic instabilities of ammonia flames have scarcely been investigated. For methane/ammonia premixed flame, Okafor et al. [91] found the burned Markstein number increasing with equivalence ratio and ammonia concentration. Ichikawa et al. [92] investigated the Markstein number of ammonia/hydrogen flame, finding that the Markstein number evolved non-monotonically with hydrogen addition. Zitouni et al. [50] investigated both blends of ammonia with methane and hydrogen. They found a linear reduction in the stretch sensitivity as methane was added to ammonia, while a non-monotonous evolution of the Markstein length was found for ammonia/hydrogen blends as hydrogen content varied. This was shown to be the effect of thermo-diffusive instabilities, which affected the flame less strongly when stoichiometric conditions were reached. Netzer et al. [93] found preferential diffusion effects in ammonia/hydrogen flame leading to enrichment of convex curvature zone. In the globally lean mixture, in the enriched zone, NO concentration increased, while in a globally rich mixture, the NO concentration reduced in locally richer zones. Preferential diffusion was also found by Wiseman et al. [94] and Rieth et al. [86, 95] for ammonia/hydrogen turbulent premixed flame as the flame structure was investigated locally. In this work, insights into the intrinsic instabilities of ammonia/hydrogen are investigated, both in the context of laminar perturbed planar flames through computation of the dispersion relation, and in the context of turbulence-flame interaction.

Chapter 3

Computational tools

This Chapter introduces the governing equations, the benefits of numerical simulations, the specificities of one-dimensional flames, the specificities of Direct Numerical Combustion, and then information on the code used, including numerical method and boundary conditions.

3.1 Governing equations

The system of the equation used to describe a reactive, compressible, gaseous mixture of N chemical species is presented hereafter. The equations were taken from Poinso and Veynante [2], unless stated otherwise. We start with the species mass fraction Y_k , which is defined as the ratio of the species k over the total mass of the mixture.

$$\sum_{k=1}^N Y_k = 1, \quad (3.1)$$

indicates that the sum of all the species mass fractions is equal to 1. We can also compute the mole fraction of the species such as:

$$X_k = \frac{W}{W_k} Y_k, \quad (3.2)$$

where W_k is the atomic weight of species k , and W is the mean molecular weight of the mixture, given by:

$$\frac{1}{W} = \sum_{k=1}^N \frac{Y_k}{W_k}. \quad (3.3)$$

In this work, the fraction of ammonia and hydrogen are typically given in mole fraction, unless stated otherwise. The spatio-temporal evolution of the mixture is given by the Navier-Stokes equation, constituting by the conservation of mass, momentum, and energy:

$$\frac{\partial \rho}{\partial t} + \frac{\partial \rho u_i}{\partial x_i} = 0, \quad (3.4)$$

is the total mass conservation equation, where t is the time, \mathbf{x} the spatial coordinate, ρ is the density of the mixture, and \mathbf{u} is the velocity field.

$$\frac{\partial}{\partial t} \rho u_j + \frac{\partial}{\partial x_i} \rho u_i u_j = -\frac{\partial P}{\partial x_j} + \frac{\partial \tau_{ij}}{\partial x_i}, \quad (3.5)$$

is the momentum conservation equation where gravity forces are neglected, P is the fluid static pressure, τ_{ij} is the viscous tensor, and $\sigma_{ij} = \tau_{ij} - P\delta_{ij}$, δ_{ij} being the Kronecker delta ($\delta_{ij} = 1$ if $i = j$, and 0 otherwise). The species conservation law is:

$$\frac{\partial \rho Y_k}{\partial t} + \frac{\partial}{\partial x_i} \rho Y_k u_i = -\frac{\partial}{\partial x_i} J_{i,k} + \dot{\omega}_k, \quad (3.6)$$

where $\dot{\omega}_k$ is the mass production rate of species k , \mathbf{J}_k is the diffusive flux vector of species k .

The energy conservation equation is written as:

$$\frac{\partial \rho E}{\partial t} + \frac{\partial}{\partial x_j} \rho E u_j = -\frac{\partial}{\partial x_j} [u_i (P\delta_{ij} - \tau_{ij}) + q_j] + \dot{\omega}_T, \quad (3.7)$$

where E is the total energy per unit mass, \mathbf{q} is the heat flux vector, $\dot{\omega}_T$ is the heat release rate, and the radiative term is not considered here.

These equations are complemented by others, such as the equation of state: each gaseous species is assumed to behave like a perfect gas:

$$P_k = \rho Y_k \frac{R}{W_k} T, \quad (3.8)$$

where P_k is the partial pressure of species k , $R = 8.314 \text{ J}\cdot\text{mol}^{-1}\cdot\text{K}^{-1}$ is the perfect gas constant, and T is the temperature. The total thermodynamic pressure P is equal to the sum of the partial pressures:

$$P = \rho \frac{R}{W} T. \quad (3.9)$$

The viscous tensor τ_{ij} needed in Eq.(3.5) is defined as:

$$\tau_{ij} = -\frac{2}{3}\mu \frac{\partial u_k}{\partial x_k} \delta_{ij} + \mu \left(\frac{\partial u_i}{\partial x_j} + \frac{\partial u_j}{\partial x_i} \right), \quad (3.10)$$

where μ is the dynamic viscosity.

The species diffusion flux needed in Eq. (3.6) requires a more detailed definition.

$$\sum_{k=1}^N Y_k V_i^k = 0, \quad (3.11)$$

is implied by the total mass conservation of a multi-species flow, where V_i^k are the components in the three directions of the diffusion velocity of species k . The diffusion velocity is often expressed as a function of the species gradient, using the Hirschfelder Curtiss approximation [96]:

$$Y_k V_i^k = -D_k \frac{W_k}{W} \frac{\partial X_k}{\partial x_i}, \quad (3.12)$$

where X_k is the mole fraction, D_k is the diffusion coefficient of the species k into the rest of the mixture:

$$D_k = \frac{1 - Y_k}{\sum_{j=1, j \neq k}^N X_j / D_{k,j}}. \quad (3.13)$$

To ensure mass conservation, a correction diffusion velocity is needed \mathbf{V}^c :

$$\mathbf{V}^c = \sum_{k=1}^N D_k \frac{W_k}{W} \frac{\partial X_k}{\partial x_i}, \quad (3.14)$$

which is added to the convection velocity. This leads to the diffusive species flux:

$$J_{i,k} = -\rho \left(D_k \frac{W_k}{W} \frac{\partial X_k}{\partial x_i} - Y_k V_i^c \right). \quad (3.15)$$

The species production rate needed in Eq. (3.6) also requires a more detailed definition. The Arrhenius law models the combustion rate:

$$\sum_{k=1}^N \nu'_{km} \mathcal{M}_{km} \rightleftharpoons \sum_{k=1}^N \nu''_{km} \mathcal{M}_{km}, \quad m = 1, M \quad (3.16)$$

where M is the number of elementary chemical reaction, \mathcal{M}_k is the species k , and ν'_{km} and ν''_{km} are the stoichiometric coefficient of species k . The rate of progress of a single reaction should be proportional to the product of the reactant molar concentration X_k . The rate of progress of a reaction m is:

$$Q_m = K_{f,m} \prod_{k=1}^N [X_k]^{\nu'_{k,m}} - K_{r,m} \prod_{k=1}^N [X_k]^{\nu''_{k,m}}, \quad (3.17)$$

where $K_{f,m}$ and $K_{r,m}$ are the forward and reverse rates of reaction m given by the Arrhenius law:

$$K_{f,m} = A_{f,m} T^{\beta_m} \exp\left(\frac{E_{a,m}}{RT}\right), \quad (3.18)$$

where A is the pre- exponential constant, β_m the temperature exponent, and $E_{a,m}$ is the activation energy of the reaction m , which are all tabulated. Finally, the mass production rate of species k is:

$$\dot{\omega}_k = W_k \sum_{m=1}^M \nu_{k,m} Q_m, \quad (3.19)$$

with $\nu_{k,m} = \nu''_{km} - \nu'_{km}$ is the net stoichiometric coefficient of species k in reaction m .

The total energy, heat flux, and heat release rate in Eq. (3.7) requires to be defined more thoroughly, by first defining the species-specific enthalpy:

$$h_{s,k}(T) = \int_{T_0}^T c_{p,k} dT, \quad (3.20)$$

where $h_{s,k}$ is the species enthalpy changing as a function of temperature, $c_{p,k}$ is the species-specific heat capacity at constant pressure, and T_0 a reference temperature (usually 298 K). The enthalpy is tabulated. The specific sensible energies $e_{s,k}$:

$$e_{s,k} = h_{s,k} - \frac{RT}{W_k}, \quad (3.21)$$

and the specific sensible energy of the whole mixture is:

$$e_s = \sum_{k=1}^N e_{s,k} Y_k = \int_{T_0}^T c_p dT - \frac{RT}{W}. \quad (3.22)$$

The total energy E is the total specific non-chemical energy:

$$E = e_s + \frac{1}{2}u_i u_i, \quad (3.23)$$

which sums the specific sensible energy and the kinetic energy. The heat flux is due to the heat transport by species diffusion, derived using Fourier's law:

$$q_i = \underbrace{-\lambda \frac{\partial T}{\partial x_i}}_{\text{Heat conduction}} - \rho \underbrace{\sum_{k=1}^N \left(D_k \frac{W_k}{W} \frac{\partial X_k}{\partial x_i} - Y_k V_i^c \right) h_{s,k}}_{\text{Heat flux through species diffusion}} = -\lambda \frac{\partial T}{\partial x_i} + \sum_{k=1}^N J_{i,k} h_{s,k}, \quad (3.24)$$

where λ is the thermal conductivity. And the heat release $\dot{\omega}_T$ is the volumic heat released by the production and destruction of the species in the chemical reactions:

$$\dot{\omega}_T = - \sum_{k=1}^N \dot{\omega}_k \Delta h_{f,k}^0, \quad (3.25)$$

where $\Delta h_{f,k}^0$ is the mass enthalpy of formation of species k at the reference temperature T_0 .

3.2 Numerical simulation for combustion

Numerical tools in combustion research have become necessary to support the development of experimental apparatus and large-scale industrial combustors and engines. Numerical tools rely on mathematical concepts, physics, computer science, and programming. Parametric variations and design evaluations are possible in numerical simulations, which can be done rapidly without the need to manufacture new designs systematically. Numerical simulation also permits the fundamental understanding of phenomena. For example, post-treatment of 3-D simulations enables the extraction of information not captured through experiments, due to the constraints of measurement devices.

Turbulence is a complex physical process that is experienced by flows in some conditions involving a large range of different time scales and length scales [56, 57, 97], introduced in Chapter 2 which can be investigated numerically. Computational fluid dynamics, or CFD, solves the Navier-Stokes equation numerically and can be applied to reactive flows to describe their behavior. Different numerical tools exist which have various purposes depending on the level of turbulence

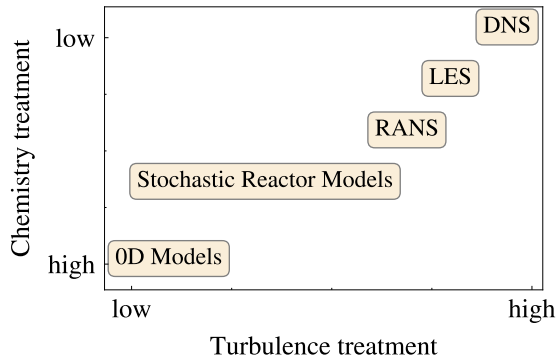
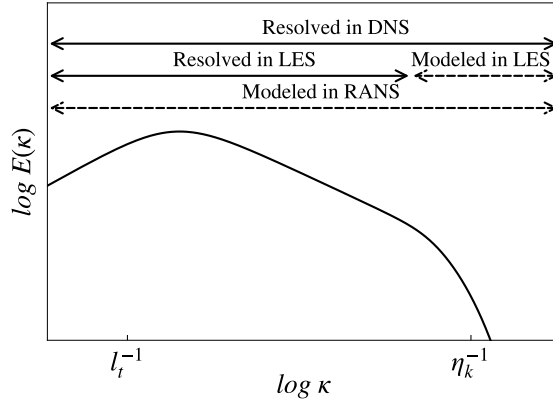


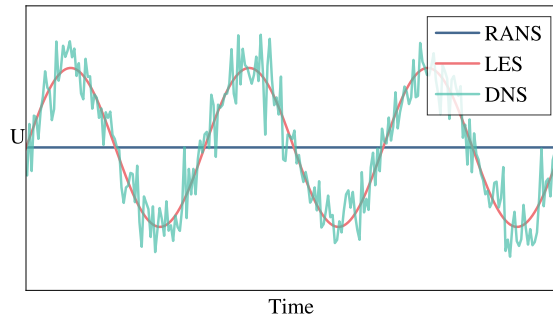
Figure 3.1: Turbulence and chemistry treatment trade-off in numerical tools.

and details of chemical reactions that need to be solved: with an increase of the turbulence treatment, a trade-off is needed with smaller chemistry schemes for the computational cost of the computations to be reasonable, illustrated Fig. 3.1 for the different tools which are described hereafter.

0-D or 1-D tools can be used for the parametric study of canonical ideal cases (i.e. constant pressure reactors, one-dimensional unstretched flames, and others). These 0-D and 1-D tools can utilize complex chemistry solving for hundreds of species and thousands of reactions. Stochastic Reactor Models, which belong to PDF methods, where the stochastic nature of flows is accounted for but using 0-D modeling treatment at its core, enable the use of detailed chemistry and account for the mixture's inhomogeneities while modeling turbulence using a simplified model. Figure 3.2 summarizes the three approaches to CFD (RANS, LES, DNS) with a schematic of the energy cascade and of the velocity time evolution. Reynolds-Averaged Navier Stokes (RANS) simulation can be used to compute two or three-dimensional flows when averaged information is needed. RANS equations are time-averaged equations of flow, which lead to unclosed quantities that require to be modeled. Common turbulence models include the $k - \epsilon$ model. Large Eddy Simulation (LES) can also be used to provide a small resolution, for two or three-dimension flows, especially when turbulence interacts with the flow. LES equations solve the large length scales of turbulence and model the smallest scales of the flow field by using a filter. Suitable subgrid-scale models in LES lead to a large range of applications to study complex geometries and capture instabil-



(a) Approaches with energy cascade



(b) Approaches with time evolution of velocity

Figure 3.2: Principle of the DNS, LES and RANS approaches. Adapted from [2].

ity phenomena. Finally, Direct Numerical Simulation (DNS) solves all scales of turbulence when multi-scales are involved but are limited to reduced chemistry.

The selection of the numerical tool modeling level (0-D, 1-D, PDF, RANS, LES, or DNS) depends on the phenomena investigated, the turbulent scale-solving requirements, the chemistry details needed, the geometry considered, and the computational resources available. A compromise between the level of physics that needs to be solved and the computational cost or memory available needs to be determined in order to select the most suited modeling tool. The allotted time to perform the simulation must also be considered in this choice. In this study, the fundamental combustion of ammonia/hydrogen blends is investigated, in both laminar and turbulent cases, and Direct Numerical Simulation is utilized. Therefore, only

the aspects relating to DNS will be described, although modeling implication in the LES framework is also important and a motivation to perform DNS and shall be briefly mentioned, although details of the framework will not be thoroughly presented.

3.3 One-dimensional premixed flames

Solvers such as Cantera [98] enable solving one-dimensional flames, strained and unstrained, to test theoretical relations and prepare the larger DNS computations. An overview of these flames' structure and definitions relating to them is presented hereafter.

3.3.1 Unstrained flames

A one-dimensional, freely propagating, or unstrained premixed laminar flame is illustrated in Fig. 3.3.

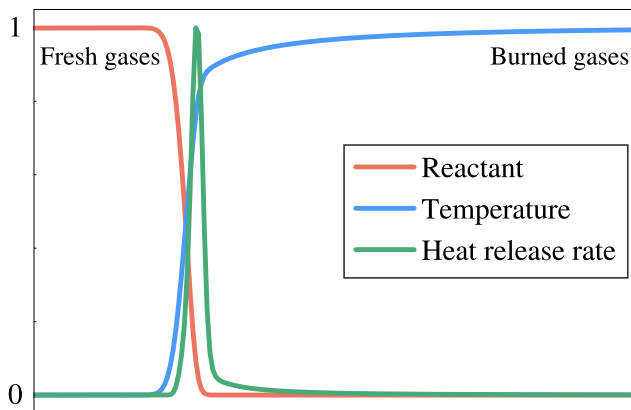


Figure 3.3: A one-dimensional laminar flame, where reactant mass fraction, temperature and heat release rate have been normalized.

The flame propagates toward the fresh gases, leaving burned gases behind. The reaction zone is where the reaction occurs and the chemical activity is situated around the peak heat release rate. In ideal one-dimensional flames with no heat losses, the temperature increases gradually from the unburned (subscript u), where the temperature starts to increase, causing a preheat zone before the reaction zone,

to the burned zone (subscript b), where the adiabatic temperature (T_{ad}) is reached. The adiabatic temperature corresponds to the maximum temperature reached in the burned gases when no heat losses are considered. The preheat and reaction zone form the flame front which propagates at a laminar flame speed s_L^0 defined by:

$$s_L^0 = -\frac{1}{\rho_u Y_{f,u}} \int \dot{\omega}_f dx, \quad (3.26)$$

where the reaction rate of the fuel is integrated over the x -axis. The thermal thickness δ_L^0 is defined as the steepest gradient of temperature:

$$\delta_L^0 = \frac{T_{ad} - T_u}{\max(dT/dx)}. \quad (3.27)$$

Another definition of flame thickness is the diffusion thickness:

$$\delta_D = \frac{\lambda_u}{\rho_u C_p s_L^0}. \quad (3.28)$$

The two definitions of flame thicknesses are used in this study as theoretical relations use one or the other, and sometimes both, as seen in Chapter 2. The diffusive thickness can be easily computed before computing a flame as long as the fresh gas properties and the flame speed are known. However, it is too approximate, and usually too small for purposes of mesh determination, which is why the thermal flame thickness is needed. The thermal thickness requires a first flame computation using mesh refinement with one-dimensional stationary flames using Cantera in the case of this study.

3.3.2 Strained flames

As discussed in Chapter 2, the turbulent flame is affected by stretch effects comprising strain and curvature. Laminar stretched premixed flames can be investigated in counterflow configurations in different set-ups:

- A single flame, where gases at its equilibrium state is sent against a flow of fresh gases,
- A twin flame, where fresh gases are blown against fresh gases, leading to two flames forming,

- And spherical flames.

Contrary to unstretched flames, where the flame speed is straightforward to derive, the flame speed of stretched flame is less straightforward, both numerically and experimentally. The consumption speed of a stretched flame depends on its Markstein number of Markstein length [2, 99, 100, 101]:

$$\frac{s_c}{s_L^0} = 1 - M_a^c \frac{\kappa \delta_D}{s_L^0}, \quad (3.29)$$

where κ is the flame's stretch and the consumption Markstein number is:

$$M_a^c = \frac{L_b^c}{\delta_D} = \frac{\beta (Le_{\text{eff}} - 1)}{2(\sigma - 1)} \int_1^\sigma \frac{\bar{\lambda}(x)}{x} \ln \frac{\sigma - 1}{x - 1} dx, \quad (3.30)$$

where L_b^c is the Markstein length, β is the Zel'dovich number, σ is the expansion ratio, which is the ratio of burned to unburned gases' density. In this study, when strained flame computations were needed, the twin flame setup was selected and computed using Cantera. These were preferred to single flame simulations as in these simulations, the solution is controlled by the temperature of the product stream. In twin flames, the solutions depend on the initial thermodynamic conditions and the strain only.

3.4 Stretch effects in premixed flame modeling

The turbulent combustion regime investigated throughout this study is limited to the thin reaction zone as it is relevant for intrinsic instabilities of the flame interaction with the flow, without the challenge of the broken reaction zone, and relevant for modeling insights. An often used concept in modeling premixed turbulent flames is the flamelet concept, where the reaction takes place in a thin layer that is wrinkled by turbulence, but not disrupted by it [102]. In flamelet modeling, a major assumption is that, due to the large difference in time scales between turbulence and chemical time scales, which are much slower, the flow and chemistry can be solved independently. A common assumption is that the structure of a flamelet is the one of a laminar flame. The thin reaction zone is commonly accepted to preserve the flamelet structure [71, 103, 104, 105]. However recent work has highlighted that in some cases, in the thin reaction zone, the turbulent consumption speed increases to values not explained by the increase of the flame surface [106, 107]. A non-unity stretch factor I_0 should be accounted for to consider

the flame speed increase, especially when preferential diffusion of light diffusing species is happening [83, 86, 93, 94, 107, 108, 109, 110]:

$$\frac{s_T}{s_L^0} = I_0 \frac{A_T}{A_0}, \quad (3.31)$$

with s_T the turbulent consumption speed, s_L^0 , the unstretched laminar flame speed and A_0 a reference flame surface. A_T represents a generalized turbulent flame surface, linked to the flame surface density by integrating Σ over the entire flame structure [70, 111]:

$$A_T = \int_0^1 \Sigma(c^*) dc^* = \int_{\Omega} |\nabla c| dV, \quad (3.32)$$

where c is the progress variable, c^* is used to define an isosurface of the progress variable representative of the reaction zone and Ω is the whole domain volume.

3.5 Direct Numerical Simulation

When all scales of the flow are solved, the numerical solution of the Navier-Stokes equation is called Direct Numerical Simulation. Although large progress in computer development has allowed the computation of 3-D turbulent reactive DNS, they remain computationally expensive and cannot be used in geometries with large domain sizes. Turbulent flows with small turbulence levels were first solved with DNS in the 70s [112, 113] using an incompressible homogeneous isotropic turbulence. In the 80s, work on different levels of turbulence and configuration, such as turbulent mixing layer, were investigated [114, 115, 116]. DNS in the scope of combustion was introduced at the same time, with chemical reactions introduced for constant density [117] and then, in the 90s, variable density effects, and heat release effects were introduced [118, 119, 120] both for global chemical schemes and then detailed ones [121]. Development in programming and parallel systems now allows us to perform such simulations, and extensive work has been performed through the use of DNS as reviewed recently by Domingo et al. [122]. DNS supports the development of turbulent combustion models [123, 124, 125, 126], allows to investigate different combustion regimes, and new fuels such as ammonia and hydrogen [86, 94, 110, 127].

3.6 DNS resolution requirements

DNS grids must ensure that all scales of turbulence are solved: the domain must be large enough for the largest scale to be solved, the mesh should be fine enough for the finest turbulent scales to be solved, and it should also be fine enough for the flame's inner structure to be solved. For a volume or an area of L^3 or L^2 , where L is the typical domain size, we can compute the number of points N that the mesh comprises in each dimension, and $\Delta x = L/N$ is the typical cell size. The domain size L should be of the order of one integral scale l_t : $L \geq l_t$ to fulfill the requirement of solving the largest scales. The smallest scales of turbulence are estimated with $\eta_k \simeq l_t/(Re_t)^{(3/4)}$ and should be resolved, a requirement too stringent in terms of computational cost and memory, especially in 3-D applications. Therefore, to solve the dissipative range, the mesh size should be of the same order of magnitude as η_k [122, 128]. An argument can be made that the Kolmogorov scales should be solved with the criterium $\eta_k/\Delta x > 0.5$ [53], a stringent requirement to meet. This leads to the requirement for the number of grid points in a direction to be $N > l_t/\eta_k$. Furthermore, the inner flame structure also has to be resolved on the mesh, to meet this criterion, ten to twenty grid points in the flame thickness should be included: $Q = \delta_L^0/\Delta x$ [2]. The size of the computational domain is given by $L \simeq (N/Q)\delta_L^0$. The Damköler number compares the turbulent time scale $\tau_t = l_t/u'$ with the chemical time scale $\tau_c = \delta_D/s_L^0$. The criteria for the computational domain grid encompassing both the turbulent criteria and the chemical one is [2, 122]:

$$Re_t Da = \left(\frac{l_t}{\delta_D} \right)^{1/2}, \quad (3.33)$$

and if δ_D and δ_L^0 are of the same order:

$$Re_t Da < (N/Q)^2. \quad (3.34)$$

To keep the computational domain's size at a reasonable level, the Damköler, Karlovitz, and turbulent Reynolds numbers should, therefore not all be too large simultaneously [122].

3.7 DNS solver

The code used throughout this study to perform the simulations is called AVBP, a suite of CFD tools performing DNS and LES of compressible, reactive or non-reacting, turbulent, multi-species flows¹ [129]. It is a parallel Fortran code developed using unstructured grids (definitions of unstructured grids will be detailed in Section 3.8), capable of solving the laminar and turbulent compressible Navier-Stokes equations in two and three dimensions. Steady and unsteady flows can be simulated. The code is programmed using Fortran 77, Fortran 90 and C subroutines. It uses the Message Passing Interface (MPI) for communication between processes in parallel execution. Chemical reaction coefficients are obtained using Cantera [98], and chemical scheme reduction was performed using Arcane [130]. Initialization of the flame is typically done using Cantera's one-dimensional simulation. HIP is used to create the geometry and mesh generation. Details on the schemes used and transport coefficients will be provided in the following sections and will be detailed in Chapter 5. The work was performed on CPU partitions using resources provided by both CERFACS and NTNU. Work was performed using HPC resources of GENCI-TGCC on Belenos (Processor type: AMD Epyc 7742 (Rome)), on the BETZY supercomputer (Processor type: AMD® Epyc™ 7742 2.25GHz), and on Kraken at CERFACS (Processors types: Xeon Gold 6140 (Sky-lake) and Xeon Platinum 8368 (IceLake)). The total CPU hours used in this work is around 6 million CPUh not accounting for test cases.

3.8 Numerical method

The Navier-Stokes equation presented in Section 3.1 needs to be written in their compact differential formulations to be solved numerically [131]:

$$\frac{\partial \mathbf{u}}{\partial t} + \nabla \cdot \mathbf{F} = \mathbf{s}, \quad (3.35)$$

where $\mathbf{u} = (\rho, \rho \mathbf{v}, \rho E)^T$ is the vector of conserved variables, $\mathbf{F} = (\mathbf{f}, \mathbf{g}, \mathbf{h})^T$ is the corresponding flux tensor and \mathbf{s} is the source terms. The fluxes can be divided into an inviscid convective part and a viscous part: $\mathbf{F} = \mathbf{F}^c(\mathbf{u}) + \mathbf{F}^v(\mathbf{u}, \nabla \mathbf{u})$. In AVBP, the control volume associated with such discretization is a cell-vertex

¹<http://www.cerfacs.fr/avbp7x>

method, where the residuals are computed at the cells before being scattered to the vertices [129, 131]. The first step is the discretization of the computational domain into polygons or polyhedrons, depending on the dimensions of the domain. The mesh -or grid- is generated. We note that, when the term "unstructured" is used to say that AVBP uses unstructured grids, this denotes the data type employed to describe the node connectivity, and does not describe the information about the shape of the grid elements. In AVBP, when a grid is composed of regular, structured shapes (made of cubic or hexahedral elements, for example), the data type is still one of an unstructured mesh. Eq. (3.35) is solved at each node of the grid using the following steps:

1. For each cell, the flux divergence of Eq. (3.35) is computed: this is the cell residual. It needs to be computed using the Green-Gauss theorem and discretized using the trapezoidal rule to integrate the fluxes along the edges of the cell, considering that the fluxes vary linearly along the edges.
2. Once the cell residual is defined, the information has to be spread to the nodes. The nodal residual is the volume-weighted average of the residuals of the cells adjacent to the node. The operation where the adjacent cell contribution is assembled is called scatter. This step requires a distribution matrix for which conservation needs to be ensured and allows the definition of different schemes, which will be presented later.
3. Once the residual calculation and distribution have been done, the solution needs to be advanced in time. The time derivative of Eq. (3.35) is integrated over the control volume, which is associated with the node. The time marching method will be presented hereafter.

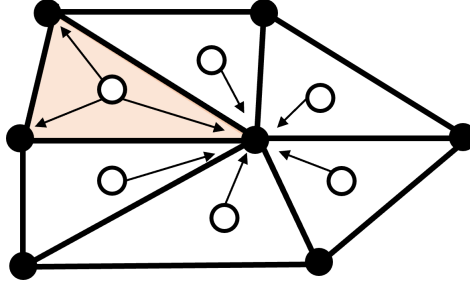


Figure 3.4: Cell vertex method: black dots are the node, the cell center is in white and the cell is colored in pink.

3.8.1 Time marching method

Time marching is done based on an N-step Runge-Kutta scheme the following way [131]:

$$\begin{aligned}
 \mathbf{u}^0 &= \mathbf{u}^n \\
 \mathbf{u}^1 &= \mathbf{u}^n + \alpha_1 \Delta t \Delta \mathbf{u}^1 \\
 &\vdots \\
 \mathbf{u}^{n+1} &= \mathbf{u}^n + \alpha_N \Delta t \Delta \mathbf{u}^N,
 \end{aligned} \tag{3.36}$$

where α_i are real coefficients and $\alpha_N = 1$. If $N = 1$, this corresponds to the classical explicit first-order Euler scheme.

$$\Delta \mathbf{u}^i = \frac{d\mathbf{u}^i}{dt}. \tag{3.37}$$

The time-step Δt is given either by the user or is variable depending on different parameters. Notably, the Courant-Friedrichs-Lewy or CFL number ensures the stability of the convective numerical scheme. The constraint is that the CFL number should be below a critical value of 1. The time-step constrained by the CFL number is:

$$\Delta t = CFL \frac{\Delta x}{u + c}, \tag{3.38}$$

where c is the speed of sound and u is the convection speed. In the case where we have a low Mach number and the acoustic waves are not relevant, the Pressure Gradient Scaling (PGS) can increase the time-step and gain computational time [132]. This is an artificial compressibility approach to artificially decrease the propagation speed of the acoustic waves (c) by rescaling pressure and temperature

by a factor α^2 : $T^* = \alpha^2 T$, $P^* = \alpha^2 P$. The resulting sound speed propagation is reduced artificially by α :

$$c^* = \sqrt{\gamma R T^*} = \sqrt{\gamma R \alpha^2 T} = \alpha c, \quad (3.39)$$

with γ the heat capacity ratio. The resulting artificial Mach number is $Ma^* = Ma/\alpha = U/c^* = U/c/\alpha$. The new CFL condition satisfies:

$$\Delta t^* = CFL \frac{\Delta x}{u + c^*}, \quad (3.40)$$

and the time-step Δt^* can be increased without changing the CFL condition as the speed sound is reduced by a factor α .

The Fourier term F limits the time-step to ensure the stability of the diffusive schemes. It is defined as:

$$F = \frac{D \Delta t}{\Delta x^2}, \quad (3.41)$$

where D is the diffusion coefficient.

Finally, the time-step is also derived from the chemical source term, which is why stiff species should be removed from the numerical scheme to limit the time-step:

$$\Delta t^{\text{source}} = \chi \min_j \left(\min_{\text{spec}} \Delta t_j^{\text{spec}} \right), \quad (3.42)$$

where χ is user-defined and depends on the chemistry used. Δt_j^{spec} is the node-valued time-step for each specie j :

$$\Delta t_j^{\text{spec}} = \frac{\rho_j}{\left| \mathbf{s}_j^{\text{spec}} \right|}. \quad (3.43)$$

The time-step is the minimum value between the three: CFL, Fourier, and chemical source term time-steps.

3.8.2 Cell-vertex convection schemes

This section describes some of the numerical schemes used in Chapter 5 for the convective part of Eq. (3.35), \mathbf{F}^c . The first scheme to be described is not used in this work but serves to understand the other schemes: it is the Central Differences scheme, where the cell residual is equally distributed to the different vertices, it

is not dissipative and leads to an unconditionally unstable scheme. Then there is the Lax-Wendroff scheme [133], which is a central finite volume-centered scheme with full discretization involving space and time, First, the time discretization is done using a third-order Taylor series:

$$\frac{\mathbf{u}^{n+1} - \mathbf{u}^n}{\Delta t} = \left. \frac{\partial \mathbf{u}}{\partial t} \right|^n + \frac{1}{2} \left. \frac{\partial^2 \mathbf{u}}{\partial t^2} \right|^n \Delta t + \mathcal{O}(\Delta t^2). \quad (3.44)$$

Eq. (3.35) is then used to replace the time derivatives by space derivatives, which leads to the numerical scheme LW being a second order both in time and space scheme.

The other class of convection schemes is the Taylor-Galerkin scheme, where, such as LW schemes, the Taylor series is used to express the solution at the time t^{n+1} , then times derivative are replaced by space ones, and finally, Eq. 3.44 is discretized in space, using Galerkin finite element method. This last step enables a more precise computation of the mass matrix, instead of using an approximation for it, such as in LW. However, the mass matrix should be inverted using the Jacobi method, which leads to a more expensive computation but also to a gain in accuracy. The two-step Taylor-Galerkin C (TTGC) comes from this finite element method [134, 135] and leads to a third-order accurate solution for convective terms in regular meshes. TTGC presents good dispersive and dissipative properties and will limit numerical scheme perturbation (wiggles). Furthermore, artificial viscosity is used for these spatially centered schemes as they tend to create wiggles. Artificial viscosity can be used to limit those wiggles, although they may affect the accuracy of the solution [131].

3.8.3 Cell-vertex diffusion schemes

The diffusion terms \mathbf{F}^v are discretized based on a Galerkin finite element method, a vertex-centered scheme. The implementation is not strictly the Galerkin finite element method due to the complexity and computational expense the exact formulation would require [131]. To determine the viscous flux divergence $\nabla \cdot \mathbf{F}_j^v$ only the nodes belonging to the cell adjacent to the node j are used. This enables to compute the viscous flux divergence on the control volume associated with node j . The operator enables to dissipate small scales and is more physical compared to other schemes such as the cell-vertex operator [131].

3.9 Boundary conditions

The boundary conditions in a numerical simulation are needed to impose conditions to solve the equations. Inside the computational domain, the variables are updated using the information from surrounding cells. However, at the boundaries, a node is missing for the numerical scheme, and physical information is also missing. Therefore, defining boundary conditions is a key part of numerical simulations. The unsteadiness of compressible flow due to acoustic waves appearing, or velocity and entropy perturbations, as well as numerical perturbations, should be evacuated from the domain. Boundary conditions, therefore, serve a crucial role in controlling wave reflections in the domain and evacuating unsteady activities. If target values are strictly imposed (such as velocity or pressure) towards which the code should be converging, this will lead to fully reflecting boundaries, and the acoustic energy will remain in the domain. Characteristic boundary conditions, or non-reflecting boundary conditions, are preferred and used throughout Chapter 5 to evacuate the unsteady perturbations from the domain. Navier-Stokes Characteristic Boundary Conditions are used [136], where waves leaving the domain are well computed by the numerical scheme, while waves entering the domain are not computed by the numerical scheme and are user-defined values. This requires a correction term to the incoming wave. However, a drawback of the non-reflecting boundary condition is the target quantity is not secured. Relaxed characteristic boundary conditions allow having a non-reflecting boundary while also converging to the target quantity.

Chapter 4

DNS specificities

The notions presented in the previous Chapters and how they relate to the simulations performed throughout this work are detailed here. First, the grid specificities of the simulations of Chapter 5 are presented, followed by a description of the chemical mechanism used, and the numerical methods specific to the simulations. Finally, the boundary conditions used are described.

4.1 Grid specificities in the simulations

In the work performed in this thesis, two types of simulations are performed. First, Direct Numerical Simulations of laminar flames in a 2-D domain (Paper 2), and second, turbulent 3-D simulations are performed (Papers 1 and 3). Direct Numerical Simulation in the context of 2-D laminar flames, as is presented in Paper 2, does not concern itself with the resolution of the turbulent scales, as no turbulence is involved. However, for a precise resolution of the flame front development, a large number of points in the flame front are needed, and no modeling of the subgrid-scale is implemented, leading to the use of the DNS terminology in this context. In the turbulent 3-D flames in Papers 1 and 3, the flame front is resolved with at least 12 points. The domain size is sufficiently large to solve the integral scale based on the turbulence spectrum that is selected. The resulting Kolmogorov scales are of the order of 10^{-5} , as is the mesh size. Although some literature references consider that to solve the dissipative range, the mesh size should be of the same order of magnitude as η_k [122, 128], an argument can be made that the Kolmogorov scales should be solved with the criterium $\eta_k/\Delta x > 0.5$ [53], which

is nearly verified in the 3-D simulations performed (where $\eta_k/\Delta x > 0.4$). However, we find that this level of mesh refinement provides sufficient information into the preferential diffusion effect we want to investigate, as the inner structure of the flame front is sufficiently resolved, and the resolution is fine enough to capture most of the dissipation: no artificial viscosity is added in the simulations. This refinement level enables us to investigate the flame interaction with turbulence with a sufficient resolution and, therefore to perform the analysis that we want in regards to thermo-diffusive instabilities in the thin reaction zone.

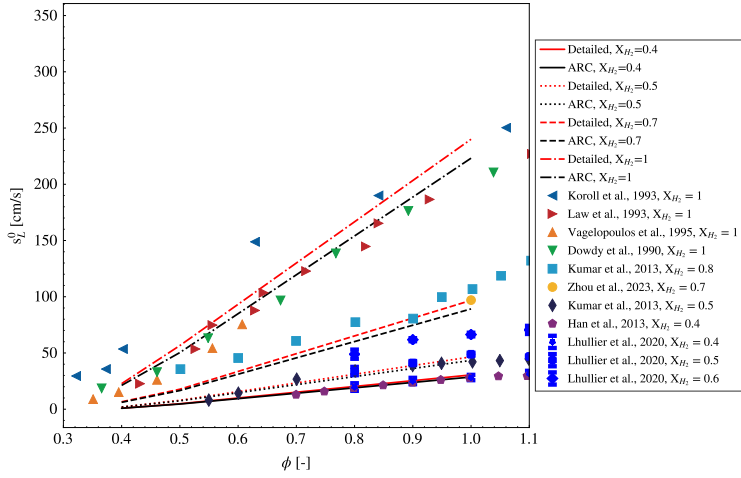
4.2 Chemical mechanism scheme reduction and validation

The number of equations to be solved during the computation depends directly on the number of species. Therefore, the chemical mechanism selection is important. In the case of ammonia/hydrogen flames, the complexity of the chemistry and the need to investigate the flame structure undergoing preferential diffusion effects led to the selection of detailed chemical schemes. In this work, two kinetic schemes are used to perform the DNS, one with NO_x for the work considering 2-D simulations (Paper 2), and the second where NO_x production is not considered, to reduce the scheme -and by extension, reduce the computational cost- in the 3-D cases (Papers 1 and 3). They are both derived from CRECK [3] and reduced with the CERFACS in-house reduction tool, Arcane [130]. The first scheme has 18 species, 6 species with QSS assumption and 150 reactions, while the second scheme has 14 species, 7 species with QSS assumption and 88 reactions. Both schemes were reduced using Arcane [130], a reduction tool using an automated procedure to reduce schemes using target values. The procedure is based on three steps briefly described hereafter. The first step is the Direct Relation Graph with Error Propagation, where species and reactions not relevant to the target configuration of the selected canonical case are eliminated from the chemical model. Chemical lumping is the second step, where groups of isomers are represented by single representative species, which reduces the number of species and reactions without changing the reaction dynamics. Finally, Quasi-Steady State assumptions are performed where species with short characteristic time scales are removed, leading to fewer transport equations and removing numerical stiffness. Error thresholds

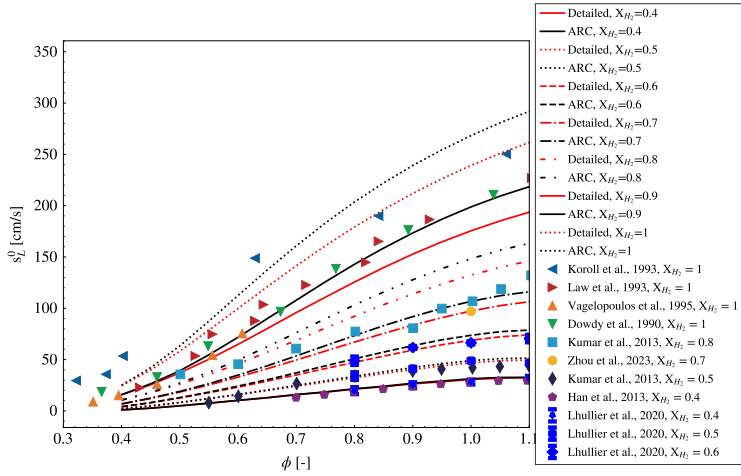
based on canonical cases (one-dimensional unstretched flames, counterflow flame, 0-D reactors) are given for the following quantities: the adiabatic temperature, laminar flame speed, and for some species mass fraction (NO for the 18-species mechanism), and the reduction is automated. We find a good agreement between experimental data, the detailed CRECK scheme, and the reduced schemes within the investigated range of each study using one-dimensional Cantera simulations, as is presented in Chapter 5 (Papers 2 and 3), and illustrated in Fig. 4.1 for the laminar flame speed. A large amount of discrepancy from experimental data in the literature regarding the laminar flame speed of ammonia/hydrogen fuel blend, and even pure hydrogen, is revealed in these comparisons. Validation between the detailed CRECK mechanism and the reduced mechanisms for the adiabatic temperature is also presented, with very good agreement between the two schemes (Fig. 4.2).

Increasing the amount of hydrogen lessens the accuracy of the reduced scheme compared to the complete one. Nevertheless, a reasonable agreement is found for the large scope of data for the two reduced schemes, and we use them assuming their accuracy is sufficient for the purpose of investigating thermo-diffusive instabilities in laminar and turbulent premixed flames. In the context of DNS, the number of species in the two schemes is quite large, and therefore we use the term "detailed chemistry" in the context of DNS computations, although we recognize the existence of detailed schemes with several hundreds of species and thousands of reactions.

In this work, scalar transport properties are approximated with a constant Lewis number for each species without thermal diffusion. Indeed, we find from the literature and Cantera simulations that, compared to a multi-component formulation, results from mixture-averaged formulation gave comparable results with mixture-averaged formulations [137] but led to a significant gain of computational resources. Furthermore, regarding the impact of Soret and Dufour effects (which is where species diffusing at different rates will exhibit different diffusion due to temperature gradient) in the context of mixture-averaged simulations, their inclusion impacts the flame structure but is not the leading order phenomenon that controls it [138], which is the Fourier's and Fick's laws. In this thesis, they are therefore not included, but it is recommended to include them in future numerical investigations,



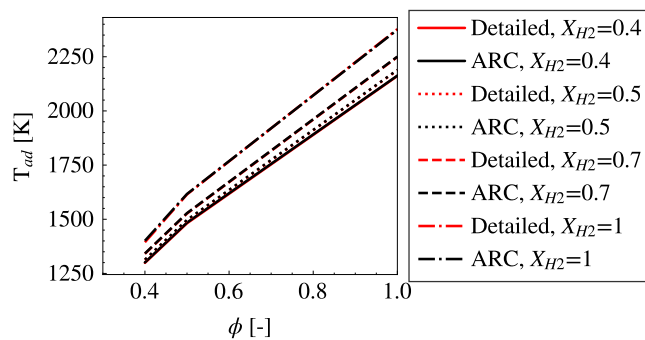
(a) 18 species



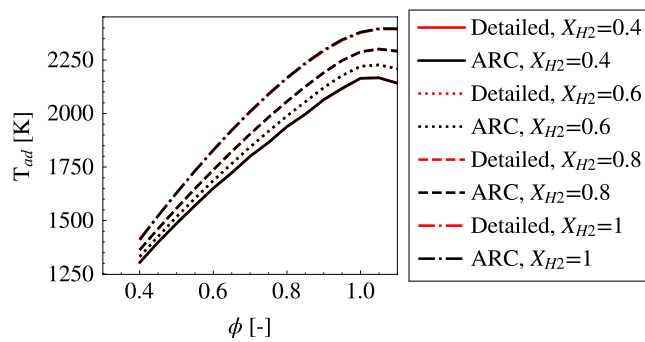
(b) 14 species

Figure 4.1: Scheme validation for the NH_3/H_2 blends for the laminar flame speed. Numerical data from CRECK [3] (detailed), and reduced ARC mechanism against experiment from Koroll et al. [4], Law et al. [5], Vagelopoulos et al. [6], Dowdy et al. [7], Kumar et al. [8], Zhou et al. [9], Han et al. [10], and Lhuillier et al. [11].

as we assume they might enhance the thermo-diffusive instabilities [110, 139], and their inclusion would lead to more accurate physics in the simulations.



(a) 18 species



(b) 14 species

Figure 4.2: Scheme validation for the NH_3/H_2 blends for the adiabatic temperature. Numerical data from CRECK [3] (detailed) against reduced ARC mechanism.

4.3 Numerical methods

Regarding the CFL described in Chapter 2, we find a reasonable limit for the artificial Mach number M^* is 0.3 to remain incompressible, 0.25 is selected in Chapter 5 for Papers 1 and 3. This leads to a speed-up of the time step for the time-step $\Delta t^*/\Delta t = 1/\sqrt{\alpha}$, leading to a faster simulation with no loss of information. Regarding the convection scheme selected in this thesis, although higher-order schemes are preferred to perform DNS, we find LW for the 2-D cases (Paper 2) and TTGC for the 3-D cases (Papers 1 and 3) to be sufficiently accurate in the performed study. Indeed, in the case of the DNS performed in Chapter 5, the mesh resolution and numerical schemes selected led to no artificial viscosity being added to the simulation, indicating a good compromise between guarantying low spatial dissipation and low dispersions effects, and performing the simulation at a reasonable computational cost.

4.4 Boundary conditions

Typically, in Chapter 5, the following boundary conditions are used. At the inlet, reflecting velocity, temperature, and species are imposed. In turbulent cases (Papers 1 and 3), a turbulent perturbation is also imposed at the inlet and enters the domain. In order to maintain the mean inlet variables around their target values, relaxation coefficients are used to specify the ingoing waves to relax every variable toward its target. This enables to keep the mean variables around their target values and, at the same time, let the high-frequency waves leave the domain. Regarding turbulence injection, there exist various ways for turbulence to be injected inside a domain [140]. Strong recycling methods use an auxiliary simulation to prescribe the velocity field at the inlet of the new simulation, while weak recycling methods use internal mapping to prescribe the velocity at an upstream cut of the domain back to the inlet. There are several solutions to use synthetic turbulent injection. One of which is the synthetic random Fourier method, where random Fourier modes are summed to generate velocity fluctuation. The velocity fluctuation has an amplitude that follows a turbulent energy spectrum that is modeled. The spectrum either follows the Von-Karman-Pao spectrum to simulate the complete energy spectra, which leads to a peak of large structures as well as a greater variety of structure scales. Or, as is done in Papers 1 and 3, the Passot-Pouquet

spectrum is followed, which has a peak at a lower wave number leading to smaller scales homogeneous structures, in order to obtain homogeneous isotropic turbulence. Although recirculation methods typically lead to more realistic turbulent scales, the Passot-Pouquet spectrum skips the inertial range and represents the flow scales having dissipative character without an a priori simulation, that would further increase the computational cost. Other methods include the synthetic digital filtering method, synthetic coherent eddy method, and volume forcing methods. At the outlet, a reflecting pressure is imposed: a relaxation that is equal to zero will lead to a perfectly non-reflecting boundary condition, while large values lead to nearly reflecting conditions. Finally, when it is needed, periodicity where the quantities are the same at two opposite faces is used in a weak formulation.

Chapter 5

Summary of papers

The results of this doctoral work are presented and discussed in three papers that are published in, or submitted to peer-reviewed international journals. In this chapter, a summary of the respective papers is presented, together with comments on how the papers are connected. The contribution of the author to each paper is designated by elements introduced by "the author".

The author's contributions on joint papers

The contributions of the author to the papers are listed as follows:

- Paper 1: Victor Coulon, Jessica Gaucherand, Victor Xing, Davide Laera, Corentin Lapeyre, Thierry Poinsot (2023). *Direct Numerical Simulation of methane, ammonia-hydrogen and hydrogen turbulent premixed flames*, Combustion and Flame, Vol. 256, Page 112933.

In this paper, the author's contribution consisted of performing the DNS for the ammonia/hydrogen flame, as well as contributing to the post-processing of the data with a focus on the ammonia/hydrogen flame. The study was designed and guided by Davide Laera, Corentin Lapeyre, and Thierry Poinsot. The other simulations were performed by Victor Xing (who computed the methane flame) and Victor Coulon (for the hydrogen flame). The post-processing and paper redaction was done by Victor Coulon, and reviewed by all the co-authors.

- Paper 2: Jessica Gaucherand, Davide Laera, Corinna Schulze-Netzer, Thierry Poinso (2023). *Intrinsic instabilities of hydrogen and hydrogen/ammonia premixed flames: influence of equivalence ratio, fuel composition and pressure.*, Combustion and Flame, Vol. 256, Page 112986.

The author modified the AVBP code to implement a new way to initialize the computational domain with a Cantera flame with a sinusoidal perturbation of the flame front. The author performed a parametric sweep of DNSs, performed all the post-processing of the DNS and of one-dimensional flames to support the analysis, and wrote the paper. The study was designed and guided by Thierry Poinso, Corinna Schulze-Netzer and Davide Laera. All the co-authors contributed to analyzing the results and reviewing the paper.

- Paper 3: Jessica Gaucherand, Davide Laera, Corinna Schulze-Netzer, Thierry Poinso (2023). *DNS of turbulent premixed ammonia/hydrogen flames: the effects of thermo-diffusive instabilities.*, Submitted to Flow, Turbulence and Combustion, in review.

The author performed a parametric sweep of DNSs, performed all the post-processing of the DNS and of one-dimensional flames to support the analysis, and wrote the paper. Corinna Schulze-Netzer contributed to the post-processing of some of the data provided by the author. The study was designed and guided by Thierry Poinso, Corinna Schulze-Netzer and Davide Laera. All the co-authors contributed to analyzing the results and reviewing the paper.

5.1 Paper I: Direct Numerical Simulation of methane, ammonia-hydrogen and hydrogen turbulent premixed flames

In this paper, three premixed flames with the same laminar flame speed and similar thickness are investigated through Direct Numerical Simulations. The first one is a methane flame at stoichiometry, the second a pure hydrogen flame at an equivalence ratio of 0.45, and lastly, a stoichiometric ammonia/hydrogen flame with a nearly equimolar blend of hydrogen and ammonia in the fuel. These three flames are subjected to the same turbulence intensity, but end up behaving in largely different ways. While the methane and ammonia/hydrogen flame have a similar flame

surface and length, the lean hydrogen flame is much shorter, and the flame thickness decreases while burning rates increase. This is illustrated by Fig. 5.1 where the isosurface of progress variables at the maximum value of the heat release rate in the equivalent unstretched flame ($c(\max(\dot{\omega}_T)) = c^*$) are used to describe the flame front, and are colored by the normalized heat release rate, normalized with the maximum heat release rate from the unstretched one-dimensional flame.

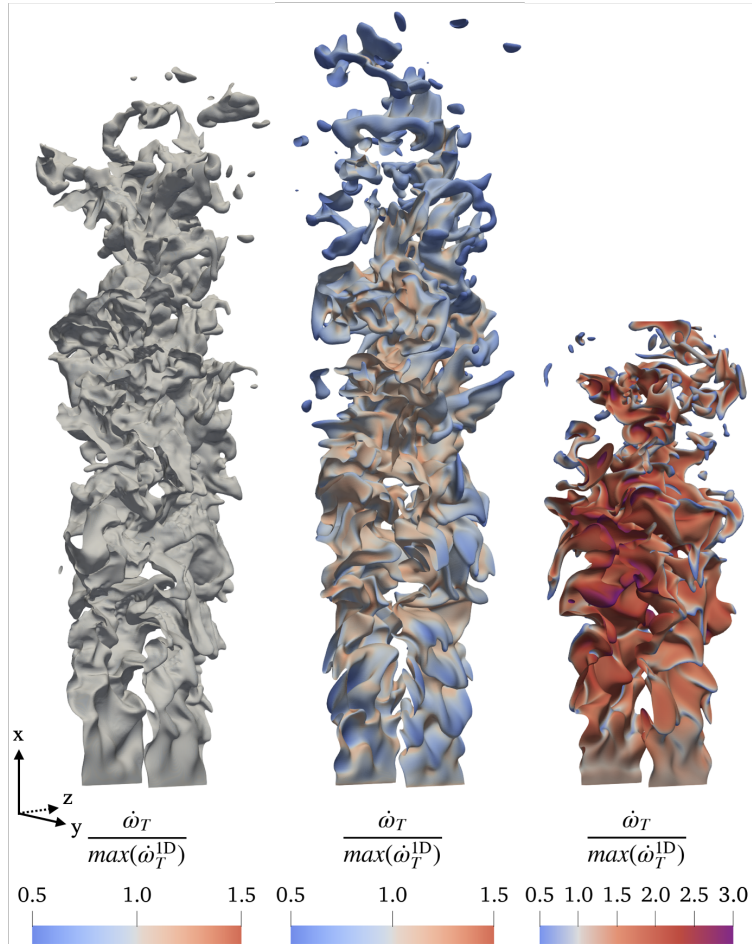


Figure 5.1: Isosurfaces of $c = c^*$, extracted after two flow-through times $t = 2\tau$ and colored by heat release rate normalized by the maximum value in the corresponding 1-D unstretched laminar flame for all cases. Methane case at $c_{CH_4}^* = 0.72$ (left), ammonia/hydrogen case at $c_{H_2O}^* = 0.8$ (center), hydrogen case at $c_{H_2}^* = 0.85$ (right).

Preferential diffusion of hydrogen in the pure hydrogen flame leads to convexly curved elements where the reaction rate is much larger due to enrichment in those regions. In regions that are not strongly curved, the impact of the strain on the hydrogen flame strongly impacts the reaction rate: indeed, in one-dimensional stretched flames simulations, it is seen that the lean hydrogen flame speed increases with strain -while for the other flames the flame speed decreases with strain- and this leads to an increase of the flame speed in the lean turbulent hydrogen flame. This observation leads to the suggestion of a comparison of the 3-D data of the hydrogen flame with 1-D stretched flames simulation and it is found that the flame speed increase in the 3-D turbulent flame is well captured by the 1-D simulations at varying strain rates and equivalence ratio. The increase of flame surface due to wrinkling for the ammonia/hydrogen and methane flames is induced by the turbulence alone, leading to a stretch factor close to unity. Whereas for the hydrogen case, the stretch factor is equal to two. Furthermore, as the conditional mean of the heat release rates conditioned on the progress variable of the 3-D flames is compared to the heat release of the laminar flame counterpart as a function of the progress variable, the hydrogen flame exhibits a large deviation from the unstretched case, leading to the non-validity of flamelet assumption in this case. The ammonia/hydrogen flame exhibits a large scatter but the conditional mean value remains close to the unstretched laminar flame, which we attribute to the fact that this flame is at stoichiometric conditions. For the methane flame, good agreement of the conditional mean with the unstretched flamelet is found, as well as a very small scatter. This leads to the conclusion that the stoichiometric ammonia/hydrogen flame blend could potentially replace, without retrofitting a combustor, a methane flame. This conclusion does not account for phenomena like flashbacks in gas turbines, which would need a separate investigation out of the scope of this thesis. Furthermore, the flamelet assumption, in the ammonia/hydrogen stoichiometric case, could be used for modeling, a conclusion that is not extended to the pure hydrogen case for which modeling implications are different and need to consider the effect of preferential diffusion into modeling aspects. This paper serves as an answer to the following research question investigated in the introduction of this thesis: how does an ammonia/hydrogen turbulent flame compare to methane and a pure hydrogen flame? We find that, although a scatter of heat release rate around the mean is found for the stoichiometric ammonia/hydrogen flame, its conditional mean is

close to an unstretched one, like it is for methane, leading to flamelet assumption validity. However, the preferential diffusion of hydrogen leads to local enrichment in some convex places and depletion in concave ones, similar to the pure hydrogen flame case. However, the overall structure is not widely affected by these preferential diffusion effects, likely due to the stoichiometric condition selected. Further ammonia/hydrogen blends need to be investigated, especially in leaner conditions.

5.2 Paper II: Intrinsic instabilities of hydrogen and hydrogen/ammonia premixed flames: influence of equivalence ratio, fuel composition and pressure.

In this paper, a parametric investigation of premixed ammonia/hydrogen blends at different blends and equivalence ratios is performed from pure hydrogen (H_2) to a blend of 40% of H_2 and 60% of ammonia (NH_3) in volume, equivalence ratios (0.4 to 1.0) and pressures (1 and 10 bar) to investigate thermo-diffusive instabilities. Indeed, as the first paper and other literature work have shown [83, 84], pure lean hydrogen flames exhibit thermo-diffusive instabilities, but in the case of ammonia/hydrogen blends, the development of these instabilities is still unclear. Work by Wiseman et al. [94] and Netzer et al. [93] has highlighted that in lean cases, characteristic thermo-diffusive behavior had been identified in preheat conditions. At atmospheric conditions, work by Mukundakumar et al. [127] identified thermo-diffusive instabilities in lean cases but only going down to an equivalence ratio of 0.6. Therefore we know that in some conditions, thermo-diffusive instabilities appear for ammonia/hydrogen flames, in which hydrogen diffuses in convex zones and burns quicker and faster and at a higher intensity. However, it is still unclear if lean ammonia/hydrogen flames behave like pure hydrogen or if the impact of ammonia additions dampens the instabilities. To investigate this question, a linear stability analysis is performed where the dispersion relation of a mixture -an indicator of a flame's tendency to become more or less unstable as it responds to a perturbation- is computed using Direct Numerical Simulations. The results obtained show that ammonia addition and equivalence ratio increase dampen the instabilities, a result that was known for pure hydrogen flame and is now extended to ammonia/hydrogen blends. Hydrodynamic -or Darrieus Landau (DL) instabilities were found to dominate mixtures at stoichiometry, and the computed relation

dispersion was equal or below the DL dispersion relation for all wave numbers: the thermo-diffusive mechanisms had a stabilizing impact on the mixtures' instabilities. On the other hand, for leaner mixtures, the computed dispersion relation is above the DL dispersion relation at small wave numbers: the thermo-diffusive mechanism further destabilizes the flame front. This is illustrated in Fig. 5.2 where the DNS-derived dispersion relation is illustrated for the 1 bar cases.

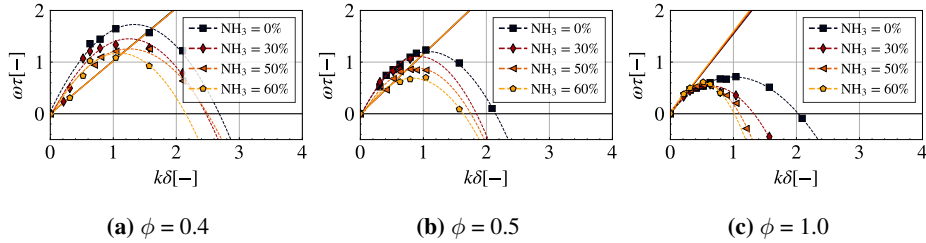


Figure 5.2: Dispersion relation for varying equivalence ratio, at various NH_3 contents in volume in the fuel. Symbols correspond to the growth rates extracted from the simulations, dashed lines correspond to the second-order polynomial fit of these growth rates. The theoretical hydrodynamic growth rate $\omega_{DL}\tau$ is also shown in solid line for all blends.

An important aspect is also to understand if theoretical relation dispersions are able to capture the behavior of ammonia/hydrogen blends in order to limit the computation of expensive DNS: this first requires computing the Lewis number of the blend. This is done in a section of the paper through the use of 1-D strained flame computations, and we find that the volume-based definition of the Lewis number of a mixture is most suited for the ammonia/hydrogen blend, therefore answering one of the research questions asked in the introduction. Comparisons with theoretical dispersion relations showed the theory's difficulty in fitting the stabilizing effects at large wave numbers for lean mixtures. This indicates a need for new theoretical relations to capture lean flame behavior. This was known for pure hydrogen but is now extended to blends of ammonia and hydrogen. At high pressure, thinner flames and higher growth rates as chain termination reactions became more important for both NH_3/H_2 blends and pure H_2 led to more unstable flames. This study led to a quantitative assessment of thermo-diffusive instabilities in ammonia/hydrogen blends, finding that these blends are stabilized by ammonia increase, but that lean cases are unstable due to hydrogen's fast diffusion.

We confirmed that preferential diffusion was to be expected in lean ammonia/hydrogen blends, and we then want to investigate how lean ammonia/hydrogen blends might behave if they were in a turbulent flow. Indeed, the first study informed that pure hydrogen would lead to a faster flame consumption and high heat release compared to its unstretched counterpart. We wonder if ammonia/hydrogen blends will also behave the same. If this were the case, then to get the same value of heat release rate, one may benefit from the stretch factor effect instead of increasing the equivalence ratio.

5.3 Paper III: DNS of turbulent premixed ammonia/hydrogen flames: the effects of thermo-diffusive instabilities.

In this paper, four Direct Numerical Simulations of turbulent premixed ammonia hydrogen flames are computed. The fuel composition with the ratio of ammonia and hydrogen varies between 19% and 57% of NH_3 , and the equivalence ratio varies between 0.44 and 0.95. The two leanest flames have similar flame speeds (0.17 m/s), while the two others have flame speeds close to 0.30 m/s. The four compositions tested are chosen to represent a large spectrum of operating conditions. The composition and characteristics of the flame enable us to study the effects of thermo-diffusive instabilities in a turbulent flow and to look into the chemistry and stretch effects at play in the development of the flames. As this is done in the context of supporting model development, a first suggestion consists of finding a progress variable to parametrize the combustion process. To do so, the irreducible error for different progress variable definitions is computed regarding the equivalence ratio and the heat release rate. The H_2O -based progress variable is found to be a suitable definition to reduce the error with the conditional means and the scatter of values of these parameters. Similarly to the first paper, the stretch factor for the four flames is computed, and it is found that a value of stretch factor of 2.69 is found for the leanest case with 18% of NH_3 in volume in the fuel and 0.44 equivalence ratio. This is higher than the value of the stretch factor obtained for the pure H_2 case of the first study at $\phi = 0.45$. This is notably attributed to the strain, and the steep gradient of the radical pool and laminar flame speed for the broad distribution of equivalence ratio obtained in 3-D. Large flamelet deviation is found for the leaner cases, as seen in Fig. 5.3. Thermo-diffusive due to the blend's com-

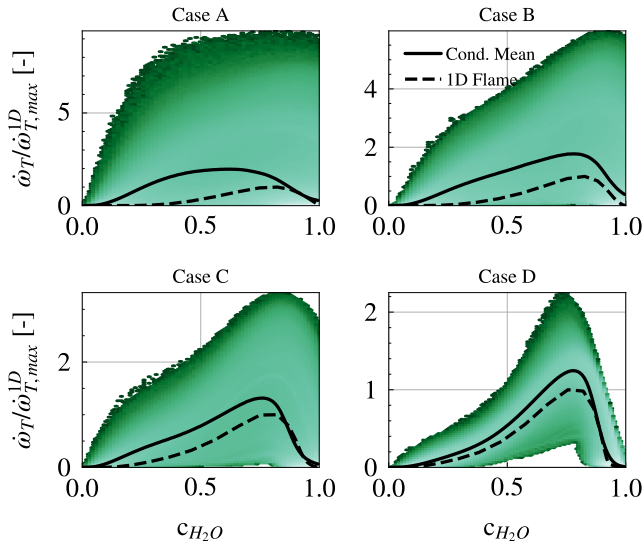


Figure 5.3: Normalized heat release rate after two flow-through times with the corresponding joint probability density function of the quantity conditioned by the progress variable c_{H_2O} for the four cases. A lighter shade in the colormap represents a greater probability of the PDF. The dashed line corresponds to the 1-D unstretched laminar flames and the solid line corresponds to the conditional mean of the quantity versus progress variable.

position interaction with turbulence leads to the curvature and strain, which further enhance the instabilities and modify the flame structure beyond the expectation of $s_T/s_L^0 = A_T/A_0$. Instead, a super unity stretch factor must be accounted for to account for the larger-than-expected flame speed and more wrinkling, leading to more flame surface and reduced flame brush length. Similarly to the pure H₂ case from Paper 1, we find that the 3-D stretch factor can be well described by performing stretched one-dimensional flame and computing the flame speed increase. For the nearly stoichiometric case, the predictive assessment method doesn't properly compute the near unity stretch factor. Indeed, in this case, the stretched flame speed decreases with strain, and the method is no longer valid. Therefore, this predictive method enables us to determine where flame instabilities might be expected to lead to a super unity stretch factor and also provides an expectation of the stretch value that might be accounted for in a model.

Chapter 6

Conclusions and outlook

Three papers investigating ammonia/hydrogen-premixed flames were investigated. The impact of preferential diffusion of hydrogen leading to thermo-diffusive instabilities was well known to impact the flame front and enhance the reactivity strongly, but these observations are now extended to lean ammonia/hydrogen blends. From intrinsic instabilities in laminar flame through linear phase dispersion relation up to the interaction with turbulence, it was found that ammonia/hydrogen premixed flame would become shortened with more wrinkle and a strongly enhanced flame speed compared to its laminar unstretched counterpart, were they lean mixtures. Predictive tools using strained one-dimensional flames for modeling purposes based on the database of DNS performed were suggested, although they require a priori knowledge of the strain values. This thesis, therefore, leads to new findings in the domain of ammonia/hydrogen combustion through Direct Numerical Simulations. Some of the main findings are recapped here:

- Regarding the flame structure and thermo-diffusive instabilities of ammonia/hydrogen premixed flames:
 - Ammonia addition dampens intrinsic thermo-diffusive instabilities, increased equivalence ratio too.
 - Lean ammonia/hydrogen mixtures in turbulent flow will exhibit high reactivity and strong wrinkling due to stretch effects.

- And regarding the validity of theoretical relations and modeling implications:
 - Theoretical relations dispersions do not capture the dispersion relation from DNS of lean ammonia/hydrogen blends.
 - A volume-based Lewis number definition is well suited for an ammonia/hydrogen blend.
 - A progress variable based on water is well suited to describe the combustion state of lean ammonia/hydrogen flames.
 - The Markstein number can support the knowledge of where ammonia/hydrogen blends will be unstable.
 - Strained one-dimensional flame can inform the global stretch factor of lean turbulent ammonia/hydrogen flames.

The work performed here could benefit from the following research as complementary:

- Inclusion of multi-components transport formulations, and including Soret and Dufour effects could benefit the level of details of the investigation of NH_3/H_2 flames and their impact on thermo-diffusive instabilities.
- Investigating higher order schemes for convective and diffusive terms.
- The work performed in this study has not investigated the impact of NO_x in thermo-diffusively unstable flames. It had been investigated by Netzer et al. [93] in laminar perturbed flames and Rieth et al. [95] in preheated conditions, but looking into the formation of NO_x atmospheric conditions would also be interesting to formulate strategies on their mitigation. It is expected that NO formation will strongly depend on equivalence ratio variation due to preferential diffusion.
- The parametric study performed in Paper 2 could benefit from further operating points investigated. Indeed, intermediate ammonia content or equivalence ratio might lead to more instabilities as ammonia dissociates into hydrogen.

- The implementation into combustion models for RANS or LES of the strained-based correction from Paper 1 or the one based on the ammonia content and equivalence ratio from Paper 3 would enable to validate the model suggested and had not been done in this work, but would be a useful addition to model hydrogen-based fuels.

Bibliography

- [1] D. R. MacFarlane, P. V. Cherepanov, J. Choi, B. H. Suryanto, R. Y. Hodgetts, J. M. Bakker, F. M. Ferrero Vallana, and A. N. Simonov, “A roadmap to the ammonia economy,” *Joule*, vol. 4, pp. 1186–1205, 2020, doi:10.1016/j.joule.2020.04.004.
- [2] T. Poinso and D. Veynante, *Theoretical and Numerical Combustion*. Edwards, 2005.
- [3] A. Stagni, C. Cavallotti, S. Arunthanayothin, Y. Song, O. Herbinet, F. Battin-Leclerc, and T. Faravelli, “An experimental, theoretical and kinetic-modeling study of the gas-phase oxidation of ammonia,” *Reaction Chemistry & Engineering*, vol. 5, pp. 696–711, 2020, doi:10.1039/C9RE00429G.
- [4] G. Koroll, R. Kumar, and E. Bowles, “Burning velocities of hydrogen-air mixtures,” *Combustion and Flame*, vol. 94, pp. 330–340, 1993, doi:10.1016/0010-2180(93)90078-H.
- [5] C. K. Law, *Reduced Kinetic Mechanisms for Applications in Combustion Systems*. Springer Berlin Heidelberg, 1993.
- [6] C. Vagelopoulos, F. Egolfopoulos, and C. Law, “Further considerations on the determination of laminar flame speeds with the counterflow twin-flame technique,” *Proceedings of the Combustion Institute*, vol. 25, pp. 1341–1347, 1994, doi:10.1016/S0082-0784(06)80776-9.

- [7] D. R. Dowdy, D. B. Smith, S. C. Taylor, and A. Williams, “The use of expanding spherical flames to determine burning velocities and stretch effects in hydrogen/air mixtures,” *Proceedings of the Combustion Institute*, vol. 23, pp. 325–332, 1991, doi:10.1016/S0082-0784(06)80275-4.
- [8] P. Kumar and T. R. Meyer, “Experimental and modeling study of chemical-kinetics mechanisms for H₂–NH₃–air mixtures in laminar premixed jet flames,” *Fuel*, vol. 108, pp. 166–176, 2013, doi:10.1016/j.fuel.2012.06.103.
- [9] S. Zhou, B. Cui, W. Yang, H. Tan, J. Wang, H. Dai, L. Li, Z. ur Rahman, X. Wang, S. Deng, and X. Wang, “An experimental and kinetic modeling study on NH₃/air, NH₃/H₂/air, NH₃/CO/air, and NH₃/CH₄/air premixed laminar flames at elevated temperature,” *Combustion and Flame*, vol. 248, p. 112536, 2023, doi:10.1016/j.combustflame.2022.112536.
- [10] X. Han, Z. Wang, M. Costa, Z. Sun, Y. He, and K. Cen, “Experimental and kinetic modeling study of laminar burning velocities of NH₃/air, NH₃/H₂/air, NH₃/CO/air and NH₃/CH₄/air premixed flames,” *Combustion and Flame*, vol. 206, pp. 214–226, 2019, doi:10.1016/j.combustflame.2019.05.003.
- [11] C. Lhuillier, P. Brequigny, F. Contino, and C. Mounaïm-Rousselle, “Combustion Characteristics of Ammonia in a Modern Spark-Ignition Engine,” in *Conference on Sustainable Mobility*, Oct. 2019.
- [12] H. Kobayashi, A. Hayakawa, K. D. A. Somarathne, and E. C. Okafor, “Science and technology of ammonia combustion,” *Proceedings of the Combustion Institute*, vol. 37, no. 1, pp. 109–133, 2019, doi:10.1016/j.proci.2018.09.029.
- [13] E. A. Wrigley, “Energy and the English Industrial Revolution,” *Philosophical Transactions of the Royal Society A: Mathematical, Physical and Engineering Sciences*, vol. 371, 2013, doi:10.1098/RSTA.2011.0568.
- [14] H. Ritchie, M. Roser, and P. Rosado, “Energy,” 2022.

- [15] O. Edenhofer, R. Pichs-Madruga, Y. Sokona, S. Kadner, J. C. Minx, and S. Brunner, “AR5 Climate Change 2014: Mitigation of Climate Change — IPCC,” 2014.
- [16] A. Valera-Medina, F. Amer-Hatem, A. K. Azad, I. C. Dedoussi, M. De Joannon, R. X. Fernandes, P. Glarborg, H. Hashemi, X. He, S. Mashruk, J. McGowan, C. Mounaim-Rouselle, A. Ortiz-Prado, A. Ortiz-Valera, I. Rossetti, B. Shu, M. Yehia, H. Xiao, and M. Costa, “Review on ammonia as a potential fuel: From synthesis to economics,” *Energy and Fuels*, vol. 35, pp. 6964–7029, 2021, doi:10.1021/acs.energyfuels.0c03685.
- [17] W. S. Chai, Y. Bao, P. Jin, G. Tang, and L. Zhou, “A review on ammonia, ammonia-hydrogen and ammonia-methane fuels,” *Renewable and Sustainable Energy Reviews*, vol. 147, p. 111254, Sep. 2021, doi:10.1016/j.rser.2021.111254.
- [18] X. Xu, E. Liu, N. Zhu, F. Liu, and F. Qian, “Review of the current status of ammonia-blended hydrogen fuel engine development,” *Energies*, vol. 15, no. 3, p. 1023, Jan. 2022, doi:10.3390/en15031023.
- [19] S. Ghavam, M. Vahdati, I. A. Wilson, and P. Styring, “Sustainable Ammonia Production Processes,” *Frontiers in Energy Research*, vol. 9, 2021, doi:10.3389/fenrg.2021.580808.
- [20] L. Rosa and M. Mazzotti, “Potential for hydrogen production from sustainable biomass with carbon capture and storage,” *Renewable and Sustainable Energy Reviews*, vol. 157, p. 112123, Apr. 2022, doi:10.1016/j.rser.2022.112123.
- [21] N. Sánchez-Bastardo, R. Schlögl, and H. Ruland, “Methane pyrolysis for zero-emission hydrogen production: A potential bridge technology from fossil fuels to a renewable and sustainable hydrogen economy,” *Industrial & Engineering Chemistry Research*, vol. 60, no. 32, pp. 11 855–11 881, Aug. 2021, doi:10.1021/acs.iecr.1c01679.
- [22] Y. Woo, J. J. Young, Y. J. Lee, and J.-N. Kim, “Recent progress on the Ammonia-Gasoline and the Ammonia-Diesel Dual Fueled Internal Combustion Engines in Korea,” in *NH₃ Fuel Conference*, 2014.

- [23] J. Mathis. NH₃ car. [Online]. Available: <http://nh3car.com/news.html>
- [24] J. T. Gray, E. Dimitroff, N. T. Meckel, and R. D. Quillian, “Ammonia fuel — engine compatibility and combustion,” *SAE Transactions*, vol. 75, pp. 785–807, 1967, doi:<https://www.jstor.org/stable/44563675>.
- [25] A. J. Reiter and S.-C. Kong, “Combustion and emissions characteristics of compression-ignition engine using dual ammonia-diesel fuel,” *Fuel*, vol. 90, pp. 87–97, 2011, doi:10.1016/j.fuel.2010.07.055.
- [26] P. Dimitriou and R. Javid, “A review of ammonia as a compression ignition engine fuel,” *International Journal of Hydrogen Energy*, vol. 45, pp. 7098–7118, 2020, doi:10.1016/j.ijhydene.2019.12.209.
- [27] C. Mounaïm-Rousselle and P. Brequigny, “Ammonia as Fuel for Low-Carbon Spark-Ignition Engines of Tomorrow’s Passenger Cars,” *Frontiers in Mechanical Engineering*, vol. 6, no. September, pp. 1–5, 2020, doi:10.3389/fmech.2020.00070.
- [28] D. Pashchenko, R. Mustafin, and I. Karpilov, “Ammonia-fired chemically recuperated gas turbine: Thermodynamic analysis of cycle and recuperation system,” *Energy*, vol. 252, p. 124081, 2022, doi:10.1016/j.energy.2022.124081.
- [29] X. Wei, M. Zhang, J. Wang, and Z. Huang, “Investigation on lean blow-off characteristics and stabilization mechanism of pre-mixed hydrogen enhanced ammonia/air swirl flames in a gas turbine combustor,” *Combustion and Flame*, vol. 249, p. 112600, 2023, doi:10.1016/j.combustflame.2022.112600.
- [30] N. A. Hussein, A. Valera-Medina, and A. S. Alsaegh, “Ammonia- hydrogen combustion in a swirl burner with reduction of nox emissions,” *Energy Procedia*, vol. 158, pp. 2305–2310, 2019, innovative Solutions for Energy Transitions, doi:10.1016/j.egypro.2019.01.265, Innovative Solutions for Energy Transitions.
- [31] A. Hayakawa, T. Goto, R. Mimoto, Y. Arakawa, T. Kudo, and H. Kobayashi, “Laminar burning velocity and Markstein length of ammonia/air pre-

- mixed flames at various pressures,” *Fuel*, vol. 159, pp. 98–106, 2015, doi:10.1016/j.fuel.2015.06.070.
- [32] H. Xiao, A. Valera-Medina, and P. J. Bowen, “Modeling Combustion of Ammonia/Hydrogen Fuel Blends under Gas Turbine Conditions,” *Energy and Fuels*, vol. 31, no. 8, pp. 8631–8642, 2017, doi:10.1021/acs.energyfuels.7b00709.
- [33] S. Frigo and R. Gentili, “Analysis of the behaviour of a 4-stroke Si engine fuelled with ammonia and hydrogen,” *International Journal of Hydrogen Energy*, vol. 38, no. 3, pp. 1607–1615, 2013, doi:10.1016/j.ijhydene.2012.10.114.
- [34] G. Ciccarelli, D. Jackson, and J. Verreault, “Flammability limits of NH₃-H₂-N₂-air mixtures at elevated initial temperatures,” *Combustion and Flame*, vol. 144, no. 1-2, pp. 53–63, 2006, doi:10.1016/j.combustflame.2005.06.010.
- [35] C. S. Mørch, A. Bjerre, M. P. Gøttrup, S. C. Sorenson, and J. Schramm, “Ammonia/hydrogen mixtures in an SI-engine: Engine performance and analysis of a proposed fuel system,” *Fuel*, vol. 90, no. 2, pp. 854–864, 2011, doi:10.1016/j.fuel.2010.09.042.
- [36] F. R. Westlye, A. Ivarsson, and J. Schramm, “Experimental investigation of nitrogen based emissions from an ammonia fueled SI-engine,” *Fuel*, vol. 111, no. 2, pp. 239–247, 2013, doi:10.1016/j.fuel.2013.03.055.
- [37] K. Ryu, G. E. Zacharakis-Jutz, and S. C. Kong, “Performance enhancement of ammonia-fueled engine by using dissociation catalyst for hydrogen generation,” *International Journal of Hydrogen Energy*, vol. 39, pp. 2390–2398, 2014, doi:10.1016/j.ijhydene.2013.11.098.
- [38] G. Xin, C. Ji, S. Wang, C. Hong, H. Meng, and J. Yang, “Experimental study on the effect of hydrogen substitution rate on combustion and emission characteristics of ammonia internal combustion engine under different excess air ratio,” *Fuel*, vol. 343, 2023, doi:10.1016/j.fuel.2023.127992.

- [39] J. S. Cardoso, V. Silva, R. C. Rocha, M. J. Hall, M. Costa, and D. Eusébio, “Ammonia as an energy vector: Current and future prospects for low-carbon fuel applications in internal combustion engines,” *Journal of Cleaner Production*, vol. 296, p. 126562, 2021, doi:10.1016/j.jclepro.2021.126562.
- [40] B. Wang, H. Wang, B. Duan, C. Yang, D. Hu, and Y. Wang, “Effect of ammonia/hydrogen mixture ratio on engine combustion and emission performance at different inlet temperatures,” *Energy*, vol. 272, p. 127110, 2023, doi:10.1016/j.energy.2023.127110.
- [41] A. Valera-Medina, M. Gutesa, H. Xiao, D. Pugh, A. Giles, B. Goktepe, R. Marsh, and P. Bowen, “Premixed ammonia/hydrogen swirl combustion under rich fuel conditions for gas turbines operation,” *International Journal of Hydrogen Energy*, vol. 44, no. 16, pp. 8615–8626, 2019, doi:10.1016/j.ijhydene.2019.02.041.
- [42] O. Fawwaz Aalrebei, A. Hamdan Al Assaf, A. Amhamed, N. Swaminathan, and S. Hewlett, “Ammonia-hydrogen-air gas turbine cycle and control analyses,” *International Journal of Hydrogen Energy*, vol. 47, no. 13, pp. 8603–8620, 2022, doi:10.1016/j.ijhydene.2021.12.190.
- [43] K. Bioche, L. Bricteux, A. Bertolino, A. Parente, and J. Blondeau, “Large eddy simulation of rich ammonia/hydrogen/air combustion in a gas turbine burner,” *International Journal of Hydrogen Energy*, vol. 46, no. 79, pp. 39 548–39 562, 2021, doi:10.1016/j.ijhydene.2021.09.164.
- [44] F. Oppong, Z. Luo, X. Li, Y. Song, and C. Xu, “Intrinsic instability of different fuels spherically expanding flames: A review,” *Fuel Processing Technology*, vol. 234, p. 107325, Sep. 2022, doi:10.1016/j.fuproc.2022.107325.
- [45] Y. Cai, T. Li, M. Du, and J. Li, “Effects of thermodiffusive instability on the spherical premixed flames anchored to a porous-plug burner,” *Aerospace Science and Technology*, vol. 97, p. 105632, 2020, doi:10.1016/j.ast.2019.105632.
- [46] S. Kadowaki, H. Suzuki, and H. Kobayashi, “The unstable behavior of cellular premixed flames induced by intrinsic instability,” *Pro-*

- ceedings of the Combustion Institute*, vol. 30, pp. 169–176, 2005, doi:10.1016/j.proci.2004.07.041.
- [47] S. Kadowaki, H. Takahashi, and H. Kobayashi, “The effects of radiation on the dynamic behavior of cellular premixed flames generated by intrinsic instability,” *Proceedings of the Combustion Institute*, vol. 33, no. 1, pp. 1153–1162, 2011, doi:10.1016/j.proci.2010.06.069.
- [48] Y. Li, M. Bi, and W. Gao, “Theoretical pressure prediction of confined hydrogen explosion considering flame instabilities,” *Journal of Loss Prevention in the Process Industries*, vol. 57, pp. 320–326, Jan. 2019, doi:10.1016/j.jlp.2019.01.001.
- [49] O. Dounia, “Numerical investigation of gas explosion phenomena in confined and obstructed channels.” Ph.D. dissertation, Université Fédérale de Toulouse, INPT - Ecole doctorale MEGeP. 4, 2018.
- [50] S. Zitouni, P. Brequigny, and C. Mounaim-Rousselle, “Influence of hydrogen and methane addition in laminar ammonia premixed flame on burning velocity, Lewis number and Markstein length,” *Combustion and Flame*, vol. 253, p. 112786, 2023, doi:10.1016/j.combustflame.2023.112786.
- [51] V. Xing, “Deep learning for subgrid-scale modeling in large eddy simulations of turbulent premixed combustion,” PhD Thesis, Ecole doctorale MEGEP - CERFACS, 11 2022.
- [52] C. J. Lapeyre, A. Misdariis, N. Cazard, D. Veynante, and T. Poinso, “Training convolutional neural networks to estimate turbulent sub-grid scale reaction rates,” *Combustion and Flame*, vol. 203, pp. 255–264, May 2019, doi:10.1016/j.combustflame.2019.02.019.
- [53] S. B. Pope, *Turbulent Flows*. Cambridge University Press, Aug. 2000.
- [54] A. N. Kolmogorov, “The local structure of turbulence in incompressible viscous fluid for very large reynolds numbers,” *Proceedings: Mathematical and Physical Sciences*, vol. 434, no. 1890, pp. 9–13, 1991, doi:10.1098/rspa.1991.0075.

- [55] J. Hinze, *Turbulence*. McGraw-Hill, 1987.
- [56] A. N. Kolmogorov, “Dissipation of energy in the locally isotropic turbulence,” *Proceedings: Mathematical and Physical Sciences*, vol. 434, no. 1890, pp. 15–17, 1941, doi:10.1098/rspa.1991.0076.
- [57] N. Peters, *Turbulent Combustion*. Cambridge University Press, 2000.
- [58] I. Glassman, *Combustion*. Academic Press, 1996.
- [59] E. C. Okafor, H. Yamashita, A. Hayakawa, K. D. A. Somarathne, T. Kudo, T. Tsujimura, M. Uchida, S. Ito, and H. Kobayashi, “Flame stability and emissions characteristics of liquid ammonia spray co-fired with methane in a single stage swirl combustor,” *Fuel*, vol. 287, 2021, doi:10.1016/j.fuel.2020.119433.
- [60] C. Kurien, P. S. Varma, and M. Mittal, “Effect of ammonia energy fractions on combustion stability and engine characteristics of gaseous (ammonia/methane) fuelled spark ignition engine,” *International Journal of Hydrogen Energy*, vol. 48, no. 4, pp. 1391–1400, 2023, doi:10.1016/j.ijhydene.2022.10.032.
- [61] D. Lapalme, R. Lemaire, and P. Seers, “Assessment of the method for calculating the Lewis number of H₂/CO/CH₄ mixtures and comparison with experimental results,” *International Journal of Hydrogen Energy*, vol. 42, pp. 8314–8328, 2017, doi:10.1016/j.ijhydene.2017.01.099.
- [62] N. Bouvet, F. Halter, C. Chauveau, and Y. Yoon, “On the effective Lewis number formulations for lean hydrogen/hydrocarbon/air mixtures,” *International Journal of Hydrogen Energy*, vol. 38, pp. 5949–5960, 2013, doi:10.1016/j.ijhydene.2013.02.098.
- [63] S. Muppala, M. Nakahara, N. Aluri, H. Kido, J. Wen, and M. Papalexandris, “Experimental and analytical investigation of the turbulent burning velocity of two-component fuel mixtures of hydrogen, methane and propane,” *International Journal of Hydrogen Energy*, vol. 34, pp. 9258–9265, 2009, doi:10.1016/j.ijhydene.2009.09.036.

- [64] F. Dinkelacker, B. Manickam, and S. Muppala, “Modelling and simulation of lean premixed turbulent methane/hydrogen/air flames with an effective Lewis number approach,” *Combustion and Flame*, vol. 158, pp. 1742–1749, 2011, doi:10.1016/j.combustflame.2010.12.003.
- [65] C. Law, G. Jomaas, and J. Bechtold, “Cellular instabilities of expanding hydrogen/propane spherical flames at elevated pressures: theory and experiment,” *Proceedings of the Combustion Institute*, vol. 30, pp. 159–167, 2005, doi:10.1016/j.proci.2004.08.266.
- [66] C. Tang, Z. Huang, C. Jin, J. He, J. Wang, X. Wang, and H. Miao, “Laminar burning velocities and combustion characteristics of propane–hydrogen–air premixed flames,” *International Journal of Hydrogen Energy*, vol. 33, no. 18, pp. 4906–4914, 2008, doi:https://doi.org/10.1016/j.ijhydene.2008.06.063.
- [67] G. Joulin and T. Mitani, “Linear stability analysis of two-reactant flames,” *Combustion and Flame*, vol. 40, pp. 235–246, 1981, doi:10.1016/0010-2180(81)90127-9.
- [68] S. B. Pope, “The evolution of surfaces in turbulence,” *Int. J. Eng. Sci.*, vol. 26, pp. 445–469, 1988, doi:10.1016/0020-7225(88)90004-3.
- [69] R. Borghi, “On the structure and morphology of turbulent premixed flames,” *Recent Advances in the Aerospace Sciences*, pp. 117–138, 1985, doi:10.1007/978-1-4684-4298-4_7.
- [70] D. Veynante and L. Vervisch, “Turbulent combustion modeling,” *Progress in Energy and Combustion Science*, vol. 28, pp. 193–266, 2002, doi:10.1016/S0360-1285(01)00017-X.
- [71] A. W. Skiba, T. M. Wabel, C. D. Carter, S. D. Hammack, J. E. Temme, and J. F. Driscoll, “Premixed flames subjected to extreme levels of turbulence part I: Flame structure and a new measured regime diagram,” *Combustion and Flame*, vol. 189, pp. 407–432, 2018, doi:10.1016/j.combustflame.2017.08.016.

- [72] G. Darrieus, “Propagation d’un front de flamme,” *La Technique Moderne*, vol. 30, p. 18, 1938.
- [73] M. Matalon and B. J. Matkowsky, “Flames as gasdynamic discontinuities,” *Journal of Fluid Mechanics*, vol. 124, p. 239–259, 1982, doi:10.1017/S0022112082002481.
- [74] M. Matalon, C. Cui, and J. K. Bechtold, “Hydrodynamic theory of premixed flames: effects of stoichiometry, variable transport coefficients and arbitrary reaction orders,” *Journal of Fluid Mechanics*, vol. 487, p. 179–210, 2003, doi:10.1017/S0022112003004683.
- [75] C. Sun, C. Sung, L. He, and C. Law, “Dynamics of weakly stretched flames: quantitative description and extraction of global flame parameters,” *Combustion and Flame*, vol. 118, pp. 108–128, 1999, doi:10.1016/S0010-2180(98)00137-0.
- [76] G. I. Sivashinsky, “Instabilities, pattern formation, and turbulence in flames,” *Annual Review of Fluid Mechanics*, vol. 15, pp. 179–199, 1983, doi:10.1146/annurev.fl.15.010183.001143.
- [77] ———, “Diffusional-thermal theory of cellular flames,” *Combustion Science and Technology*, vol. 15, no. 3-4, pp. 137–145, Jan. 1977, doi:10.1080/00102207708946779.
- [78] S. Yang, A. Saha, F. Wu, and C. K. Law, “Morphology and self-acceleration of expanding laminar flames with flame-front cellular instabilities,” *Combustion and Flame*, vol. 171, pp. 112–118, Sep. 2016, doi:10.1016/j.combustflame.2016.05.017.
- [79] Z.-Y. Sun and G.-X. Li, “Propagation characteristics of laminar spherical flames within homogeneous hydrogen-air mixtures,” *Energy*, vol. 116, pp. 116–127, Dec. 2016, doi:10.1016/j.energy.2016.09.103.
- [80] F.-S. Li, G.-X. Li, Y.-H. Jiang, H.-M. Li, and Z.-Y. Sun, “Study on the effect of flame instability on the flame structural characteristics of hydrogen/air mixtures based on the fast fourier transform,” *Energies*, vol. 10, no. 5, p. 678, 2017, doi:10.3390/en10050678.

- [81] C. Altantzis, C. Frouzakis, A. Tomboulides, and K. Boulouchos, “Numerical simulation of propagating circular and cylindrical lean premixed hydrogen/air flames,” *Proceedings of the Combustion Institute*, vol. 34, no. 1, pp. 1109–1115, 2013, doi:10.1016/j.proci.2012.07.072.
- [82] L. Berger, A. Attili, and H. Pitsch, “Intrinsic instabilities in premixed hydrogen flames: Parametric variation of pressure, equivalence ratio, and temperature. part 1 - dispersion relations in the linear regime,” *Combustion and Flame*, vol. 240, p. 111935, 2022, doi:10.1016/j.combustflame.2021.111935.
- [83] —, “Synergistic interactions of thermodiffusive instabilities and turbulence in lean hydrogen flames,” *Combustion and Flame*, vol. 244, p. 112254, 2022, doi:10.1016/j.combustflame.2022.112254.
- [84] T. Howarth and A. Aspden, “An empirical characteristic scaling model for freely-propagating lean premixed hydrogen flames,” *Combustion and Flame*, vol. 237, p. 111805, 2022, doi:10.1016/j.combustflame.2021.111805.
- [85] T. Howarth, E. Hunt, and A. Aspden, “Thermodiffusively-unstable lean premixed hydrogen flames: Phenomenology, empirical modelling, and thermal leading points,” *Combustion and Flame*, vol. 253, p. 112811, Jul. 2023, doi:10.1016/j.combustflame.2023.112811.
- [86] M. Rieth, A. Gruber, F. A. Williams, and J. H. Chen, “Enhanced burning rates in hydrogen-enriched turbulent premixed flames by diffusion of molecular and atomic hydrogen,” *Combustion and Flame*, vol. 239, p. 111740, 2022, doi:10.1016/j.combustflame.2021.111740.
- [87] T. M. Vu, J. Park, O. B. Kwon, and J. S. Kim, “Effects of hydrocarbon addition on cellular instabilities in expanding syngas–air spherical premixed flames,” *International Journal of Hydrogen Energy*, vol. 34, no. 16, pp. 6961–6969, Aug. 2009, doi:10.1016/j.ijhydene.2009.06.067.
- [88] M. Reyes, R. Sastre, F. Tinaut, and J. Rodríguez-Fernández, “Study and characterization of the instabilities generated in expanding spherical flames of hydrogen/methane/air mixtures,” *International Journal*

- of Hydrogen Energy*, vol. 47, no. 53, pp. 22 616–22 632, Jun. 2022, doi:10.1016/j.ijhydene.2022.05.063.
- [89] E. C. Okafor, Y. Nagano, and T. Kitagawa, “Experimental and theoretical analysis of cellular instability in lean H₂-CH₄-air flames at elevated pressures,” *International Journal of Hydrogen Energy*, vol. 41, no. 15, pp. 6581–6592, Apr. 2016, doi:10.1016/j.ijhydene.2016.02.151.
- [90] E. C. Okafor, A. Hayakawa, Y. Nagano, and T. Kitagawa, “Effects of hydrogen concentration on premixed laminar flames of hydrogen–methane–air,” *International Journal of Hydrogen Energy*, vol. 39, no. 5, pp. 2409–2417, Feb. 2014, doi:10.1016/j.ijhydene.2013.11.128.
- [91] E. C. Okafor, Y. Naito, S. Colson, A. Ichikawa, T. Kudo, A. Hayakawa, and H. Kobayashi, “Experimental and numerical study of the laminar burning velocity of CH₄–NH₃–air premixed flames,” *Combustion and Flame*, vol. 187, pp. 185–198, 2018, doi:10.1016/j.combustflame.2017.09.002.
- [92] A. Ichikawa, A. Hayakawa, Y. Kitagawa, K. K. A. Somarathne, T. Kudo, and H. Kobayashi, “Laminar burning velocity and Markstein length of ammonia/hydrogen/air premixed flames at elevated pressures,” *International Journal of Hydrogen Energy*, vol. 40, no. 30, pp. 9570–9578, Aug. 2015, doi:10.1016/j.ijhydene.2015.04.024.
- [93] C. Netzer, A. Ahmed, A. Gruber, and T. Løvås, “Curvature effects on no formation in wrinkled laminar ammonia/hydrogen/nitrogen-air premixed flames,” *Combustion and Flame*, vol. 232, p. 111520, 2021, doi:10.1016/j.combustflame.2021.111520.
- [94] S. Wiseman, M. Rieth, A. Gruber, J. R. Dawson, and J. H. Chen, “A comparison of the blow-out behavior of turbulent premixed ammonia/hydrogen/nitrogen-air and methane–air flames,” *Proceedings of the Combustion Institute*, vol. 38, pp. 2869–2876, 2021, doi:10.1016/j.proci.2020.07.011.
- [95] M. Rieth, A. Gruber, and J. H. Chen, “A direct numerical simulation study on no and n₂o formation in turbulent premixed ammonia/hydrogen/nitrogen-air flames,” *Proceedings of*

- the Combustion Institute*, vol. 39, no. 2, pp. 2279–2288, 2023, doi:10.1016/j.proci.2022.07.266.
- [96] J. O. Hirschfelder, C. F. Curtiss, and R. B. B. Wiley, “Molecular theory of gases and liquids.” *Journal of Polymer Science*, vol. 17, no. 83, pp. 116–116, 1955, doi:10.1017/S0368393100117833.
- [97] L. Onsager, “The distribution of energy in turbulence.” *Physical Review*, vol. 68, p. 286, 1945.
- [98] D. G. Goodwin, H. K. Moffat, I. Schoegl, R. L. Speth, and B. W. Weber, “Cantera: An object-oriented software toolkit for chemical kinetics, thermodynamics, and transport processes,” 2022, version 2.6.0.
- [99] P. Pelce and P. Clavin, “Influence of hydrodynamics and diffusion upon the stability limits of laminar premixed flames,” *Journal of Fluid Mechanics*, vol. 124, p. 219–237, 1982, doi:10.1017/S002211208200247X.
- [100] J. Buckmaster and D. Mikolaitis, “The premixed flame in a counterflow,” *Combustion and Flame*, vol. 47, pp. 191–204, 1982, doi:10.1016/0010-2180(82)90100-6.
- [101] J. Bechtold and M. Matalon, “The dependence of the Markstein length on stoichiometry,” *Combustion and Flame*, vol. 127, no. 1, pp. 1906–1913, 2001, doi:10.1016/S0010-2180(01)00297-8.
- [102] N. Peters, “Laminar flamelet concepts in turbulent combustion,” *Symposium (International) on Combustion*, vol. 21, no. 1, pp. 1231–1250, Jan. 1988, doi:10.1016/S0082-0784(88)80355-2.
- [103] A. J. Aspden, M. S. Day, and J. B. Bell, “Turbulence–flame interactions in lean premixed hydrogen: transition to the distributed burning regime,” *Journal of Fluid Mechanics*, vol. 680, pp. 287–320, May 2011, doi:10.1017/jfm.2011.164.
- [104] A. Aspden, M. Day, and J. Bell, “Three-dimensional Direct Numerical Simulation of turbulent lean premixed methane combustion with detailed kinetics,” *Combustion and Flame*, vol. 166, pp. 266–283, Apr. 2016, doi:10.1016/j.combustflame.2016.01.027.

- [105] G. Nivarti and S. Cant, “Direct Numerical Simulation of the bending effect in turbulent premixed flames,” *Proceedings of the Combustion Institute*, vol. 36, no. 2, pp. 1903–1910, 2017, doi:10.1016/j.proci.2016.07.076.
- [106] S. Mohammadnejad, Q. An, P. Vena, S. Yun, and S. Kheirikhah, “Thick reaction zones in non-flamelet turbulent premixed combustion,” *Combustion and Flame*, vol. 222, pp. 285–304, Dec. 2020, doi:10.1016/j.combustflame.2020.08.047.
- [107] A. Attili, S. Luca, D. Denker, F. Bisetti, and H. Pitsch, “Turbulent flame speed and reaction layer thickening in premixed jet flames at constant Karlovitz and increasing Reynolds numbers,” *Proceedings of the Combustion Institute*, vol. 38, no. 2, pp. 2939–2947, 2021, doi:10.1016/j.proci.2020.06.210.
- [108] M. Rieth, A. Gruber, and J. H. Chen, “The effect of pressure on lean premixed hydrogen-air flames,” *Combustion and Flame*, vol. 250, p. 112514, 2023, doi:10.1016/j.combustflame.2022.112514.
- [109] A. Aspden, “A numerical study of diffusive effects in turbulent lean premixed hydrogen flames,” *Proceedings of the Combustion Institute*, vol. 36, no. 2, pp. 1997–2004, 2017, doi:10.1016/j.proci.2016.07.053.
- [110] L. Berger, K. Kleinheinz, A. Attili, and H. Pitsch, “Characteristic patterns of thermodynamically unstable premixed lean hydrogen flames,” *Proceedings of the Combustion Institute*, vol. 37, pp. 1879–1886, 2019, doi:10.1016/j.proci.2018.06.072.
- [111] L. Vervisch, E. Bidaux, K. N. Bray, and W. Kollmann, “Surface density function in premixed turbulent combustion modeling, similarities between probability density function and flame surface approaches,” *Physics of Fluids*, vol. 7, pp. 2496–2503, 1995, doi:10.1063/1.868693.
- [112] S. A. Orszag, “Analytical theories of turbulence,” *Journal of Fluid Mechanics*, vol. 41, p. 363–386, 1970, doi:10.1017/S0022112070000642.

- [113] S. A. Orszag and G. S. Patterson, “Numerical simulation of three-dimensional homogeneous isotropic turbulence,” *Physical Review Letters*, vol. 28, no. 2, pp. 76–79, Jan. 1972, doi:10.1103/PhysRevLett.28.76.
- [114] J. R. Herring and R. M. Kerr, “Comparison of Direct Numerical Simulations with predictions of two-point closures for isotropic turbulence convecting a passive scalar,” *Journal of Fluid Mechanics*, vol. 118, no. -1, p. 205, May 1982, doi:10.1017/S0022112082001049.
- [115] R. S. Rogallo and P. Moin, “Numerical simulation of turbulent flows,” *Annual Review of Fluid Mechanics*, vol. 16, pp. 99–137, 1984, doi:10.1146/annurev.fl.16.010184.000531.
- [116] V. Eswaran and S. B. Pope, “Direct Numerical Simulations of the turbulent mixing of a passive scalar,” *Physics of Fluids*, vol. 31, no. 3, p. 506, 1988, doi:10.1063/1.866832.
- [117] A. D. Leonard and J. C. Hill, “Direct Numerical Simulation of turbulent flows with chemical reaction,” *Journal of Scientific Computing*, vol. 3, no. 1, pp. 25–43, Mar. 1988, doi:10.1007/BF01066481.
- [118] T. Poinso, D. Veynante, and S. Candel, “Quenching processes and premixed turbulent combustion diagrams,” *Journal of Fluid Mechanics Digital Archive*, vol. 228, p. 561, Jul. 1991, doi:10.1017/S0022112091002823.
- [119] P. Domingo and L. Vervisch, “Triple flames and partially premixed combustion in autoignition of non-premixed turbulent mixtures,” *Symposium (International) on Combustion*, vol. 26, no. 1, pp. 233–240, Jan. 1996, doi:10.1016/S0082-0784(96)80221-9.
- [120] L. Vervisch and T. Poinso, “Direct Numerical Simulation of non-premixed turbulent flames,” *Annual Review of Fluid Mechanics*, vol. 30, no. 1, pp. 655–691, Jan. 1998, doi:10.1146/annurev.fluid.30.1.655.
- [121] M. Baum, T. J. Poinso, D. C. Haworth, and N. Darabiha, “Direct Numerical Simulation of H₂/O₂/N₂ flames with complex chemistry in two-dimensional turbulent flows,” *Journal of Fluid Mechanics*, vol. 281, pp. 1–32, Dec. 1994, doi:10.1017/S0022112094003010.

- [122] P. Domingo and L. Vervisch, “Recent developments in DNS of turbulent combustion,” *Proceedings of the Combustion Institute*, 2022, doi:10.1016/j.proci.2022.06.030.
- [123] A. Aniello, D. Laera, L. Berger, A. Attili, and T. Poinso, “Introducing thermodynamic effects in large-eddy simulation of turbulent combustion for lean hydrogen-air flames,” *Proceedings of the 2022 Summer Program*, 2022, doi:10.1017/S0022112070000642.
- [124] J. Sellmann, J. Lai, A. M. Kempf, and N. Chakraborty, “Flame surface density based modelling of head-on quenching of turbulent premixed flames,” *Proceedings of the Combustion Institute*, vol. 36, no. 2, pp. 1817–1825, 2017, doi:10.1016/j.proci.2016.07.114.
- [125] W. Han, A. Scholtissek, F. Dietzsch, and C. Hasse, “Thermal and chemical effects of differential diffusion in turbulent non-premixed H₂ flames,” *Proceedings of the Combustion Institute*, vol. 38, no. 2, pp. 2627–2634, 2021, doi:10.1016/j.proci.2020.06.049.
- [126] S. Lapointe and G. Blanquart, “A priori filtered chemical source term modeling for LES of high Karlovitz number premixed flames,” *Combustion and Flame*, vol. 176, pp. 500–510, Feb. 2017, doi:10.1016/j.combustflame.2016.11.015.
- [127] N. Mukundakumar and R. Bastiaans, “DNS study of spherically expanding premixed turbulent ammonia-hydrogen flame kernels, effect of equivalence ratio and hydrogen content,” *Energies*, vol. 15, 2022, doi:10.3390/en15134749.
- [128] P. Moin and K. Mahesh, “Direct Numerical Simulation: A tool in turbulence research,” *Annual Review of Fluid Mechanics*, vol. 30, no. 1, pp. 539–578, Jan. 1998, doi:10.1146/annurev.fluid.30.1.539.
- [129] T. Schönfeld and M. Rudgyard, “Steady and unsteady flow simulations using the hybrid flow solver avbp,” *AIAA Journal*, vol. 37, pp. 1378–1385, 1999, doi:10.2514/2.636.

- [130] Q. Cazères, P. Pepiot, E. Riber, and B. Cuenot, “A fully automatic procedure for the analytical reduction of chemical kinetics mechanisms for computational fluid dynamics applications,” *Fuel*, vol. 303, p. 121247, 2021, doi:10.1016/j.fuel.2021.121247.
- [131] N. Lamarque, “Schémas numériques et conditions limites pour la simulation aux grandes échelles de la combustion diphasique dans les foyers d’hélicoptère.” Theses, Institut National Polytechnique de Toulouse - INPT, Dec. 2007.
- [132] J.D.Ramshaw and a. P.J.O’Rourke, “Acoustic damping for explicit calculations of fluid flow at low mach number.” Los Alamos National Laboratories, Tech. Rep., 1986.
- [133] R.-H. NI, “A multiple grid scheme for solving the euler equations,” in *5th Computational Fluid Dynamics Conference*. American Institute of Aeronautics and Astronautics, Jun. 1981.
- [134] J. Donea and A. Huerta, *Finite Element Methods for Flow Problems*. Wiley, Apr. 2003.
- [135] O. Colin and M. Rudgyard, “Development of high-order Taylor-Galerkin schemes for LES,” *Journal of Computational Physics*, pp. 338–371, 2000, doi:10.1006/jcph.2000.6538.
- [136] T. Poinso and S. Lelef, “Boundary conditions for direct simulations of compressible viscous flows,” *Journal of Computational Physics*, vol. 101, pp. 104–129, 1992, doi:10.1016/0021-9991(92)90046-2.
- [137] C. Chi, W. Han, and D. Thévenin, “Effects of molecular diffusion modeling on turbulent premixed NH₃/H₂/air flames,” *Proceedings of the Combustion Institute*, vol. 39, no. 2, pp. 2259–2268, 2023, doi:10.1016/j.proci.2022.08.074.
- [138] S. Palle, C. Nolan, and R. S. Miller, “On molecular transport effects in real gas laminar diffusion flames at large pressure,” *Physics of Fluids*, vol. 17, no. 10, pp. 103 601–103 601–19, Oct. 2005, doi:10.1063/1.1990198.

- [139] Z. Zhou, F. E. Hernández-Pérez, Y. Shoshin, J. A. van Oijen, and L. P. de Goey, “Effect of Soret diffusion on lean hydrogen/air flames at normal and elevated pressure and temperature,” *Combustion Theory and Modelling*, vol. 21, no. 5, pp. 879–896, Apr. 2017, doi:10.1080/13647830.2017.1311028.
- [140] X. Wu, “Inflow turbulence generation methods,” *Annual Review of Fluid Mechanics*, vol. 49, no. 1, pp. 23–49, Jan. 2017, doi:10.1146/annurev-fluid-010816-060322.

Paper I

*Direct Numerical Simulation of methane, ammonia-hydrogen and
hydrogen turbulent premixed flames*

Victor Coulon, Jessica Gaucherand, Victor Xing, Davide Laera, Corentin
Lapeyre, Thierry Poinsot
Combustion and Flame, Vol. 256, Page 112933, (2023)

<https://doi.org/10.1016/j.combustflame.2023.112933>



Direct numerical simulations of methane, ammonia-hydrogen and hydrogen turbulent premixed flames

Victor Coulon^{a,*}, Jessica Gaucherand^{a,b}, Victor Xing^a, Davide Laera^{a,c}, Corentin Lapeyre^a, Thierry Poinso^{a,d}

^a CERFACS, 42 avenue Gaspard Coriolis, 31057 Toulouse, France

^b Department of Energy and Process Engineering, Norwegian University of Science and Technology, NO-7034 Trondheim, Norway

^c Department of Mechanics, Mathematics and Management, Polytechnic University of Bari, Via Orabona 4, Bari 70125, Italy

^d IMFT, Allée du Professeur Camille Soula, Toulouse 31400, France

ARTICLE INFO

Article history:

Received 7 December 2022

Revised 28 June 2023

Accepted 30 June 2023

Keywords:

DNS

Premixed

Hydrogen

Methane

Ammonia

Thermo-diffusive instability

ABSTRACT

Three turbulent premixed flames with the same unstretched laminar flame speeds and thicknesses are analyzed and compared using 3D Direct Numerical Simulation (DNS) in a slot burner configuration at atmospheric conditions: a CH₄/air flame at $\phi = 1$, an NH₃–H₂/air (46% vol. H₂) at $\phi = 1$ and an H₂/air flame at $\phi = 0.45$.

While both stoichiometric methane and ammonia-hydrogen flames behave similarly, the lean hydrogen flame brush is twice as short with less flame surface, and exhibits significant alteration of its local flame structure: for the H₂ flame, the thickness of flamelets decreases significantly while burning rates increase drastically. This is observed for flame elements convexly curved with respect to fresh reactants (positive curvature) because of preferential diffusion, where thermo-diffusive instabilities generate long-tail structures that continuously head toward the fresh gases, and also for near-flat flame elements because of local strain effects. Opposite behaviors are observed for flame elements concavely curved (negative curvature) where fuel depletion caused by refocusing of hydrogen and strain effects are unable to increase the consumption, even leading to near-extinction of the flame. The turbulent methane and ammonia-hydrogen flames studied in this work do not exhibit the instabilities seen in the pure hydrogen flame. However, local flame-flame interactions are observed in the cusp regions of all three flames, which significantly increase the displacement speed as well as flame surface destruction.

A 1D-3D comparison indicates that strain effects in regions of low curvature and preferential diffusion effects in regions of positive curvature can be modeled using counterflow flamelets to account for stretch effects on the turbulent hydrogen flame propagation in addition to turbulent wrinkling.

© 2023 The Combustion Institute. Published by Elsevier Inc. All rights reserved.

1. Introduction

Recently, hydrogen and ammonia have been put forward as potential low-carbon energy carriers. Their fuel properties pose challenging problems for the combustion of new sustainable systems, such as the low flammability limit of ammonia or the intrinsic combustion instabilities of lean hydrogen flames [1–3]. Nevertheless, their mixture combines interesting features like increasing ammonia flame speed [4], avoiding hydrogen flame boundary layer flashback [5], mitigating hydrogen thermo-diffusive instabilities [6] and achieving high volumetric energy density for industrial configurations such as piston engines, aircraft engines or industrial burners [7]. However, the influence of intrinsic instabilities of hy-

drogen, or even their existence for ammonia-hydrogen blends, is yet unclear and must be investigated for technological and safety reasons [8,9]. Modeling these flames either as a simple fuel (H₂, NH₃), or as blends (NH₃–H₂), poses a number of fundamental issues to be tackled.

From a numerical point of view, hydrogen raises new challenges even in a fully premixed single-fuel regime. In particular, it is of high interest to accurately predict the rate at which the flame propagates, which is substantially altered by the turbulent field but also by intrinsic flame instabilities. Numerical turbulent calculations with conventional fuels such as methane exhibit only hydrodynamic instabilities [10,11] stemming from gas expansion without significant alteration of their flame structure [12–15]. However, in a lean setup with a fuel characterized by large mass diffusivity compared to molecular heat diffusivity (i.e., Lewis number $Le < 1$), preferential diffusion can affect the turbulent flame

* Corresponding author.

E-mail address: coulon@cerfacs.fr (V. Coulon).

speed. As postulated by Damköler [16], the increase in turbulent flame speed is primarily due to the flame surface enhancement induced by wrinkling, but additional effects on the consumption rates have been ascribed to Lewis number effects. Direct Numerical Simulations (DNS) are necessary to study diffusive phenomena taking place on spatial scales of the order of a few flame thicknesses, still out of reach with current mesh sizes for most Large Eddy Simulations (LES) calculations, especially at high pressures.

For turbulent lean premixed hydrogen flames, DNS with detailed reaction mechanisms have shown that the enhanced burning rates are mainly caused by intrinsic thermo-diffusive instabilities [17–25]. Recent studies [26,27] have demonstrated their impact on lean hydrogen/air flames, even in the absence of turbulence, by deriving growth rates associated with the intrinsic instabilities by mean of dispersion relations using asymptotic methods [28,29]. They show that for a sufficiently weak flame perturbation, the associated growth rate increases exponentially because of intense burning in regions convexly curved with respect to the fresh reactants. In turbulent conditions, the highly corrugated shape of the flame sheet further enhances the preferential diffusion of hydrogen. More specifically, the hydrogen mass diffusivity operates in highly curved regions with strong fluctuations of local equivalence ratio leading to large variability of the fuel reaction rates along the flame front. The pressure is also known to drastically affect the lean hydrogen flame: Rieth et al. [30] have highlighted flames resilient to strain effects with narrower reaction zones due to an intensification of hydrogen diffusive fluxes with respect to convective fluxes in lean conditions with $\phi = 0.3$, and preheated conditions with $T_{in} = 750\text{K}$. The authors were also able to retrieve similar behavior of pressurized flames at atmospheric pressure by keeping constant parameters such as Markstein, effective Lewis, Zeldovich and Peclet numbers.

Mixtures of ammonia and hydrogen are also of interest [31] and a question emerges as to the impact of the additional hydrogen on the ammonia flame response. Recently, Wiseman et al. [15] and Rieth et al. [32] have shown that $\text{NH}_3 - \text{H}_2 - \text{N}_2/\text{air}$ (NH_3 : 40%, H_2 : 45%, N_2 : 15% vol.) mixture leads to thermo-diffusively unstable turbulent flame at $\phi = 0.45$ and $T_{in} = 750\text{K}$. More generally, the interplay between turbulence and intrinsic flame instabilities on the overall turbulent flame is still the subject of active research efforts, especially concerning pure hydrogen and hydrogen-enriched fuels. While several methane/air flames have also been investigated in previous works [12–15,33], this study aims to compare Lewis number effects on three different flames: methane/air, ammonia-hydrogen/air and hydrogen/air. This is accomplished by DNS simulations of such flames in a turbulent premixed Bunsen-like configuration (slot burner) at atmospheric conditions. The three flame compositions (CH_4 , $\text{NH}_3 - \text{H}_2$ and H_2) are chosen to match the unstretched laminar flame speed and thickness of the stoichiometric methane mixture, and each flame is subjected to the same turbulence forcing. Section 2 describes the DNS solver and computational methodology. Results are outlined in Section 3, with a description of each flame's geometry, followed by an investigation of flame structures and the interplay between Lewis numbers and turbulence effects on the turbulent flame speeds. To further investigate stretch effects on the pure hydrogen flame dynamics, an additional 1D - 3D analysis between DNS and counterflow flamelets is conducted. It highlights the role of the strain effects on near-flat flame elements weakly affected by preferential diffusion.

2. Computational methodology and configurations

2.1. Transport and chemical kinetics

Molecular viscosity μ is approximated with a power law $\mu = \mu_{ref}(T/T_{ref})^b$ and the reference parameter values of all cases are



Fig. 1. Physical domain of 3D DNS cases. The inlet contains a central region of width $H = L_y/3$ with fresh gases at bulk velocity U_{bulk} and velocity fluctuations u' (homogeneous isotropic turbulence) surrounded by two laminar coflows at equilibrium state and velocity U_{coflow} .

provided in Table A.1 of the supplementary material. The heat conduction coefficient of each mixture, λ , is computed with a constant Prandtl number around 0.7 for each mixture¹ as $\lambda = \mu C_p / Pr$, where C_p is the mixture-averaged mass-specific heat capacity. Molecular diffusion coefficients D_k are computed from the Schmidt number of each k th species, assumed to be constant in time and space.

Methane/air kinetics is described through a single-step mechanism (5 species, 1 reaction) [34] using a polynomial estimation based on an analytical solution of the 1D laminar transport equation of the progress variable c [35–37]. Hydrogen chemistry is modeled using the San Diego mechanism (9 species and 21 reactions) [38]. An analytically reduced chemistry mechanism, derived from CRECK [39] and reduced with Arcane [40], is used to model the chemistry of the ammonia-hydrogen blend (14 species, 7 species with QSS assumption and 174 reactions).² Validation of the $\text{NH}_3 - \text{H}_2$ scheme for laminar flames is provided in Fig. B.1 of the supplementary material.

2.2. Setup of the simulations

Fig. 1 illustrates the configuration used in this work. It corresponds to a slot burner turbulent flame, where burnt gases at equilibrium surround a rectangular slot injecting fresh premixed gases. All calculations are performed with the compressible solver AVBP³ [41], an explicit massively-parallel code solving the conservation of mass, momentum, energy and species equations. A third-order accurate in space and time Taylor-Galerkin finite-element scheme is used for the discretization of the convective terms, while a second-order Galerkin scheme is used for diffusion terms [42]. Domains are rectangular with dimensions $L_x \times L_y \times L_z$. Axial dimensions L_x have been chosen using preliminary estimations of flame brush lengths. $L_y = 25.6\text{mm}$ to avoid interference with lateral boundaries,

¹ Mixtures are mainly composed of air.

² The reduced mechanism for $\text{NH}_3 - \text{H}_2$ flame is detailed as supplementary material, and available at <https://chemistry.cerfacs.fr/>.

³ <http://www.cerfacs.fr/avbp7x>.

and $L_z = 12.8\text{mm}$ to average in the transverse direction. Domains are discretized on regular Cartesian meshes composed of $N_x \times N_y \times N_z$ hexahedral cells of size Δx . Laminar 1D planar unstretched flamelets were first computed, initialized with Cantera [43] solutions, to determine the spatial resolution of species mass fractions, temperature and density profiles and choose an adequate number of points (N_c) in each thermal thickness δ_L^0

$$\delta_L^0 = \frac{T_b - T_u}{\max(|\nabla T|)}. \quad (1)$$

A mesh convergence study was performed on the H_2 case to ensure that Lewis effects were captured (see Section C of the supplementary material). The inlet boundary condition is separated into three parts along the y direction. A central jet of width $H = L_y/3$ injects a flow of fresh turbulent gases at the bulk velocity $U_{bulk} = 25\text{ms}^{-1}$. Turbulence in this central jet is homogeneous and isotropic (HIT) with \mathbf{u}' obtained by a synthetic generation method built from a Fourier series decomposition [44]

$$\mathbf{u}'(\mathbf{r}, t) = \sum_{n=1}^N \mathbf{v}^n(\mathbf{k}^n) \cos(\mathbf{k}^n \mathbf{r} + \omega^n t) + \mathbf{w}^n(\mathbf{k}^n) \sin(\mathbf{k}^n \mathbf{r} + \omega^n t), \quad (2)$$

with $N = 200$ modes. The Fourier modes $\{\mathbf{v}^n, \mathbf{w}^n\}$, wavevectors \mathbf{k}^n , and pulsations ω^n are random variables sampled to obtain a Passot-Pouquet [45] turbulence spectrum

$$E(k) = 16 \frac{u'^2}{k_e} \sqrt{\frac{2}{\pi}} \left(\frac{k}{k_e}\right)^4 \exp\left[-2\left(\frac{k}{k_e}\right)^2\right], \quad (3)$$

where $u' = 2.5\text{ms}^{-1} = U_{bulk}/10$ is the turbulent fluctuation intensity and k_e is the wavenumber associated with the most energetic lengthscale. k_e is related to the integral lengthscale l_t of the spectrum through $l_t = \sqrt{2\pi}/k_e$, and its value is chosen to obtain $l_t = 2.1\text{mm} = H/4$. Two slow laminar coflows of burnt gases at the axial velocity $U_{coflow} = 0.1\text{ms}^{-1}$ are imposed on both sides of the central jet. Their composition corresponds to the burnt gas states of the central mixture. A spectral analysis shows that the shear-induced turbulence is not expected to have enough time to become fully developed since the flames add significant viscous dissipation, so that the three turbulent flames are mainly controlled by the injected HIT in the fresh gas stream (see Section D of the supplementary material).

For all cases, global equivalence ratios ϕ_{global} , fuel Lewis number $Le_f = \lambda \rho C_p D$, Karlovitz numbers $Ka = (l_t/\delta_L^0)^{-1/2} (u'/S_L^0)^{3/2}$, Reynolds numbers $Re = U_{bulk} H \nu$, turbulent Reynolds numbers $Re_t = (l_t/\eta_k)^{4/3}$, lengths and numbers of points in x -, y -, z -direction L_x , L_y , L_z , N_x , N_y , N_z respectively, cell sizes Δx , timesteps Δt , numbers of points in thermal thickness $N_c = \delta_L^0/\Delta x$ and Kolmogorov scales resolutions $\eta_k \Delta x$ [46] are reported in Table 1. The pure methane flame is characterized by $Le_{CH_4} = 1$, while $Le_{NH_3} \approx 0.9$ and $Le_{H_2} \approx 0.3$ for the two other flames. The Lewis number of the ammonia-hydrogen flame is $Le_{blend} \approx 0.6$ and is computed with Eq. (4) [47]

$$Le_{blend} = X_{NH_3} Le_{NH_3} + X_{H_2} Le_{H_2} \quad (4)$$

where X_i and Le_i are the molar mass fractions and the Lewis numbers of each fuel defining the blend.

The flames are computed at $T_u = 300\text{K}$ and $P = 1\text{bar}$ and global equivalence ratios have been chosen to reach the unstretched laminar flame speed and flame thickness of the stoichiometric methane mixture with $S_L^0 \approx 0.38\text{ms}^{-1}$ and $\delta_L^0 \approx 450\mu\text{m}$. Both methane/air and ammonia-hydrogen/air mixtures are at stoichiometry whereas

Table 1
Parameters of 3D DNS calculations.

Case	CH_4	$\text{NH}_3\text{-H}_2$	H_2
ϕ_{global}	1	1	0.45
Le_f	1	≈ 0.6	≈ 0.3
T_{ad} [K]	2330	2140	1535
Ka	7.8	7.8	7.7
Re	14 220	11 985	10 830
Re_t	355	313	271
L_x [mm]	12H	10.5H	6H
L_y [mm]	3H	3H	3H
L_z [mm]	1.5H	1.5H	1.5H
N_x	1601	2191	1281
N_y	401	627	641
N_z	201	314	321
Δx [μm]	64	41	40
Δt [μm]	≈ 0.062	≈ 0.040	≈ 0.043
N_c	≈ 7	≈ 11	≈ 11
$\eta_k/\Delta x$	≈ 0.5	0.7	0.8

the pure hydrogen/air mixture is lean with $\phi_{global} = 0.45$. Simulations are initialized with burnt conditions inside the domain before beginning the injection of fresh gases at the inlet boundary. In the fresh-burnt transition region, species mass fraction and temperature profiles are set to follow the unstretched laminar flames profiles, and a smooth transition from U_{bulk} to U_{coflow} is enforced through a hyperbolic tangent function. The domain is periodic in the spanwise direction (z), no-slip conditions are specified in the crosswise direction (y) and static pressure is imposed at the outlet. Both inlet and outlet boundary conditions are treated with the Navier–Stokes Characteristic Boundary Conditions (NSCBC) [48]. In the following, averaging begins after one transient flow-through time τ , with $\tau = L_x/U_{bulk}$ defined in terms of axial length and central jet velocity, to ensure a statistically-steady state. While ammonia-hydrogen and pure hydrogen flames match the methane unstretched laminar flame speed and thickness, the adiabatic temperatures are not exactly the same, leading to variations in viscosity of the burnt gases and a mismatch in the gas expansion ratio. Therefore, 2D simulations were first conducted to ensure the similarity of flame lengths in the absence of turbulence (see Section E of the supplementary material).

3. Results and discussions

All three flames are forced using the same homogeneous and isotropic turbulent flow field (Section 2.2) in the central bulk flow imposed at the inlet boundary condition (Fig. 1). The corresponding regimes based on inlet HIT parameters are located in the thin reactions zones (TRZ) in the Borghi-Peters diagram [49,50] as recent DNS works (Fig. 2). Classification of turbulent combustion regimes should be interpreted with care [50–53]. Note that the three flames are premixed: viscosity is mainly controlled by the high N_2 content which is the same for all flames. Further, density fields are very similar so that u' and l_t , as well as Re_t , are the same. Since laminar flame speeds and thicknesses are also conserved in this study, the three flames remain in the same regime in the diagram.

3.1. Overview of the three flames and stretch effects

Fig. 3 shows isosurfaces based on progress variable values at maximum HRR in the corresponding 1D unstretched laminar flame. A drastic difference between the hydrogen flame and the other two is observed with a turbulent hydrogen flame brush much shorter than the methane and the ammonia-hydrogen flames. This result correlates with high H_2 heat release rates (HRR), which increase up to three times the maximum corresponding 1D

⁴ Timesteps are limited by the Courant-Friedrichs-Lewy (CFL) condition with $CFL = 0.7$.

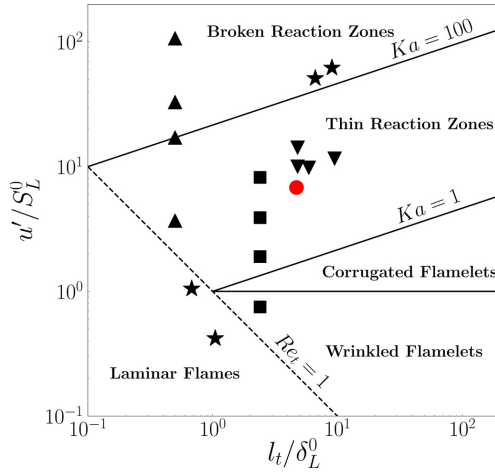


Fig. 2. Borghis-Peters turbulent combustion diagram. ●: present cases; ▼: Luca et al. 2019 [14] (CH₄); ■: Aspden et al. 2015 [22] (H₂); ★: Rieth et al. 2021 [32] (NH₃-H₂, H₂); ▲: Savard et al. 2014 [21] (H₂).

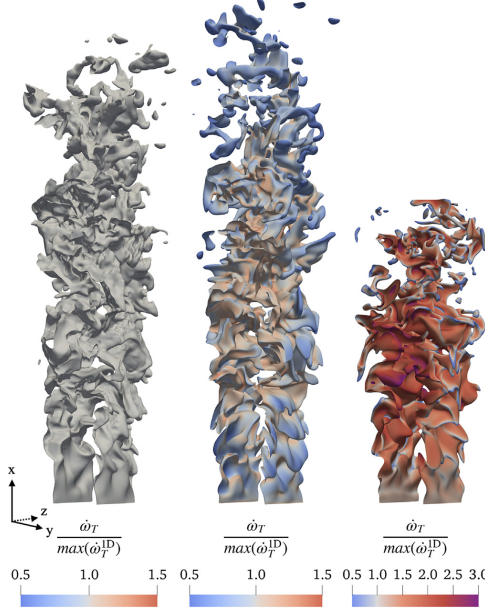


Fig. 3. Isosurfaces of $c = c^*$, retrieved at $t = 2\tau$ and colored by HRR normalized by the maximum value in the corresponding 1D unstretched laminar flame for all cases. CH₄ case at $c_{H_2}^0 = 0.72$ (left), NH₃-H₂ case at $c_{H_2}^0 = 0.78$ (center), H₂ case at $c_{H_2}^0 = 0.85$ (right). (For interpretation of the references to color in this figure, the reader is referred to the web version of this article.)

flamelet rate, on flame elements curved with the center of curvature into the burnt gases (often called leading edges). In contrast, the H₂ heat release rates almost vanish on flame elements curved with the center of curvature into the fresh gases (or trailing edges). The same tendency is observed for the ammonia-hydrogen case, but the normalized heat release rates are centered around unity and the overall brush length is still approximately the same as for the methane case similarly to the 2D calculations.

For a mixture characterized by equidiffusion ($Le \approx 1$), the increase in fuel consumption is mainly caused by the flame surface enhancement. Generally, the progress variable value at HRR peak in 1D flame, $c = c^*$, is used to define an isosurface representative of the reaction zone, with $c = 1 - Y_f / Y_{f,u}$ where Y_f is the fuel mass fraction⁵ and $Y_{f,u}$ its value in the unburnt gases. Both production and destruction of this isosurface are described by the transport equation for the flame surface density (FSD), $\Sigma(c^*) = |\nabla c| \delta(c - c^*)$ [54–56], where δ is the Dirac delta function.

$$\frac{\partial \Sigma}{\partial t} + \nabla \cdot ((\mathbf{u} + S_d \cdot \mathbf{n})_S \Sigma) = (K)_S \Sigma. \quad (5)$$

The surface average of a generic quantity Q on this isosurface, $\langle Q \rangle_S$, is defined by Eq. (6)

$$\langle Q \rangle_S = \frac{\langle Q \rangle |\nabla c| |c^*}{\langle |\nabla c| |c^* \rangle}. \quad (6)$$

with $\langle \bullet | c^* \rangle$ representing the conditional mean with respect to c^* . In stationary regime, the FSD is convected by both the flow field velocity \mathbf{u} and the normal component of the displacement speed $S_d \cdot \mathbf{n}$. The RHS term of Eq. (5) represents the FSD source term proportional to the total stretch, K . Details on S_d and K are provided in Section F of the supplementary material.

To assess how the flames are impacted by stretch effects in addition to wrinkling, the stretch factor I_0 is introduced and linked to the turbulent consumption flame speed S_T by Eq. (7)

$$\frac{S_T}{S_L^0} = \frac{A_T}{A_0}, \quad (7)$$

where S_L^0 is the unstretched laminar flame speed and S_T refers to the turbulent flame consumption speed defined by Eq. (8).

$$S_T = - \frac{1}{\rho_u Y_{f,u} A_0} \int_{\Omega} \dot{\omega}_f dV, \quad (8)$$

with ρ_u the density in the unburnt gases and Ω the whole domain volume. A_0 is a reference surface while A_T represents a generalized turbulent flame surface and is linked to the flame surface density by integrating Σ over the entire flame structure [51,57] as defined by Eq. (9)

$$A_T = \int_0^1 \Sigma(c^*) dc^* = \int_{\Omega} |\nabla c| dV. \quad (9)$$

Finally, the stretch factor I_0 accounts for strain and curvature effects on flame elements in turbulent flows [58,59]. Several methods for estimating the stretch factor are reported in the literature: (i) compute the surface-averaged consumption speed from S_L^0 , with the speeds calculated by integrating the fuel source terms normal to the flame front [18,24,60]. Or, (ii) compute both speed and surface enhancements in Eq. (7), then indirectly retrieve I_0 [25,30]. To avoid the computation of the reference surface A_0 , a total volumetric burning rate can be instead computed as proposed in [33]. Another simplification is to (iii) retrieve the deviation of the surface-averaged density-weighted displacement speed from $\rho_u S_L^0$ on a single isosurface assumed to be representative of the reaction zone,

⁵ For the NH₃-H₂ flame, the water mass fraction Y_{H_2O} is instead used.

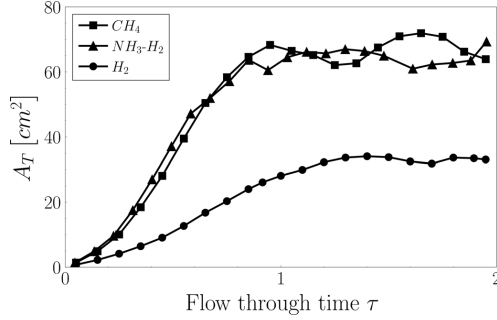


Fig. 4. Temporal evolution of the overall 3D turbulent flame surfaces A_T computed with Eq. (9).

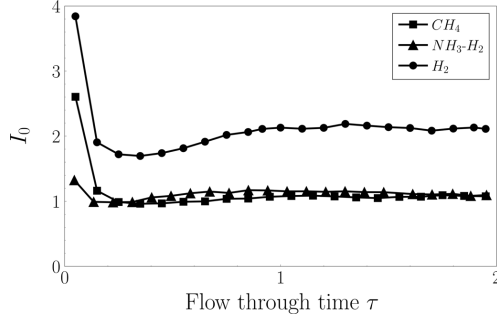


Fig. 5. Temporal evolution of the stretch factor I_0 for the turbulent 3D cases computed as Attili et al. [33].

as $I_0^* = (\tilde{S}_d)_s / S_L^0$ [61–65], where $\tilde{S}_d = S_d \rho / \rho_u$ to account for density changes due to gas expansion. Therefore, the stretch factor I_0 should be considered as a global parameter accounting for local variations in the whole flame structure, i.e., fuel reaction rate and gradient (or thickness) internal variations. Note that the global stretch factor I_0 is generally assumed of order unity in many flamelet models [66], which is generally true for a fuel characterized by $Le \approx 1$ [16]. In the following, the last two approaches are used to evaluate I_0 and I_0^* .

Fig. 4 shows the temporal evolution of turbulent flame surfaces. While the methane and ammonia-hydrogen flames exhibit the same turbulent flame surface, the hydrogen flame is significantly shorter with less surface than the two other flames. Fig. 5 shows that once flames have reached a stationary regime, I_0 goes to unity for both methane and ammonia-hydrogen flames while super-unity values of the stretch factor are observed for hydrogen, indicating that the H_2 flame consumes the fresh reactants faster than the other cases. Note that even higher I_0 values have been reported in a recent similar hydrogen/air DNS calculation in leaner conditions [25]. The following sections provide a more detailed understanding of the evolution of flame surfaces, followed by an assessment of each internal flame structure.

3.2. Geometrical description

To investigate the production and destruction of flame surface along the streamwise direction (x), Figs. 6, 9 and 10 show surface-averaged stretch, curvature and displacement speed along the ax-

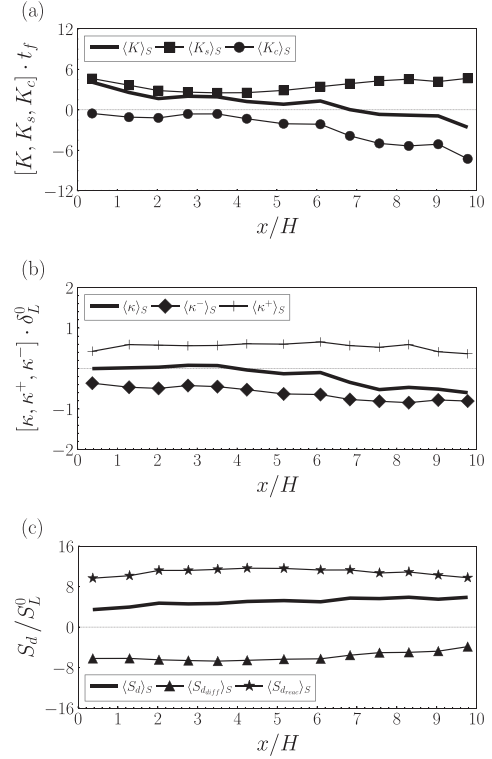


Fig. 6. CH_4 flame: surface-averaged total stretch K and its contributions K_s , K_c (a), total curvature κ and its contributions κ^- , κ^+ (b), displacement speed S_d and its contributions $S_{d,off}$, $S_{d,rec}$ (c) retrieved on the isosurface of $c_{CH_4}^* = 0.72$, at $t = 2\tau$.

ial position x for CH_4 , NH_3-H_2 and H_2 cases, respectively. The total stretch K and its strain (K_s) and curvature (K_c) terms are normalized with a flame characteristic time $t_f = \delta_L^0 / S_L^0$. The curvature, κ , is defined by $\kappa = \nabla \cdot \mathbf{n}$, with $\mathbf{n} = -\nabla c / |\nabla c|$ the normal vector to the flame front pointing toward the fresh gases, and is normalized by the laminar unstretched flame thickness. Its negative and positive contributions, κ^- and κ^+ , are defined by Eqs. (10) and (11), respectively

$$\kappa^- = \int_{-\infty}^0 \kappa \mathcal{P}(\kappa) d\kappa, \quad (10)$$

$$\kappa^+ = \int_0^{+\infty} \kappa \mathcal{P}(\kappa) d\kappa, \quad (11)$$

where $\mathcal{P}(\kappa)$ is the probability to find curvature value κ . Furthermore, Kernel Density Estimate (KDE) between displacement speed and curvature are provided in Figs. 7, 8 and 11(b-c) to quantify their relationship on the flame surfaces, and are completed by instantaneous isosurfaces of c^* to gain qualitative insights.

In the first region of the CH_4 flame ($x/H \leq 7$), equivalent positive and negative curvature values are observed (Figs. 6b and 7c). As a result, the enhancement of flame surface is mainly controlled by strain effects, as shown in Fig. 6a. On the contrary, in the second region of the flame ($x/H > 7$), a flame surface destruction occurs as the flame is convected downstream, i.e., a zone where the

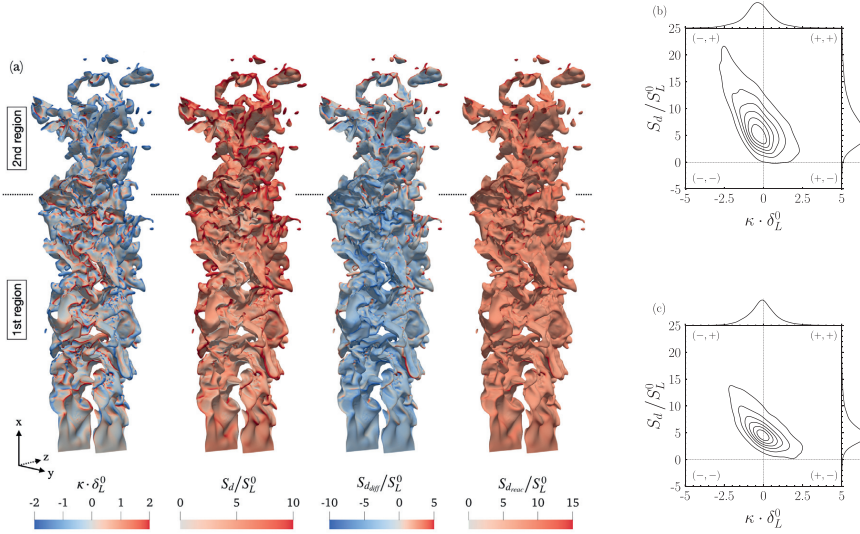


Fig. 7. CH₄ flame: instantaneous isosurface of $c_{CH_4}^* = 0.72$ at $t = 2\tau$, colored by curvature κ , total displacement speed S_d alongside its diffusive and reactive contributions $S_{d,diff}$, $S_{d,react}$, respectively (a). Kernel Density Estimates of the displacement speed S_d with curvature κ , retrieved on the isosurface of $c_{CH_4}^* = 0.72$ at $t = 2\tau$ in the first region $x/H \leq 7$ (c) and in the second region $x/H > 7$ (b). (For interpretation of the references to color in this figure, the reader is referred to the web version of this article.)

negative curvature is prevailing due to extreme cusp regions and flame detachments in the rear of the flame brush (Fig. 7a) [67]. Hence, the curvature term K_C becomes dominant and this effect results in a further deviation of the displacement speed from S_L^0 as shown in Fig. 6c, which however remains positive, leading to a

local drastic surface destruction (top left quadrant in Fig. 7b) referred to as kinematic restoration [68]. Lagrangian investigations have shown that the strong increase in S_d in this region is induced by flame-flame interactions [69,70], which modify heat and species diffusive fluxes. To better visualize this effect, diffusive and reac-

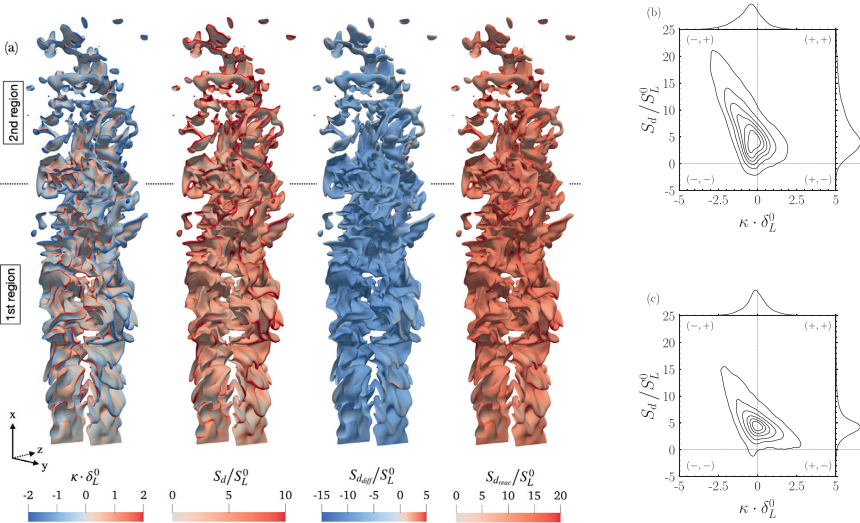


Fig. 8. NH₃-H₂ flame: instantaneous isosurface of $c_{H_2,O}^* = 0.78$ at $t = 2\tau$, colored by curvature κ , total displacement speed S_d alongside its diffusive and reactive contributions $S_{d,diff}$, $S_{d,react}$, respectively (a). Kernel Density Estimates of the displacement speed S_d with curvature κ , retrieved on the isosurface of $c_{H_2,O}^* = 0.78$ at $t = 2\tau$ in the first region $x/H \leq 7$ (c) and in the second region $x/H > 7$ (b). (For interpretation of the references to color in this figure, the reader is referred to the web version of this article.)

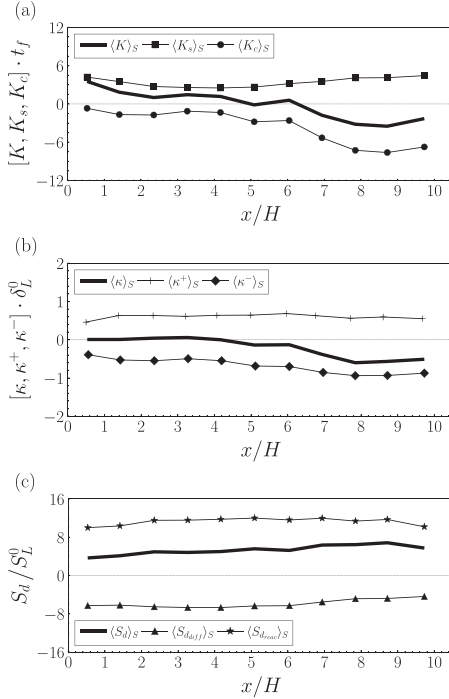


Fig. 9. $\text{NH}_3\text{-H}_2$ flame: surface-averaged total stretch K and its contributions K_s, K_c (a), total curvature κ and its contributions κ^-, κ^+ (b), displacement speed S_d and its contributions S_{diff}, S_{dnc} (c) retrieved on the isosurface of $c_{H_2}^0 = 0.78$, at $t = 2\tau$.

tive components of S_d (see Eq. (F.4) in the supplementary material) are plotted in Figs. 6c and 7a. These interactions enhance the diffusive fluxes leading to larger S_d values in the cusp regions of the flame.⁶

According to Fig. 9a, similar surface evolution is observed for the ammonia-hydrogen case, where the curvature term K_c starts to control the flame surface destruction around $x/H \approx 7$.

Fig. 9c indicates however that the diffusive fluxes are less impacted at the trailing edges due to weaker flame-flame interactions. This can also be observed in Fig. 8a, where almost no positive values of S_{diff} are retrieved in the extreme cusp regions.⁷ However, greater variations in heat release rate are observed in this case. Therefore, KDEs in Fig. 8b and c also show higher displacement speeds on negatively curved flame elements in both flame regions. This case even yields negative displacement speeds in regions of small negative curvature, where the diffusive contribution counterbalances the small reactivity and leads to a small surface production (bottom left quadrants of Figs. 8b and c).

When considering the hydrogen case, the total stretch K is a positive FSD source term until $x/H \approx 3.5$ (Fig. 10a). In the first region, the surface dilatation by propagation hardly contributes to the flame surface, with $K_c \approx 0$, since both production and destruc-

⁶ In this case, the tangential component of diffusive fluxes overcompensates the normal component (see Fig. G.1 in the supplementary material).

⁷ In this case, the normal component of the diffusive fluxes overcompensates the tangential component (see Fig. G.2 in the supplementary material).

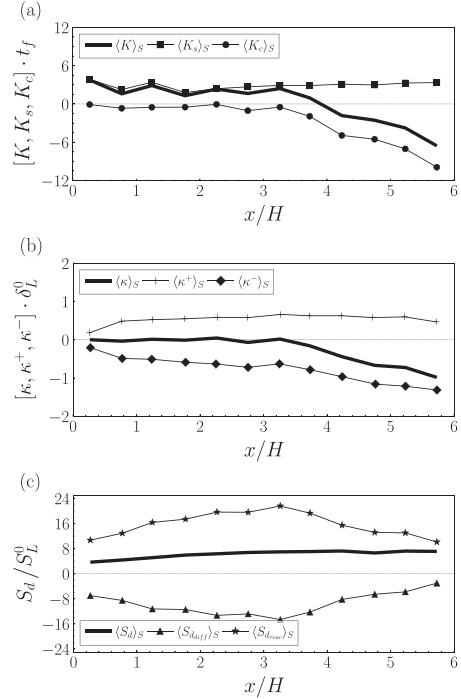


Fig. 10. H_2 flame: surface-averaged total stretch K and its contributions K_s, K_c (a), total curvature κ and its contributions κ^-, κ^+ (b), displacement speed S_d and its contributions S_{diff}, S_{dnc} (c) retrieved on the isosurface of $c_{H_2}^0 = 0.85$, at $t = 2\tau$.

tion are balanced in this case (Fig. 11c). This effect is induced by the thermo-diffusive instabilities generating long-tail structures that continuously head toward the fresh reactants, associated with large heat release rates at the leading edges. Hence, excursions of S_d from S_d^0 shown in Fig. 10c originate from intense heat release rates, which in this case, even unbalance the large H_2 diffusive fluxes. The switch between both stretch contributions is occurring more upstream than the previous cases due to the intense burning in the first region. Furthermore, strong flame-flame interactions are observed with positive values of S_{diff} in the extreme cusp regions (Fig. 11a), where the heat release rates almost vanish which is generally known as tip-opening for lean hydrogen flames [71,72]. As a result, the diffusive contribution of S_d is strongly shifted toward positive values in Fig. 10a, and the reactive contribution plays a minor role on the flame surface destruction in regions of large negative curvature compared to the previous cases, thus explaining the lower values of S_d at negative curvature observed in Fig. 11b and c (see also Fig. H.1 in the supplementary material). A possible explanation for the larger flame-flame interactions observed in this case, is that the strong flame propagation toward the fresh reactants, induced by thermo-diffusive instabilities, extends the elongated and narrow regions surrounded by burnt gases, further increasing the tangential diffusive fluxes.⁸

⁸ In this case, the diffusive fluxes tangent to the flame front, and proportional to curvature, dominate in the cusp regions even if intense normal diffusive fluxes

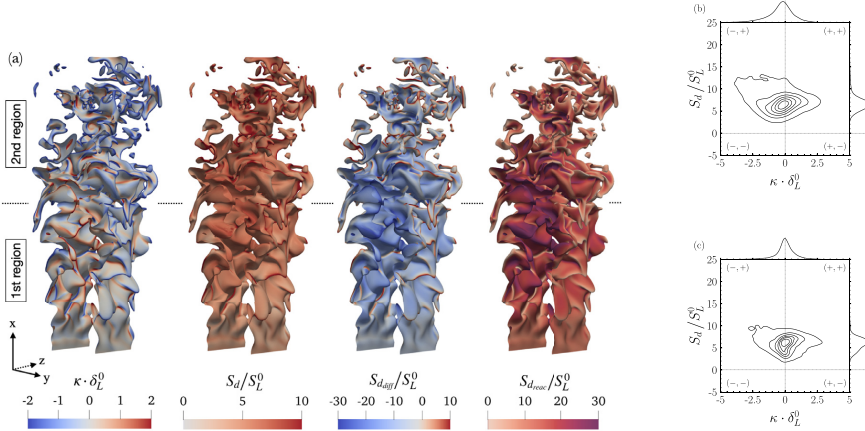


Fig. 11. H₂ flame: instantaneous isosurface of $c_{H_2} = 0.85$ at $t = 2\tau$, colored by curvature κ , total displacement speed S_d alongside its diffusive and reactive contributions $S_{d, diff}$, $S_{d, reac}$, respectively (a). Kernel Density Estimates of the displacement speed S_d with curvature κ , retrieved on the isosurface of $c_{H_2} = 0.85$ at $t = 2\tau$ in the first region $x/H \leq 3.5$ (c) and in the second region $x/H > 3.5$ (b). (For interpretation of the references to color in this figure, the reader is referred to the web version of this article.)

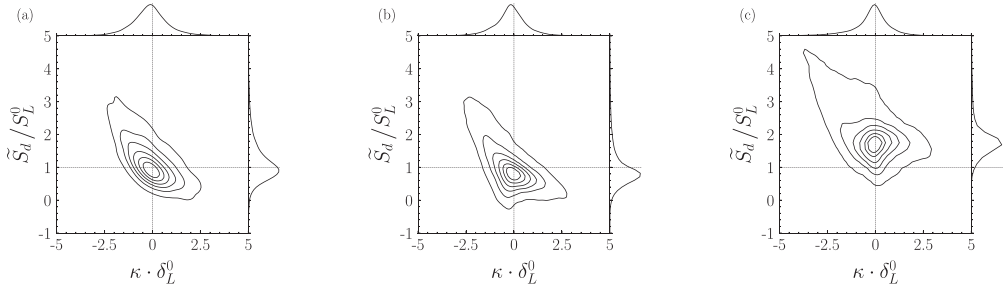


Fig. 12. Kernel Density Estimates of the density-weighted displacement speed \tilde{S}_d with curvature κ , retrieved on the isosurfaces of c^* at $t = 2\tau$ for CH₄ case (a), NH₃-H₂ case (b), and H₂ case (c).

Another estimation of stretch effects is obtained now by averaging the displacement speed on the isosurface of c^* (approach (iii) in Section 3.1). Fig. 12 shows KDEs between \tilde{S}_d and κ over each entire flame brush. The mean values of the marginal PDFs of \tilde{S}_d/S_d^0 represent the stretch factor I_0^* . Although the scalar value of the progress variable at maximum HRR might be dependent on the local mixture variations, I_0^* is close to the global stretch factor I_0 for all cases. As a result, the displacement speeds recovered from the isosurfaces of c^* give a reasonable approximation of the overall propagation for all cases [65]. Note that flame-flame interactions strongly modify the flame structure in the cusp regions, where extreme values of I_0^* and flame surface annihilation are observed for each case (see Section I of the supplementary material) similarly to the results shown by Dave et al. [69,70].

3.3. Local states description

To examine the three flames locally, domain volume of all cases have been axially-sampled into subvolumes \mathcal{V}^* spanning the cross-wise (y) and spanwise (z) directions to obtain statistically con-

verged quantities, as done in [25,33]. Then, turbulent flame speeds and surfaces have been computed on each \mathcal{V}^* , and temporal averages lead to S_T and A_T . Similarly, the reference flame surface A_0 has been computed using Eq. (9) with the Favre-averaged progress variable fields by performing a filtering operation with a Gaussian kernel of width Δ iteratively determined with Cantera calculations to obtain a filtered flame thickness⁹ $\bar{\delta}_L^0 \approx N_c^{LES} \Delta \chi^{LES}$, with $\Delta \chi^{LES} = R \Delta x$, $R = 6$ is an arbitrary downsampling factor and $N_c^{LES} = 5$ is a typical number of points in the thermal thickness of a LES calculation.

Fig. 13 shows the spatial evolution of A_T/A_0 , S_T/S_L^0 and I_0 for each flame. In all cases, flame surfaces increase in the first flame regions before being destroyed by the mechanisms discussed in the previous section. For the CH₄ case, the large increase in turbulent flame speed S_T is linked to the increase in flame surface since the equidiffusion of the mixture does not impact the local states of this flame ($I_0 \approx 1$) [14,33]. Super-unity values of I_0 observed for the second region ($x/H > 7$) in Fig. 13 might be linked to the increase in turbulent intensity along the streamwise direction

⁹ are clearly oriented toward adjacent flame fronts (see Fig. G.3 in the supplementary material).

⁹ The filtered flame thickness $\bar{\delta}_L^0$ is obtained by using Eq. (1) on filtered temperature field \bar{T} .

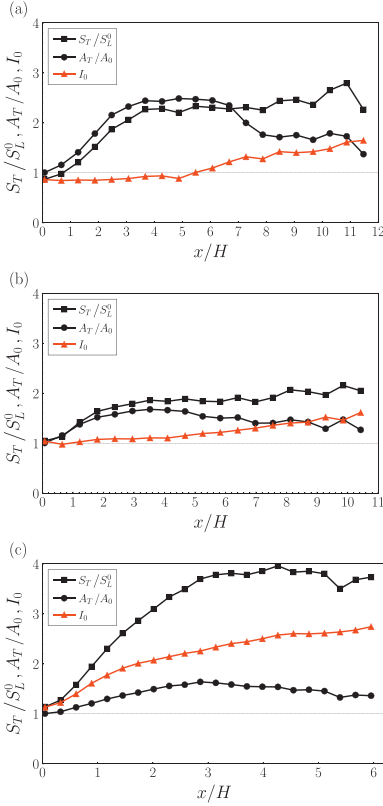


Fig. 13. Streamwise evolution of A_T/A_0 , S_T/S_L^0 and I_0 for CH₄ case (a), NH₃-H₂ case (b) and H₂ case (c). Statistics are performed on all the snapshots for which the flames are statistically stabilized ($\tau < t < 2\tau$).

leading to lower turbulent advection time scales (associated to the flame surface destruction) than the molecular times scales (associated to diffusive transport) resulting in higher Karlovitz numbers as discussed by Rieth et al. [32]. Therefore, locally A_T decreases more strongly than the drop-off of S_T/S_L^0 , which increases incrementally the stretch factor I_0 further downstream. A similar trend is observed for the NH₃-H₂ case indicating that the flame structure is not altered by preferential diffusion effects of hydrogen in this case. In contrast, for the H₂ flame, the stretch factor grows from

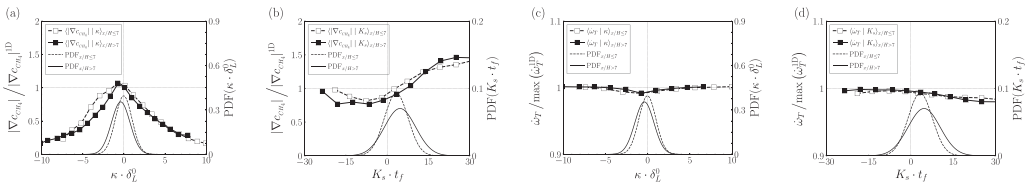


Fig. 14. CH₄ flame: averages of $|\nabla c_{CH_4}|$ and ω_T conditioned by κ (a, c) and K_0 (b, d) in the first ($x/H \leq 7$) and second region ($x/H > 7$). Parameters are retrieved on the isosurface of $c_{CH_4}^* = 0.72$, at $t = 2\tau$. Progress variable gradients are normalized with $|\nabla c_{CH_4}|^{1D}$ computed from the corresponding 1D unstretched laminar flame at $c_{CH_4}^* = 0.72$.

$I_0 \approx 1$ at the flame foot to $I_0 \approx 2.5$ at the tip, more than the flame wrinkling factor [25]. As a comparison, this was not observed in calculations performed at richer conditions with $\phi = 0.7$ and atmospheric conditions [73,74], indicating that the impact of stretch on a hydrogen/air mixture in lean conditions depends strongly on the operating point.

To assess how the flame structures are altered by the flame-turbulence interaction, Figs. 14, 15 and 16 show $|\nabla c|$ and ω_T conditionally averaged with respect to curvature and strain. Progress variable gradients are normalized with respect to the flamelet gradient at $c = c^*$. The heat release rate is normalized by the maximum value of the flamelet at $c = c^*$.

For the methane flame, the normalized progress variable gradients shown in Fig. 14a are below unity for both large negative and positive curvature values, indicating a substantial thickening of the flame front in comparison with the flamelet structure. The larger gradients (linked to thinner flame fronts) are located on flame elements that are almost not curved ($\kappa \approx 0$). In contrast, large positive tangential strain rates cause a substantial increase in the gradients (Fig. 14b). However, when compared with the corresponding flamelet, HRR is not enhanced by curvature (note the small scale in Fig. 14c). A small decrease in HRR is noted at zero curvature where the CH₄ flame burns slightly less when strained, as also confirmed by the decreasing trend when K_0 is increasing as shown in Fig. 14d.

The NH₃-H₂ case gives nearly the same results in terms of progress variable gradients as those observed for the CH₄ case, with a thinner flame front around $\kappa \approx 0$ and for large positive values of K_0 . A slight thinning of the flame front is nevertheless observed for positive of curvature (Fig. 15a), indicating a small flame response to convexly curved flame elements. Besides, the normalized HRR exhibits larger variations than the CH₄ case but remains below unity, under both curvature and tangential straining effects (Figs. 15a and d). As a result, stretch effects slightly modify the structure of the NH₃-H₂ flame leading to averaged burning rates below the maximum 1D flamelet rate all along the flame, and the flame brush extends to the same length as observed for CH₄ case. This result is specific to the stoichiometric conditions and mixture proportions used in this study.

Fig. 16 shows that the H₂ flame behaves differently with a greater alteration of its structure. As noted by Berger et al. [25], the lean hydrogen flame is mostly thickened at negative curvatures while large progress variable gradients are retrieved at both zero and positive curvatures (Fig. 16a). An asymmetry with respect to zero curvature is also retrieved, especially compared with the methane flame [12,75]. A significant flame response to curvature is also shown in terms of heat release rate. Large negative curvature values are related to a decrease in HRR and thereby the local consumption rates. In contrast, substantial HRR are obtained on flat flame elements, and even more at positive curvature, where deviations from the laminar behavior exceed a factor three (Fig. 16c) due to H₂ preferential diffusion effects (see also Fig. J.3 of the supplementary material). As a result, the global and lean equivalence ratio of $\phi_{global} = 0.45$ is not maintained along the corrugated flame

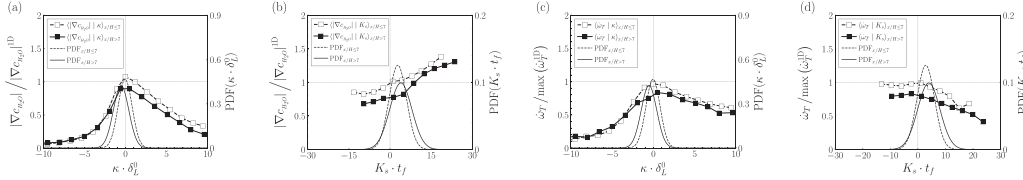


Fig. 15. $\text{NH}_3\text{-H}_2$ flame: averages of $|\nabla c_{\text{H}_2\text{O}}|$ and ω_T conditioned by κ (a, c) and K_s (b, d) in first ($x/H \leq 7$) and second region ($x/H > 7$). Parameters are retrieved on the isosurface of $c_{\text{H}_2\text{O}} = 0.78$, at $t = 2\tau$. Progress variable gradients are normalized with $|\nabla c_{\text{H}_2\text{O}}|^{\text{1D}}$ computed from the corresponding 1D unstretched laminar flame at $c_{\text{H}_2\text{O}} = 0.78$.

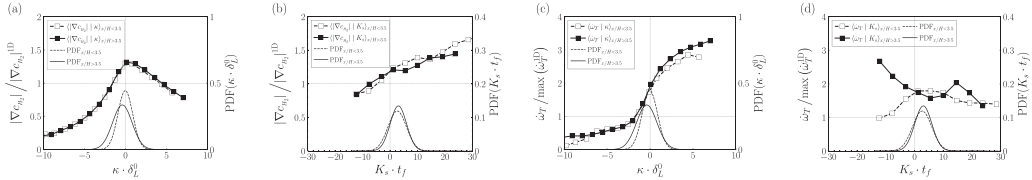


Fig. 16. H_2 flame: averages of $|\nabla c_{\text{H}_2\text{O}}|$ and ω_T conditioned by κ (a, c) and K_s (b, d) in first ($x/H \leq 3.5$) and second region ($x/H > 3.5$). Parameters are retrieved on the isosurface of $c_{\text{H}_2} = 0.85$, at $t = 2\tau$. Progress variable gradients are normalized with $|\nabla c_{\text{H}_2\text{O}}|^{\text{1D}}$ computed from the corresponding 1D unstretched laminar flame at $c_{\text{H}_2} = 0.85$.

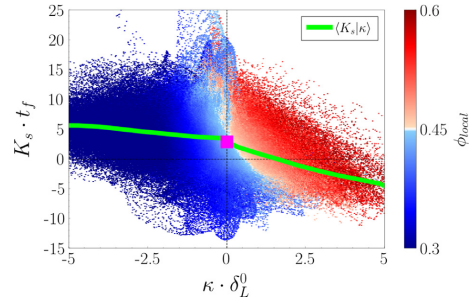


Fig. 17. Joint distribution of tangential strain rates K_s and curvature κ colored by local equivalence ratio ϕ_{local} , retrieved on the isosurface of $c_{\text{H}_2} = 0.85$, at $t = 2\tau$. The solid line represents the averages of K_s conditioned by κ . The square dot represents the mean strain rate and is located at $\kappa \approx 0$. (For interpretation of the references to color in this figure, the reader is referred to the web version of this article.)

front causing significant discrepancies in local equivalence ratios, which is further discussed in the following. In contrast with the laminar case, super-unity values of normalized HRR are already observed in the first region ($x/H \leq 3.5$), indicating that stretch effects impact the flame for very early axial positions with $I_0 > 1$ near the flame foot as shown in [25]. As a result, a strong overconsumption is observed on flat flame elements [76] and in the vicinity of the leading edges, which counterbalances the stiffening effects so that the overall response of the hydrogen flame to stretch yields large super-unity I_0 values as shown in Fig. 13c. Also, note the increase in HRR for positive values of K_s in Fig. 16d before switching to extinction due to blow off.

It is instructive to quantify both curvature and tangential strain rate effects on the H_2 flame structure by assessing the variations in local equivalence ratio. Fig. 17 shows the relationship between K_s and κ through a joint distribution colored by local equivalence ratio, ϕ_{local} , defined by Eq. (12) [31]

$$\phi_{\text{local}} = \frac{Z_{\text{H}}/Z_{\text{O}}}{(Z_{\text{H}}/Z_{\text{O}})_{\text{st}}} \quad (12)$$

Local equivalence ratios span a wide range of values, with very large hydrogen depletion close to the trailing edges mostly associated with positive strain rates causing local extinction events. While the global equivalence ratio is retrieved at $\kappa \approx 0$, the limit for leaner and richer mixtures is shifted toward positively curved and compressed flame elements. This highlights the influence of tangential strain rates on the hydrogen preferential diffusion effects for flame elements slightly curved with positive curvature, which correspond to the tails of thermo-diffusively unstable structures. However, flame elements strongly curved at the tip of these long-tail structures generate unconditionally local richer mixtures, hence explaining the large HRR associated with compressed and thickened flame elements as shown in Fig. 16d (2nd region). The averages of K_s conditioned by κ for each flame are shown in Fig. K.1 of the supplementary material.

Finally, the impact of stretch effects on the whole H_2 flame structure is investigated and compared to the CH_4 and $\text{NH}_3\text{-H}_2$ cases: Fig. 18 shows the conditional mean of $|\nabla c|$ with respect to the fuel progress variable c . For CH_4 , the gradients are almost not altered in the preheat zone but slightly steeper in the reaction zone due to straining effects as shown in Fig. 14b. While the $\text{NH}_3\text{-H}_2$ case features the same behavior as the CH_4 case, significant gradients are retrieved for the H_2 case, especially in the preheat zone and up to the oxidation zone.

Fig. 19 shows conditional means of heat release rates with respect to the progress variable for all cases. As expected, the CH_4 flame is not leading to higher HRR than the maximum flamelet rate consistently with previous works [13,14,33,77]. A nearly analogous result is observed in the preheat zone of the $\text{NH}_3\text{-H}_2$ case, but conditional averages yield lower HRR in the reaction zone since this flame burns less fresh reactants when strained (Fig. 15d). A large scatter is observed in this case but induces only a small deviation of the conditional averages with respect to the 1D flame, as shown in Fig. 19b, which reveals source term discrepancies without significant internal flame structure alterations. This result confirms the thermo-diffusively stable behavior of the $\text{NH}_3\text{-H}_2$ blend used in this work (46% vol. H_2) at stoichiometric conditions under atmospheric pressure and temperature. In contrast, Wiseman et al. [15] retrieved a thermo-diffusively unstable flame at atmospheric pressure, in lean ($\phi = 0.45$) and preheated ($T_u = 750\text{K}$) conditions by computing a temporally evolving turbulent planar

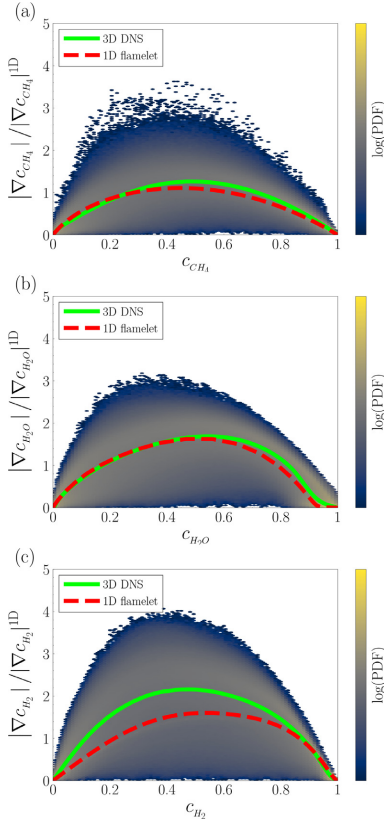


Fig. 18. Averages of $|\nabla c|$ conditioned by c , at $t = 2\tau$. Scatter: 3D points with corresponding PDF (in log scale), dashed-lines: 1D unstretched laminar flames, solid lines: conditional means of $|\nabla c|$ for CH_4 case (a), $\text{NH}_3\text{-H}_2$ case (b), H_2 case (c). (For interpretation of the references to color in this figure, the reader is referred to the web version of this article.)

jet flame with similar turbulence parameters ($u'/S_L^0 \approx 7$, $l_t/\delta_L^0 \approx 4.8$ and $Re = 13800$). It is equivalently characterized by a mismatch between the HRR conditioned by water-based progress variable and their corresponding 1D flame. The authors indicate a stronger consumption of the fuel with respect to the flame surface increase, leading to $l_0 \approx 2$ in this case, with a flame more resilient to strain in lean and preheated conditions because of the fast hydrogen diffusion (see also [30]). Further analysis of this case [32] indicated the strong influence of flame elements convexly curved toward reactants on burning rates, even exacerbated at higher pressure. Therefore, while the stoichiometric $\text{NH}_3\text{-H}_2$ flame structure of the present study is almost not altered by the turbulent mixing, drastic changes could be obtained with different fuel proportions and operating conditions.

However, when considering the pure H_2 flame, a large scatter is observed in Fig. 19c with a remarkable deviation with respect to the corresponding flamelet in the preheat zone as expected in TRZ regime. While this result indicates the poor ability of the progress variable c_{H_2} to represent all local flame states due to the turbulent mixing, the scalar value $c_{\text{H}_2}^* = 0.85$ retrieved in the 1D flame

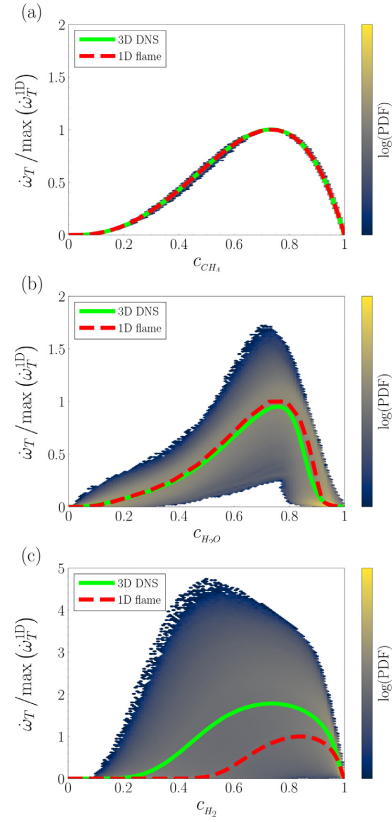


Fig. 19. Averages of ω_T conditioned by c , at $t = 2\tau$. Scatter: 3D points with corresponding PDF (in log scale), dashed-lines: 1D unstretched laminar flames, solid lines: conditional means of ω_T for CH_4 case (a), $\text{NH}_3\text{-H}_2$ case (b), H_2 case (c). (For interpretation of the references to color in this figure, the reader is referred to the web version of this article.)

almost matches the maximum value of the conditional mean. This could explain the good agreement between both stretch factors l_0^* and l_0 observed in the previous section. It also confirms that the flame structure highly modified by the gradients is even more altered by the intense local burning rates, leading to average flame propagation speeds in excess compared to S_L^0 .

3.4. Variations in hydrogen flame structure: Comparison with counterflow flamelets

As shown in the previous sections, hydrogen preferential diffusion strongly impacts the flame dynamics by impacting the flame surface and enhancing the local equivalence ratio. However, the flame structure variations observed in the DNS are also ascribed to tangential strain rates for near-flat flame elements. Therefore, both parameters should be considered to model the overconsumption of hydrogen in lean conditions. Hence, laminar premixed counterflow calculations were performed, for counterflow flamelets based on equilibrium products assumed to be fairly representative of the local environment of the 3D turbulent flame. The calculations span

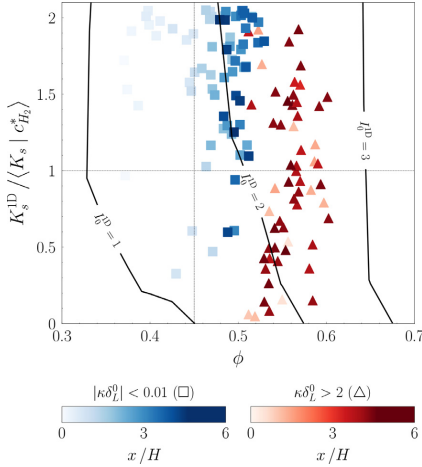


Fig. 20. Contours of 1D stretch factors $S_c^{1D} = S_c^{1D}/S_L^0$ ($\phi = 0.45$) in the $K_s^{1D} - \phi$ space, with strain rates and equivalence ratios matching the values retrieved on the isosurface of $c_{H_2}^*$. The mean strain rate value in the 3D DNS is $(K_s |c_{H_2}^*|) = 2436s^{-1}$. Flamelets are computed from Cantera counterflow calculations at $T_u = 300K$ and $P = 1bar$, and $K_s^{1D} = (\dot{m}_u/\rho_u + \dot{m}_b/\rho_b)/L$ with L the distance separating streams of fresh and burnt gases, \dot{m}_u and \dot{m}_b the mass fluxes per unit area of the unburnt and burnt gases, respectively. Points belonging to the 3D isosurface of $c_{H_2}^*$ are retrieved from near-flat flame elements ($|k\delta_L^0| < 0.01$), and positively curved flame elements ($k\delta_L^0 > 2$ and $\phi_{local}/\phi_{global} > 1.1$). Each point is colored as a function of the distance to the inlet x/H .

a range of equivalence ratios $0.3 < \phi < 0.7$, with 1D strain rate K_s^{1D} values from $0s^{-1}$ to twice the average value measured on the isosurface of $c_{H_2}^*$, from which $I_0 \approx I_0$ has been observed. Then, 1D stretched laminar consumption flame speeds S_c^{1D} are computed according to Eq. (13) and normalized by the 1D unstretched laminar flame speed S_L^0 at global equivalence ratio of the 3D case in the $K_s^{1D} - \phi$ space

$$S_c^{1D} = -\frac{1}{\rho_u Y_{f,u}} \int \dot{\omega}_{H_2} dx. \quad (13)$$

The ratios S_c^{1D}/S_L^0 corresponds to the 1D stretch factors retrieved from flamelets subjected to various mixtures and strain effects only. To compare with the data retrieved from the aforementioned isosurface, several points belonging to near-flat flame elements are sorted according to the condition $|k\delta_L^0| < 0.01$ from those matching large positive curvature values at $k\delta_L^0 > 2$. Fig. 20 shows that 3D data are located in the range $1 < S_c^{1D}/S_L^0 < 3$, thus matching the 3D stretch factors observed in the DNS (Fig. 13c). Most of the points extracted from flat flame elements correspond to slightly richer conditions than the global equivalence ratio since no flame elements are perfectly flat in turbulent conditions. In particular, 1D stretch factors $S_c^{1D}/S_L^0 \approx 2$ are retrieved all along the isosurface, except near the inlet, which highlights the strong influence of strain effects on the consumption rates in regions weakly affected by the hydrogen preferential diffusion. This suggests that the hydrogen flame response to large tangential strain rates in near-flat regions could lead to global stretch factors retrieved in turbulent conditions [64]. Moreover, flame elements strongly affected by the hydrogen preferential diffusion with equivalence ratios highly shifted to richer conditions exhibit higher consumption speed deviations with $2 < S_c^{1D}/S_L^0 < 3$ irrespective of the strain rate values. These points correspond to positively curved regions enriched by hydrogen preferential diffusion and piloted by the thermo-diffusive in-

stabilities in the 3D DNS. Note that as the equivalence ratio decreases, the strain rates have much less impact on the consumption rates with 1D stretch factors close to unity, indicating that highly strained cusp regions are much less affected than the leading edges.

These findings suggest that 1D counterflow flamelets in the $K_s^{1D} - \phi$ space can be used to reasonably approximate stretch effects in addition to the flame surface wrinkling determined by the flame surface density approach. Investigations about the overconsumption induced by the coupling between strain effects and preferential diffusion using 1D - 3D comparisons will be the subject of future work, considering a wider range of DNS operating conditions and including multi-fuel assessment with NH_3-H_2 flames.

4. Conclusion

In this study, three DNS calculations of methane, ammonia-hydrogen and pure hydrogen premixed flames were conducted at atmospheric conditions, in a slot burner configuration and in both laminar and turbulent regimes. The composition of each mixture is chosen to provide the same unstretched laminar flame speed of the stoichiometric methane flame, leading to a stoichiometric ammonia-hydrogen flame using 46% vol. H_2 and a lean hydrogen flame ($\phi_{global} = 0.45$). Although the gas expansion ratios differ, the results show that the three mixtures lead to very similar flames in the laminar regime because they propagate at the same speed, albeit small oscillations are observed for the pure hydrogen case due to the thermo-diffusive instabilities that are convected toward the flame tip. However, when turbulence is injected in the fresh gases, results change drastically: both methane and ammonia-hydrogen cases generate similar turbulent flames but the pure hydrogen flame brush is shorter with less flame surface.

The displacement speed plays an important role in the evolution of flame surfaces, causing the destruction of each flame on the negatively curved flame regions in the rear of each flame brush, by overwhelming the surface creation mainly driven by tangential strain rates. The flame destruction is amplified by strong surface contractions due to flame-flame interactions which locally disrupt the diffusive fluxes leading to strong positive values of displacement speed in the cusp regions. While this effect is supported by the reaction rates of the methane and ammonia-hydrogen flames, the pure hydrogen flame exhibits a kinematic restoration mainly from its diffusive fluxes. Moreover, the hydrogen case exhibits higher flame surface production at the leading edges because of thermo-diffusive instabilities, resulting in a nearly zero surface budget from dilatation by propagation.

Both methane and ammonia-hydrogen turbulent combustion are mostly driven by the flame wrinkling induced by turbulence without significant flame structure alterations, whereas the hydrogen flame is strongly impacted by stretch effects. The stoichiometric conditions of the ammonia-hydrogen blend lead to a thermo-diffusively stable flame, contrasting with previous studies using leaner mixtures. The pure hydrogen flame response to curvature and tangential strain rates is radically different with substantial flame structure alterations as indicated by super-unity stretch factor $I_0 > 1$. It originates from the hydrogen preferential diffusion effects leading to thermo-diffusive instabilities driven by the flame elements that are convexly curved to the reactants, but also from strain effects which highly affect the burning rates in regions of low curvature. In general, results show that the hydrogen flame response to stretch leads to an enhancement of the gradients, but the large burning rates counterbalance these stiffening effects causing average consumption speeds in excess of two times the unstretched laminar flame speed.

According to a 1D-3D comparison of the hydrogen case, the impact of strain and mixture variations are well recovered using

counterflow flamelet calculations, suggesting that such 1D flames could be used to approximate the stretch effects on lean hydrogen flames propagation in turbulent conditions.

Declaration of Competing Interest

The authors declare that they have no known competing financial interests or personal relationships that could have appeared to influence the work reported in this paper.

Acknowledgments

The research leading to these results has received funding from the European Union's Horizon 2020 – Research and Innovation Framework Programme H2020-INFRAEDI-2019-1 under grant agreement no. 951733. This project has also received funding from the European Research Council under the European Union's Horizon 2020 research and innovation program under grant agreement no. 832248 (SCIROCCO). This work was performed using HPC resources of GENCI-TGCC under grant agreement no. 2023-A0132B10157. The authors acknowledge the Norwegian Research Council and related partners in the Low Emission Centre for the support of J. Gaucherand.

Supplementary material

Supplementary material associated with this article can be found, in the online version, at doi:10.1016/j.combustflame.2023.112933.

References

- [1] C.M. White, R.R. Steeper, A.E. Lutz, The hydrogen-fueled internal combustion engine: a technical review, *Int. J. Hydrog. Energy* 31 (2006) 1292–1305.
- [2] S. Verhelst, T. Wallner, Hydrogen-fueled internal combustion engines, *Prog. Energy Combust. Sci.* 35 (2009) 490–527.
- [3] A. Valera-Medina, H. Xiao, M. Owen-Jones, W.I.F. David, P.J. Bowen, Ammonia for power, *Prog. Energy Combust. Sci.* 69 (2018) 63–102.
- [4] C. Lhuillier, P. Brequigny, N. Lamoureux, F. Contino, C. Mounaïm-Rousselle, Experimental investigation on laminar burning velocities of ammonia/hydrogen/air mixtures at elevated temperatures, *Fuel* 263 (2020) 116653.
- [5] H. Kobayashi, A. Hayakawa, K.D.K.A. Somaratne, E.C. Okafor, Science and technology of ammonia combustion, *Prog. Combust. Inst.* 37 (2019) 109–133.
- [6] J.H. Lee, S.I. Lee, O.C. Kwon, Effects of ammonia substitution on hydrogen/air flame propagation and emissions, *Int. J. Hydrog. Energy* 35 (2010) 11332–11341.
- [7] W.S. Chai, Y. Bao, P. Jin, G. Tang, L. Zhou, A review on ammonia, ammonia-hydrogen and ammonia-methane fuels, *Renew. Sustain. Energy Rev.* 147 (2021) 111254.
- [8] A.N. Lipatnikov, J. Chomiak, Molecular transport effects on turbulent flame propagation and structure, *Prog. Energy Combust. Sci.* 31 (2005) 1–73.
- [9] M. Fischer, Safety aspects of hydrogen combustion in hydrogen energy systems, *Int. J. Hydrog. Energy* 11 (1986) 593–601.
- [10] G. Darrieus, Propagation d'un front de flamme, *La Technique Moderne* 30 (1938) 18.
- [11] L.D. Landau, On the theory of slow combustion, *Acta Physicochimica URSS* 19 (1944) 77–85.
- [12] R. Sankaran, E.R. Hawkes, J.H. Chen, T. Lu, C.K. Law, Structure of a spatially developing turbulent lean methane-air bunsen flame, *Proc. Combust. Inst.* 31 (2007) 1291–1298.
- [13] R. Sankaran, E.R. Hawkes, C.S. Yoo, J.H. Chen, Response of flame thickness and propagation speed under intense turbulence in spatially developing lean premixed methane-air jet flames, *Combust. Flame* 162 (2015) 3294–3306.
- [14] S. Luca, A. Attili, E. Lo Schiavo, F. Creta, F. Bisetti, On the statistics of flame stretch in turbulent premixed jet flames in the thin reaction zone regime at varying Reynolds number, *Proc. Combust. Inst.* 37 (2019) 2451–2459.
- [15] S. Wiseman, M. Rieth, A. Gruber, J.R. Dawson, J.H. Chen, A comparison of the blow-out behavior of turbulent premixed ammonia/hydrogen/nitrogen-air and methane-air flames, *Proc. Combust. Inst.* 38 (2021) 2869–2876.
- [16] G. Damköhler, Der einfluss der turbulenz auf die flammengeschwindigkeit in gasgemischen, *Zeitschrift für Elektrochemie und angewandte physikalische Chemie* 46 (1940) 601–626.
- [17] J.H. Chen, H.G. Im, Stretch effects on the burning velocity of turbulent premixed hydrogen/air flames, *Proc. Combust. Inst.* 28 (2000) 211–218.
- [18] M. Day, J. Bell, P.T. Bremer, V. Pasucci, V. Beckner, M. Ljewiski, Turbulence effects on cellular burning structures in lean premixed hydrogen flames, *Combust. Flame* 156 (2009) 1035–1045.
- [19] A.J. Aspden, M.S. Day, J.B. Bell, Characterization of low lewis number flames, *Proc. Combust. Inst.* 33 (2011) 1463–1471.
- [20] A.J. Aspden, M.S. Day, J.B. Bell, Turbulence-flame interactions in lean premixed hydrogen: transition to the distributed burning regime, *J. Fluid Mech.* 680 (2011) 287–320.
- [21] B. Savard, G. Blanquart, An a priori model for the effective species lewis numbers in premixed turbulent flames, *Combust. Flame* 161 (2014) 1547–1557.
- [22] A.J. Aspden, M.S. Day, J.B. Bell, Turbulence-chemistry interaction in lean premixed hydrogen combustion, *Proc. Combust. Inst.* 35 (2015) 1321–1329.
- [23] C.E. Frouzakis, N. Fogle, A.G. Tomboulides, C. Altantzis, M. Matalon, Numerical study of unstable hydrogen/air flames: shape and propagation speed, *Proc. Combust. Inst.* 35 (2015) 1087–1095.
- [24] T.L. Howarth, A.J. Aspden, An empirical characteristic scaling model for freely-propagating lean premixed hydrogen flames, *Combust. Flame* 237 (2022) 111805.
- [25] L. Berger, A. Attili, H. Pitsch, Synergistic interactions of thermodiffusive instabilities and turbulence in lean hydrogen flames, *Combust. Flame* 244 (2022) 112254.
- [26] L. Berger, A. Attili, H. Pitsch, Intrinsic instabilities in premixed hydrogen flames: parametric variation of pressure, equivalence ratio, and temperature. Part 1 – dispersion relations in the linear regime, *Combust. Flame* (2022) 111935.
- [27] L. Berger, A. Attili, H. Pitsch, Intrinsic instabilities in premixed hydrogen flames: parametric variation of pressure, equivalence ratio, and temperature. Part 2 – non-linear regime and flame speed enhancement, *Combust. Flame* (2022) 111936.
- [28] M. Matalon, C. Cui, J.K. Bechtold, Hydrodynamic theory of premixed flames: effects of stoichiometry, variable transport coefficients and arbitrary reaction orders, *J. Fluid Mech.* 487 (2003) 179–210.
- [29] G.I. Sivashinsky, Instabilities, pattern formation, and turbulence in flames, *Annu. Rev. Fluid Mech.* 15 (1983) 179–199.
- [30] M. Rieth, A. Gruber, J.H. Chen, The effect of pressure on lean premixed hydrogen-air flames, *Combust. Flame* (2023) 112514.
- [31] C. Netzer, A. Ahmed, A. Gruber, T. Lavás, Curvature effects on NO formation in wrinkled laminar ammonia/hydrogen/nitrogen-air premixed flames, *Combust. Flame* 232 (2021) 111520.
- [32] M. Rieth, A. Gruber, F.A. Williams, J.H. Chen, Enhanced burning rates in hydrogen-enriched turbulent premixed flames by diffusion of molecular and atomic hydrogen, *Combust. Flame* 239 (2021) 111740.
- [33] A. Attili, S. Luca, D. Denker, F. Bisetti, H. Pitsch, Turbulent flame speed and reaction layer thickening in premixed jet flames at constant Karlovitz and increasing Reynolds numbers, *Proc. Combust. Inst.* 38 (2021) 2939–2947.
- [34] P. Quillatre, O. Vermorel, T. Poinso, P. Ricoux, Large eddy simulation of vented deflagration, *Ind. Eng. Chem. Res.* 52 (2013) 11414–11423.
- [35] M. Pfitzner, P. Breda, An analytic probability density function for partially premixed flames with detailed chemistry, *Phys. Fluids* 33 (2021) 035117.
- [36] M. Pfitzner, A new analytic PDF for simulations of premixed turbulent combustion, *Flow Turbul. Combust.* 106 (2021) 1213–1239.
- [37] M. Pfitzner, M. Klein, A near-exact analytic solution of progress variable and PDF for single-step arrhenius chemistry, *Combust. Flame* 226 (2021) 390–395.
- [38] P. Saxena, F.A. Williams, Testing a small detailed chemical-kinetic mechanism for the combustion of hydrogen and carbon monoxide, *Combust. Flame* 145 (2006) 316–323.
- [39] A. Stagni, C. Cavallotti, S. Arunthanayothin, Y. Song, O. Herbinet, F. Battin-Leclerc, T. Faravelli, An experimental, theoretical and kinetic-modeling study of the gas-phase oxidation of ammonia, *React. Chem. Eng.* 5 (2020) 696–711.
- [40] Q. Cazères, P. Peipiot, E. Ribet, B. Cuenot, A fully automatic procedure for the analytical reduction of chemical kinetics mechanisms for computational fluid dynamics applications, *Fuel* 303 (2021) 121247.
- [41] T. Schönfeld, M. Rudgyard, Steady and unsteady flow simulations using the hybrid flow solver AVBP, *AIAA J.* (1999) 1378–1385.
- [42] O. Colin, M. Rudgyard, Development of high-order Taylor-Galerkin schemes for LES, *J. Comput. Phys.* (2000) 338–371.
- [43] D.G. Goodwin, H.K. Moffat, I. Schoegl, R.L. Speth, B.W. Weber, Cantera: an object-oriented software toolkit for chemical kinetics, thermodynamics, and transport processes, 2022, Version 2.6.0.
- [44] R.H. Kraichnan, Diffusion by a random velocity field, *Phys. Fluids* 13 (1970) 22–31.
- [45] T. Passot, A. Pouquet, Numerical simulation of compressible homogeneous flows in the turbulent regime, *J. Fluid Mech.* 181 (1987) 441–466.
- [46] S.B. Pope, *Turbulent flows*, Cambridge University Press, 2000.
- [47] S.P.R. Muppala, M. Nakahara, N.K. Aluri, H. Kido, J.X. Wen, M.V. Papalexandris, Experimental and analytical investigation of the turbulent burning velocity of two-component fuel mixtures of hydrogen, methane and propane, *Int. J. Hydrog. Energy* 34 (2009) 9258–9265.
- [48] T.J. Poinso, S.K. Lele, Boundary conditions for direct simulations of compressible viscous flows, *J. Comput. Phys.* 101 (1992) 104–129.
- [49] R. Borghi, On the structure and morphology of turbulent premixed flames, *Recent Adv. Aerosp. Sci.* (1985) 117–138.
- [50] N. Peters, *Turbulent combustion*, Cambridge University Press, 2000.
- [51] D. Veynante, L. Vervisch, Turbulent combustion modeling, *Prog. Energy Combust. Sci.* 28 (2002) 193–266.
- [52] T. Poinso, D. Veynante, Theoretical and numerical combustion, RT Edwards, Inc., 2005.

- [53] A.W. Skiba, T.M. Wabel, C.D. Carter, S.D. Hammack, J.E. Temme, J.F. Driscoll, Premixed flames subjected to extreme levels of turbulence Part I: flame structure and a new measured regime diagram, *Combust. Flame* 189 (2018) 407–432.
- [54] S.B. Pope, The evolution of surfaces in turbulence, *Int. J. Eng. Sci.* 26 (1988) 445–469.
- [55] A. Trounev, The evolution equation for the flame surface density in turbulent premixed combustion, *J. Fluid Mech.* 278 (1994) 1–31.
- [56] F. Charlette, C. Meneveau, D. Veynante, A power-law flame wrinkling model for LES of premixed turbulent combustion Part I: non-dynamic formulation and initial tests, *Combust. Flame* 131 (2002) 159–180.
- [57] L. Vervisch, E. Bidaux, K.N.C. Bray, W. Kollmann, Surface density function in premixed turbulent combustion modeling, similarities between probability density function and flame surface approaches, *Phys. Fluids* 7 (1995) 2496–2503.
- [58] K.N.C. Bray, R.S. Cant, Some applications of Kolmogorov's turbulence research in the field of combustion, *Proc. R. Soc. London. Ser. A Math. Phys. Sci.* 434 (1991) 217–240.
- [59] D. Bradley, P.H. Gaskell, X.J. Gu, The modeling of aerodynamic strain rate and flame curvature effects in premixed turbulent combustion, *Symp. (Int.) Combust.* 27 (1998) 849–856.
- [60] A.J. Aspden, M.S. Day, J.B. Bell, Three-dimensional direct numerical simulation of turbulent lean premixed methane combustion with detailed kinetics, *Combust. Flame* 166 (2016) 266–283.
- [61] T. Echekki, J.H. Chen, Analysis of the contribution of curvature to premixed flame propagation, *Combust. Flame* (1999) 492–497.
- [62] H.A. Urañakara, S. Chaudhuri, H.L. Dave, P.G. Arias, H.G. Im, A flame particle tracking analysis of turbulence-chemistry interaction in hydrogen-air premixed flames, *Combust. Flame* (2016) 220–240.
- [63] T. Falkenstein, A. Rezhikova, R. Langer, M. Bode, S. Kang, H. Pitsch, The role of differential diffusion during early flame kernel development under engine conditions - Part I: analysis of the heat-release-rate response, *Combust. Flame* 221 (2020) 502–515.
- [64] Z. Lu, Y. Yang, Modeling pressure effects on the turbulent burning velocity for lean hydrogen/air premixed combustion, *Proc. Combust. Inst.* (2021) 2901–2908.
- [65] E. Suillaud, K. Truffin, O. Colin, D. Veynante, Direct numerical simulations of high Karlovitz number premixed flames for the analysis and modeling of the displacement speed, *Combust. Flame* 236 (2022) 111770.
- [66] N. Chakraborty, D. Alwazzan, M. Klein, R.S. Cant, On the validity of Damköhler's first hypothesis in turbulent bunsen burner flames: a computational analysis, *Proc. Combust. Inst.* 37 (2019) 2231–2239.
- [67] I. Han, K.Y. Huh, Roles of displacement speed on evolution of flame surface density for different turbulent intensities and lewis numbers in turbulent premixed combustion, *Combust. Flame* 152 (2008) 194–205.
- [68] N. Peters, The turbulent burning velocity for large-scale and small-scale turbulence, *J. Fluid Mech.* 384 (1999) 107–132.
- [69] H.L. Dave, S. Chaudhuri, Evolution of local flame displacement speeds in turbulence, *J. Fluid Mech.* 884 (2019) A46.
- [70] W. Song, H. Dave, H.G. Im, S. Chaudhuri, et al., Local flame displacement speeds of hydrogen-air premixed flames in moderate to intense turbulence, *Combust. Flame* 236 (2022) 111812.
- [71] C.K. Law, S. Ishizuka, P. Cho, On the opening of premixed bunsen flame tips, *Combust. Sci. Technol.* 28 (1982) 89–96.
- [72] Y. Mizobuchi, T. Nambu, T. Takeno, Numerical study of tip opening of hydrogen/air bunsen flame, *Proc. Combust. Inst.* 37 (2019) 1775–1781.
- [73] W. Song, F.E. Hernández Pérez, E.A. Tingas, H.G. Im, Statistics of local and global flame speed and structure for highly turbulent H₂/air premixed flames, *Combust. Flame* 232 (2021) 111523.
- [74] W. Song, F.E. Hernández-Pérez, H.G. Im, Diffusive effects of hydrogen on pressurized lean turbulent hydrogen-air premixed flames, *Combust. Flame* 246 (2022) 112423.
- [75] P. Tamadonfar, O.L. Gülder, Experimental investigation of the inner structure of premixed turbulent methane/air flames in the thin reaction zones regime, *Combust. Flame* 162 (2015) 115–128.
- [76] M. Baum, T.J. Poinso, D.C. Haworth, N. Darabiha, Direct numerical simulation of H₂/O₂/N₂ flames with complex chemistry in two-dimensional turbulent flows, *J. Fluid Mech.* 281 (1994) 1–32.
- [77] C. Jiménez, B. Cuenot, T. Poinso, D. Haworth, Numerical simulation and modeling for lean stratified propane-air flames, *Combust. Flame* 128 (2002) 1–21.

Direct Numerical Simulation of methane,
ammonia-hydrogen and hydrogen turbulent premixed flames
– Supplementary material n°1

Victor Coulon^{a,*}, Jessica Gaucherand^{a,b}, Victor Xing^a, Davide Laera^{a,c}, Corentin Lapeyre^a, Thierry Poinso^{a,d}

^a*CERFACS, 42 avenue Gaspard Coriolis, 31057 Toulouse, France*

^b*Department of Energy and Process Engineering, Norwegian University of Science and Technology, NO-7034 Trondheim, Norway*

^c*Department of Mechanics, Mathematics and Management, Polytechnic University of Bari, Via Orabona 4, 70125 Bari, Italy*

^d*IMFT, Allée du Professeur Camille Soula, 31400 Toulouse, France*

This supplementary material provides the following additional contents:

- (A) Reference parameters of the power law model for viscosity,
- (B) Validation of ammonia-hydrogen reduced scheme (ARC),
- (C) Mesh convergence study,
- (D) Spectral analysis of the turbulence,
- (E) 2D laminar calculations,
- (F) Definition of stretch,
- (G) 3D isosurfaces colored by the normal and tangential components of the diffusive contribution of the displacement speed,
- (H) Average of the displacement speed conditioned by curvature,
- (I) 3D isosurfaces colored by the density-weighted displacement speed,
- (J) Transverse slices of heat release rate,
- (K) Average of the tangential strain rate conditioned by curvature.

*Corresponding author:
Email address: coulon@cerfacs.fr (Victor Coulon)

A. Reference parameters of the power law model for viscosity

The solver¹ used in this study allows to compute multi-species flows assuming a molecular viscosity μ independent of the gas composition. This assumption is considered since mixtures are perfectly premixed and mainly composed of air which is characterized by a Prandtl number around 0.7. Molecular viscosity is determined using the power law as

$$\mu = \mu_{ref} \left(\frac{T}{T_{ref}} \right)^b \quad (\text{A.1})$$

where the reference parameters μ_{ref} , T_{ref} and b (Table A.1) are determined using least squares optimization to fit viscosity values computed with Wilke's law [1] from 1D flame calculations for ranges of pressure, unburned gas temperature and pressure.

Case	CH ₄	NH ₃ -H ₂	H ₂
μ_{ref} [kg m ⁻¹ s ⁻¹]	1.80×10^{-5}	1.76×10^{-5}	8.06×10^{-5}
T_{ref} [K]	300	303	265
b	0.68	0.67	0.65

Table A.1: Reference parameters used to model the molecular viscosity with the power law for all cases.

¹<http://www.cerfacs.fr/avbp7x>

B. Validation of ammonia-hydrogen reduced scheme (ARC)

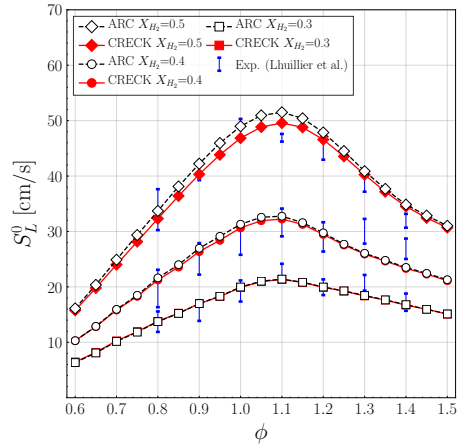


Figure B.1: Reduced scheme validation for the $\text{NH}_3\text{-H}_2$ blend. Numerical data from CRECK (detailed) [2], and ARC (reduced) schemes are in good agreement with experimental data from Lhuillier et al. [3].

C. Mesh convergence study

Mesh resolution has been chosen based on a mesh convergence study considering pure H_2 . Fig. C.1 shows hydrogen reaction rates conditionally averaged with respect to the progress variable (based of the fuel mass fraction) using four different mesh resolutions: $N_c = [4.5, 7, 9, 11]$, with N_c the number of mesh points within the thermal thickness δ_L^0 . According to this study, a convergence clearly starts above $N_c = 9$. Hence, 11 mesh points seems accurate enough to capture 3D Lewis effects on $\text{NH}_3\text{-H}_2$ and H_2 flames structure, and very close to the adequate resolution for thermo-diffusively instable flames mentioned by Howarth *et al.* [4]. The $N_c = 7$ case gives acceptable results, and was chosen for the CH_4 case for which the Lewis effects are known to be not critical.

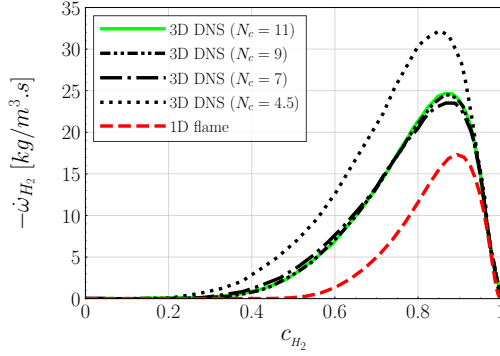


Figure C.1: Conditional averages of hydrogen reaction rates with respect to the progress variable (H_2 based) for different mesh resolutions.

D. Spectral analysis of the turbulence

In these configurations, two sources of velocity fluctuations affect the flames:

1. The homogeneous and isotropic turbulence injected in the fresh gases of the slotburner using the Passot-Pouquet spectrum. To quantify its evolution, power spectral densities of different temporal signals of the turbulent kinetic energy have been computed. Results indicate that turbulence decays very slowly as shown in [Fig. D.1](#), where nearly self-similar spectra are observed for signals retrieved along the streamwise direction, in the center of the flame brush at fixed positions in both crosswise and spanwise directions.
2. The turbulence generated in the shear zones. The development of the shear-induced turbulence in the two shear layers is strongly affected by each flame development, which adds significant dissipation to the turbulent structures ([Fig. D.2](#)). It is not clear that this turbulence will ever have enough time to become fully developed according to the statistics retrieved in the jet core.

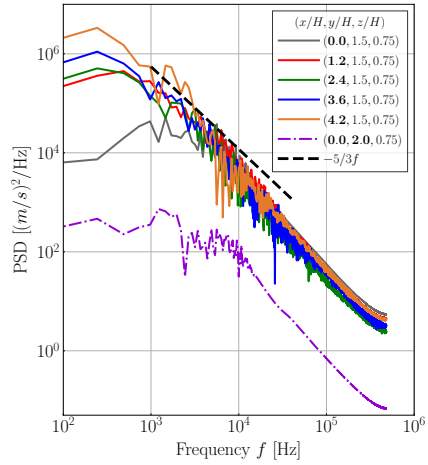


Figure D.1: Power spectral density of temporal signals of turbulent kinetic energy (TKE) retrieved at six positions "P" for the H_2 case. Lower power density is observed for the entire bandwidth of the TKE signal located in the upper shear layer (position "P1bis"), where high viscous dissipation rates are retrieved.

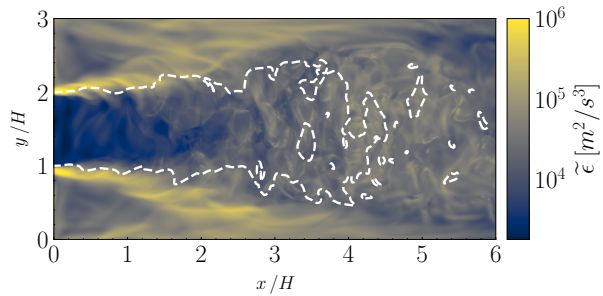


Figure D.2: H_2 case: viscous dissipation rate and contour of progress variable $c_{H_2}^* = 0.85$, both averaged in the spanwise direction z .

E. 2D laminar calculations

Theoretically, the flame length of a 2D slot burner is defined as [5]

$$l_f = \frac{H/2}{\tan\left[\arcsin\left(\frac{S_L^0}{U_{bulk}}\right)\right]}, \quad (\text{E.1})$$

leading to $l_f \approx 0.28$ m, with H the slot height, S_L^0 the unstretched laminar flame speed and U_{bulk} the central jet velocity. Fig. E.1 shows the heat release rates of the flames normalized by their maximum value in a 1D unstretched laminar flame. In the absence of turbulent motions, all three flames behave in very similar ways, as expected from their identical laminar flame speed. The methane flame has constant heat release rates equal to the maximum flamelet value along the whole flame front. The same result is obtained over most of the ammonia-hydrogen flame, but a local flame extinction is observed at the flame tip (Fig. E.1, center). The hydrogen flame (Fig. E.1, right) has approximately the same length but exhibits thermo-diffusive instabilities near the flame tip. In this regime, they are convected by the mean flow and have only a small impact on the local flame states.

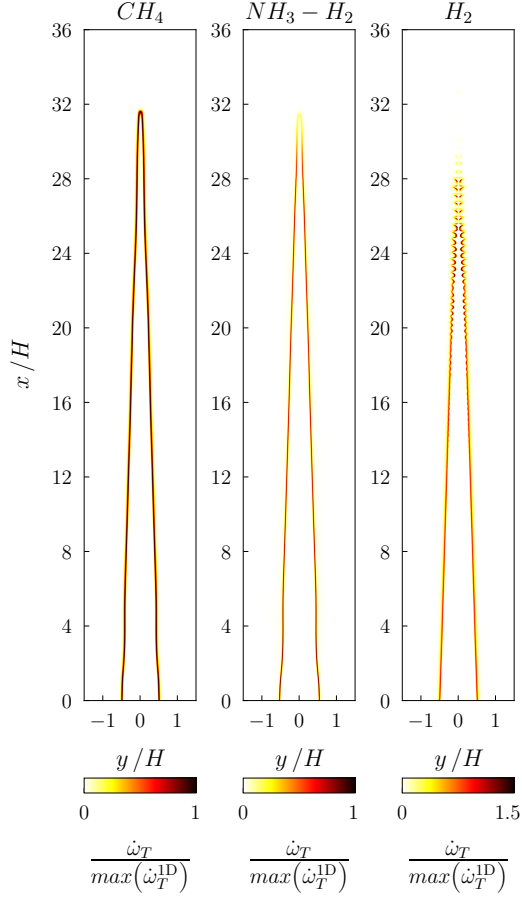


Figure E.1: Isocontours of normalized HRR for 2D laminar cases at $t \approx 100t_f$ ($t_f = \delta_L^0 / S_L^0$).

F. Definition of stretch

The total stretch K is driven by two contributions: the tangential strain rate, K_s , and the curvature-linked propagation rate (referred to as ‘‘curvature term’’), K_c . The overall stretch K experienced by the flame sheet is the sum of these two contributions

$$K = K_s + K_c = \nabla \mathbf{u} - \mathbf{nn} : \nabla \mathbf{u} + S_d \kappa, \quad (\text{F.1})$$

with $\kappa = \nabla \cdot \mathbf{n}$ representing the curvature and $\mathbf{n} = -\nabla c / |\nabla c|$ the normal vector to the flame front pointing towards the fresh gases. Therefore, positively curved flame elements are curved convexly to fresh gases while negatively curved flame elements are curved concavely to fresh gases. The curvature term represents surface dilatation and induces either surface production or destruction depending on the sign of S_d and κ . The displacement speed S_d represents the difference between the normal component of the flow field velocity vector \mathbf{u} , and the velocity vector associated to a point on the isosurface of c^* , \mathbf{w} , which follows the governing equation of the progress variable c Eq. (F.2) [5, 6]

$$\frac{\partial c}{\partial t} \Big|_{c=c^*} + \mathbf{w} \cdot \nabla c \Big|_{c=c^*} = 0. \quad (\text{F.2})$$

Hence, it is the flame front speed relative to the flow and is defined kinematically by Eq. (F.3)

$$S_d = (\mathbf{w} - \mathbf{u}|_{c=c^*}) \cdot \mathbf{n}. \quad (\text{F.3})$$

S_d can also be determined with the heat and species diffusive fluxes and the heat release rates on the isosurface of c^* by Eq. (F.4) [5]

$$S_d = \underbrace{\frac{1}{\rho C_p |\nabla T|} \left[\nabla \cdot (\lambda \nabla T) + \rho \nabla T \cdot \sum_k (\mathcal{D}_k C_{p,k} \nabla Y_k) \right]}_{S_{diff}} + \underbrace{\frac{1}{\rho C_p |\nabla T|} \left(- \sum_k h_k \dot{\omega}_k \right)}_{S_{reac}}, \quad (\text{F.4})$$

where \mathcal{D}_k is the molecular diffusion coefficient, $C_{p,k}$ is the mass-specific heat capacity, Y_k is the mass fraction, h_k is the enthalpy and $\dot{\omega}_k$ is the mass-production rate for the k th species. Therefore, the displacement speed is a net balance between the reaction rates and diffusive fluxes. The latter can be decomposed into a normal component which is generally oriented in the opposite direction to the normal vector \mathbf{n} as defined

above, and a tangential component which varies linearly with opposite curvature [7, 8]. In a steady, unstretched planar laminar flame, the sum of the contribution due to reaction and normal diffusion would be equal to S_L^0 [9]. Therefore, K_s is piloted only by turbulence whereas K_c depends on both turbulence and chemistry. In this work, S_d is computed from Eq. (F.4).

G. 3D isosurfaces colored by the normal and tangential components of the diffusive contribution of the displacement speed

G.1. Methane/air flame

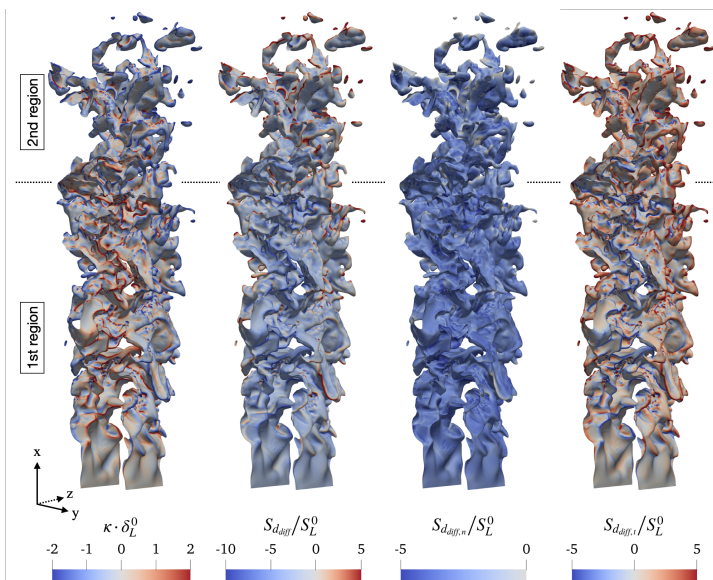


Figure G.1: Instantaneous isosurfaces of $c_{CH_4}^* = 0.72$, at $t = 2\tau$, colored by curvature κ , diffusive contribution of the displacement speed S_{diff} alongside its normal and tangential components $S_{diff,n}$, $S_{diff,t}$, respectively. Flame-flame interactions occur in regions highly curved with negative curvature where the normal diffusion fluxes oriented in the direction of normal vector \mathbf{n} are reduced, while tangential diffusion fluxes are increased. (For interpretation of the references to color in this figure, the reader is referred to the web version of this article.)

G.2. Ammonia-hydrogen/air flame

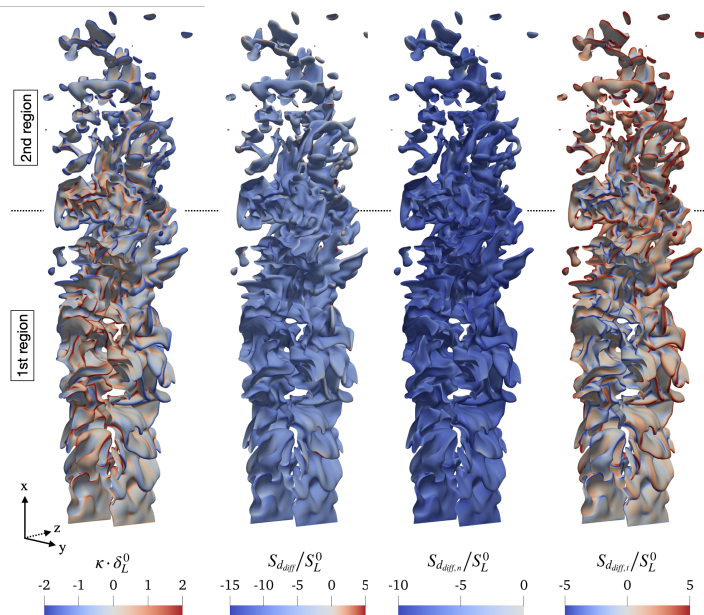


Figure G.2: Instantaneous isosurfaces of $c_{H_2O}^* = 0.8$, at $t = 2\tau$, colored by curvature κ , diffusive contribution of the displacement speed $S_{d_{diff}}$ alongside its normal and tangential components $S_{d_{diff,n}}$, $S_{d_{diff,t}}$, respectively. The flame-flame interactions in the extreme cusp regions are limited as the normal diffusion fluxes are not disrupted and annihilate the effects of tangential diffusion. (For interpretation of the references to color in this figure, the reader is referred to the web version of this article.)

G.3. Hydrogen/air flame

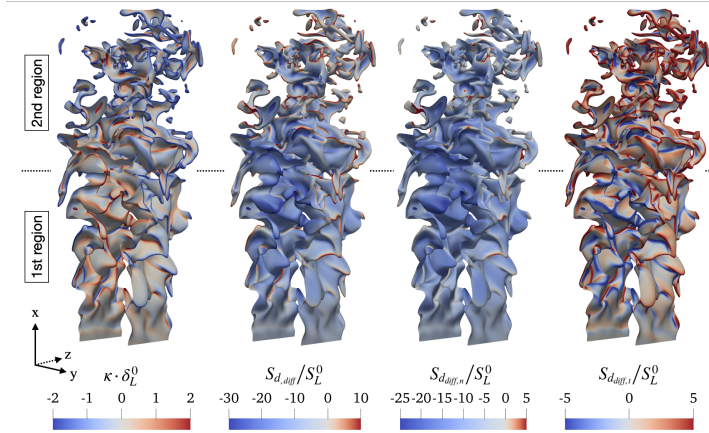


Figure G.3: Instantaneous isosurfaces of $c_{H_2}^* = 0.85$, at $t = 2\tau$, colored by curvature κ , diffusive contribution of the displacement speed $S_{d_{diff}}$ alongside its normal and tangential components $S_{d_{diff,n}}$, $S_{d_{diff,t}}$, respectively. Strong flame-flame interactions are retrieved, where the normal diffusion fluxes are strongly affected in the extreme cusp regions and supported by intense tangential diffusion fluxes. (For interpretation of the references to color in this figure, the reader is referred to the web version of this article.)

H. Average of the displacement speed conditioned by curvature

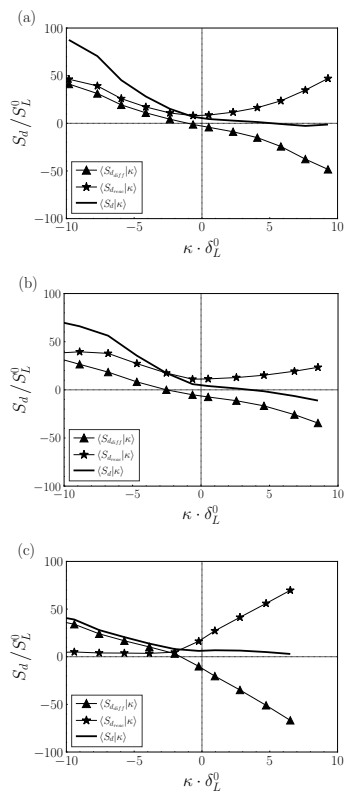


Figure H.1: Averages of the total displacement speed S_d and its diffusive and reactive contributions S_{diff} , S_{react} conditioned by curvature κ on the isosurfaces of c^* at $t = 2\tau$: CH₄ case (a), NH₃-H₂ case (b), H₂ case (c). Surface contraction at negative curvature is supported by the reactive contribution of S_d for both CH₄ and NH₃-H₂ cases, while the H₂ case exhibits a kinematic restoration induced by the diffusive fluxes only.

I. 3D isosurfaces colored by the density-weighted displacement speed

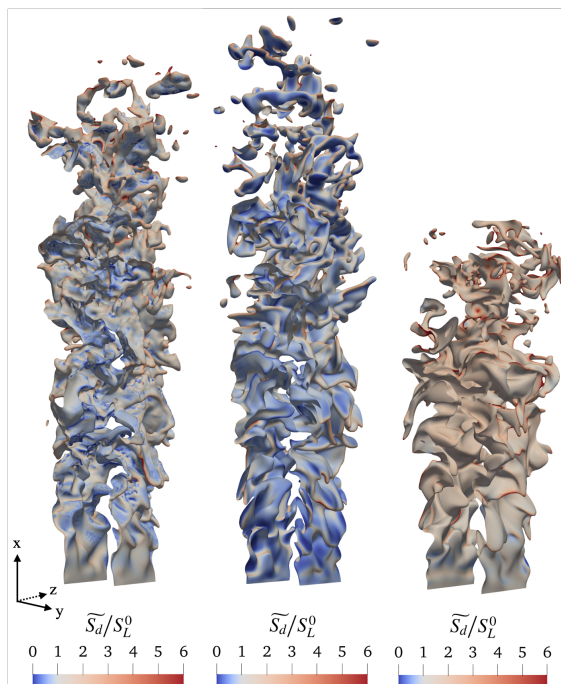


Figure I.1: Instantaneous isosurfaces of c^* , at $t = 2\tau$, colored by the density-weighted displacement speed: CH₄ case (left), NH₃-H₂ case (center), H₂ case (right). Averaging these fields yields the isoscalar-based stretch factors $I_0^* = \langle \widetilde{S}_d \rangle_S / S_L^0$ [10–13]. Extreme stretch factors are retrieved in the cusp regions and originate from flame-flame interactions as discussed in [14] (For interpretation of the references to color in this figure, the reader is referred to the web version of this article.)

J. Transverse slices of heat release rate

J.1. Methane/air flame

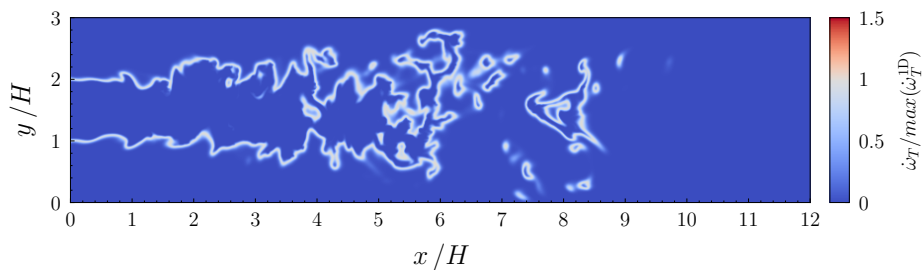


Figure J.1: Transverse slice of the CH_4 heat release rates normalized by the maximum value in corresponding 1D flame, retrieved at $t = 2\tau$. (For interpretation of the references to color in this figure, the reader is referred to the web version of this article.)

J.2. Ammonia-hydrogen/air flame

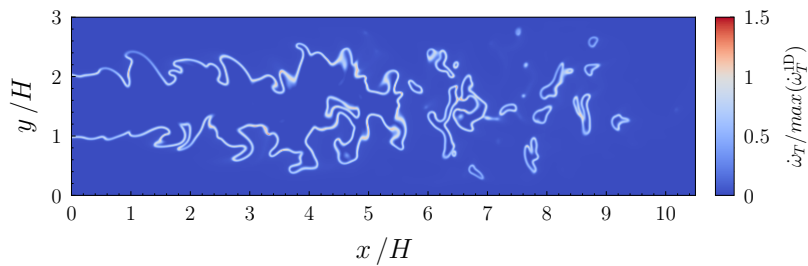


Figure J.2: Transverse slice of the $\text{NH}_3\text{-H}_2$ heat release rates normalized by the maximum value in corresponding 1D flame, retrieved at $t = 2\tau$. (For interpretation of the references to color in this figure, the reader is referred to the web version of this article.)

J.3. Hydrogen/air flame

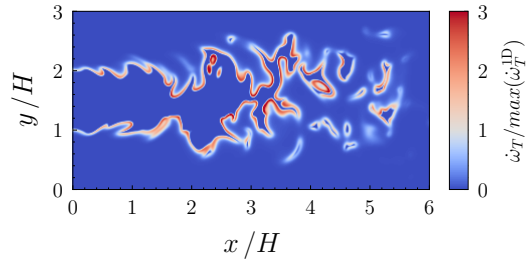


Figure J.3: Transverse slice of the H₂ heat release rates normalized by the maximum value in corresponding 1D flame, retrieved at $t = 2\tau$. Intense burning rates are retrieved on flame elements curved convexly to fresh gases (leading edges), as a marker of hydrogen preferential diffusion. (For interpretation of the references to color in this figure, the reader is referred to the web version of this article.)

K. Average of the tangential strain rate conditioned by curvature

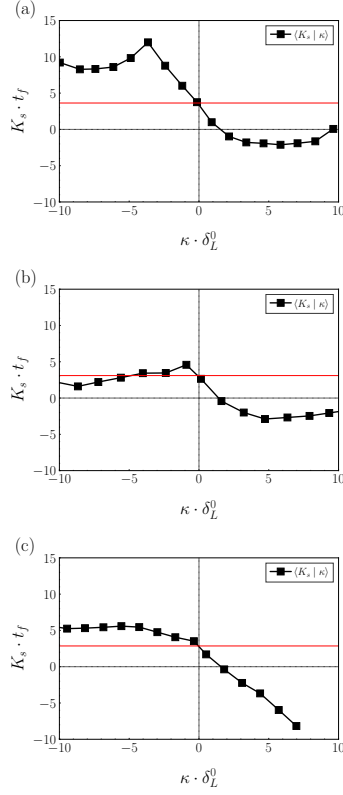


Figure K.1: Averages of the tangential strain rate K_s conditioned by curvature κ on the isosurfaces of c^* at $t = 2\tau$: CH₄ case (a), NH₃-H₂ case (b), H₂ case (c). The solid horizontal lines correspond to the mean strain rates for each case ($\langle K_s | c_{CH_4}^* \rangle = 3096 \text{ s}^{-1}$, $\langle K_s | c_{H_2O}^* \rangle = 2637 \text{ s}^{-1}$, $\langle K_s | c_{H_2}^* \rangle = 2436 \text{ s}^{-1}$). While both CH₄ and NH₃-H₂ cases reach an almost constant surface contraction ($K_s < 0$) at positive curvature, the H₂ case exhibits a stronger contraction which intensifies as the positive curvature increases. This effect is a marker of the thermo-diffusive instability of hydrogen.

References

- [1] C. R. Wilke, A viscosity equation for gas mixtures, *J. Chem. Phys.* (1950) 517–519.
- [2] A. Stagni, C. Cavallotti, S. Arunthanayothin, Y. Song, O. Herbinet, F. Battin-Leclerc, T. Faravelli, An experimental, theoretical and kinetic-modeling study of the gas-phase oxidation of ammonia, *React. Chem. Eng.* 5 (2020) 696–711.
- [3] C. Lhuillier, P. Brequigny, N. Lamoureux, F. Contino, C. Mounaïm-Rousselle, Experimental investigation on laminar burning velocities of ammonia/hydrogen/air mixtures at elevated temperatures, *Fuel* 263 (2020) 116653.
- [4] T. L. Howarth, A. J. Aspden, An empirical characteristic scaling model for freely-propagating lean premixed hydrogen flames, *Combust. Flame* 237 (2022) 111805.
- [5] T. Poinsot, D. Veynante, *Theoretical and numerical combustion*, RT Edwards, Inc., 2005.
- [6] S. B. Pope, The evolution of surfaces in turbulence, *Int. J. Eng. Sci.* 26 (1988) 445–469.
- [7] I. R. Gran, T. Echehki, J. H. Chen, Negative flame speed in an unsteady 2D premixed flame: A computational study, *Symp. Combust.* 26 (1996) 323–329.
- [8] T. Echehki, J. H. Chen, Analysis of the contribution of curvature to premixed flame propagation, *Combust. Flame* 144 (1999) 492–497.
- [9] N. Peters, P. Terhoeven, J. H. Chen, T. Echehki, Statistics of flame displacement speeds from computations of 2D unsteady methane-air flames, *Symp. Combust.* 27 (1998) 833–839.
- [10] H. A. Uranakara, S. Chaudhuri, H. L. Dave, P. G. Arias, H. G. Im, A flame particle tracking analysis of turbulence-chemistry interaction in hydrogen-air premixed flames, *Combust. Flame* (2016) 220–240.

- [11] T. Falkenstein, A. Rezchikova, R. Langer, M. Bode, S. Kang, H. Pitsch, The role of differential diffusion during early flame kernel development under engine conditions - Part I: Analysis of the heat-release-rate response, *Combust. Flame* 221 (2020) 502–515.
- [12] Z. Lu, Y. Yang, Modeling pressure effects on the turbulent burning velocity for lean hydrogen/air premixed combustion, *Proc. Combust. Inst.* (2021) 2901–2908.
- [13] E. Suillaud, K. Truffin, O. Colin, D. Veynante, Direct numerical simulations of high karlovitz number premixed flames for the analysis and modeling of the displacement speed, *Combust. Flame* 236 (2022) 111770.
- [14] W. Song, H. Dave, H. G. Im, S. Chaudhuri, et al., Local flame displacement speeds of hydrogen-air premixed flames in moderate to intense turbulence, *Combust. Flame* 236 (2022) 111812.

Direct Numerical Simulation of methane,
ammonia-hydrogen and hydrogen turbulent premixed flames
– Supplementary material n°2

Victor Coulon^{a,*}, Jessica Gaucherand^{a,b}, Victor Xing^a, Davide Laera^{a,c}, Corentin Lapeyre^a, Thierry Poinso^{a,d}

^a*CERFACS, 42 avenue Gaspard Coriolis, 31057 Toulouse, France*

^b*Department of Energy and Process Engineering, Norwegian University of Science and Technology, NO-7034 Trondheim, Norway*

^c*Department of Mechanics, Mathematics and Management, Polytechnic University of Bari, Via Orabona 4, 70125 Bari, Italy*

^d*IMFT, Allée du Professeur Camille Soula, 31400 Toulouse, France*

This supplementary material provides the following additional content:

(A) Reduced mechanism for $\text{NH}_3\text{-H}_2$ /air mixture.

*Corresponding author:

Email address: coulon@cerfacs.fr (Victor Coulon)

A. Reduced mechanism for ammonia-hydrogen/air mixture

The Analytically Reduced Chemistry (ARC) used in this work was derived to achieve an accurate description of the combustion of premixed $\text{NH}_3\text{-H}_2$ /air flames. The reduction was performed using Arcane [1], a fully automatic multi-step reduction tool relying on Directed Relation Graph with Error Propagation (DRGEP) [2], chemical lumping [3] and Quasi-Steady State (QSS) assumption [4].

The reference detailed mechanism is CRECK C1–C3 scheme (31 species, 203 reactions) [5], for which carbon related species are removed. The ARC mechanism models the chemistry of the ammonia-hydrogen/air blend with 14 transported species and 7 QSS species (Table A.1). The Prandtl number of all species is equal to 7.20223360e-01.

Transported		
Species	Schmidt number	QSS species
N_2	7.91933071e-01	O
H_2	2.01035469e-01	N_2H_2
H	1.29142304e-01	N_2H_4
O_2	7.80325784e-01	N
H_2O	7.11763704e-01	N_2H
OH	4.90096612e-01	N_2NO
H_2O_2	7.60364501e-01	N_2H_3
HO_2	7.55287584e-01	
NO	7.64704477e-01	
N_2O	1.01016545e00	
HNO	7.61288927e-01	
NH_3	6.73071089e-01	
NH	4.56358209e-01	
NH_2	4.68963305e-01	

Table A.1: Species characteristics of the $\text{NH}_3\text{-H}_2$ ARC mechanism.

The mechanism is available at <https://chemistry.cerfacs.fr/>, and detailed description of the reactions is given in Table A.2.

Table A.2: List of reactions with A the pre-exponential factor in $m^{3(n-1)}/\text{kmol}^{n-1} \cdot \text{s}$ with n the order of the reaction, b the temperature exponent and E_a the activation energy in J kmol^{-1} . In the case of fall-off reactions, two sets of Arrhenius coefficients are specified, the first one being the low temperature set and the second one the high temperature set.

No.	Reaction	A	b	E_a
1	$\text{H}_2 + \text{O} \leftrightarrow \text{H} + \text{OH}$	5.080000E+01	2.670000E+00	2.632573E+07
2	$\text{H}_2 + \text{OH} \leftrightarrow \text{H} + \text{H}_2\text{O}$	4.380000E+10	0.000000E+00	2.924616E+07
3	$\text{H} + \text{O}_2 \leftrightarrow \text{O} + \text{OH}$	1.140000E+11	0.000000E+00	6.395662E+07
5	$\text{H}_2\text{O} + \text{O} \leftrightarrow 2 \text{OH}$	6.700000E+04	1.704000E+00	6.270477E+07
6	$\text{H}_2\text{O}_2 (+\text{M}) \leftrightarrow 2 \text{OH} (+\text{M})$	2.490000E+21	-2.300000E+00	2.039658E+08
		2.000000E+12	9.000000E-01	2.039658E+08
7	$\text{H} + \text{H}_2\text{O}_2 \leftrightarrow \text{H}_2 + \text{HO}_2$	2.150000E+07	1.000000E+00	2.510400E+07
8	$\text{H}_2\text{O}_2 + \text{OH} \leftrightarrow \text{H}_2\text{O} + \text{HO}_2$	1.740000E+09	0.000000E+00	1.330512E+06
9	$\text{H}_2\text{O}_2 + \text{OH} \leftrightarrow \text{H}_2\text{O} + \text{HO}_2$	7.590000E+10	0.000000E+00	3.041350E+07
10	$\text{H} + \text{HO}_2 \leftrightarrow 2 \text{OH}$	7.079000E+10	0.000000E+00	1.234280E+06
11	$\text{H} + \text{HO}_2 \leftrightarrow \text{H}_2 + \text{O}_2$	1.140200E+07	1.082700E+00	2.317016E+06
12	$\text{HO}_2 + \text{O} \leftrightarrow \text{O}_2 + \text{OH}$	3.250000E+10	0.000000E+00	0.000000E+00
13	$\text{HO}_2 + \text{OH} \leftrightarrow \text{H}_2\text{O} + \text{O}_2$	7.000000E+09	0.000000E+00	-4.572945E+06
14	$\text{HO}_2 + \text{OH} \leftrightarrow \text{H}_2\text{O} + \text{O}_2$	4.500000E+11	0.000000E+00	4.572945E+07
15	$2 \text{HO}_2 \leftrightarrow \text{H}_2\text{O}_2 + \text{O}_2$	1.000000E+11	0.000000E+00	4.619504E+07
16	$2 \text{HO}_2 \leftrightarrow \text{H}_2\text{O}_2 + \text{O}_2$	1.900000E+08	0.000000E+00	-5.894942E+06
17	$\text{H} + \text{O}_2 (+\text{M}) \leftrightarrow \text{HO}_2 (+\text{M})$	1.737000E+13	-1.230000E+00	0.000000E+00
		4.650000E+09	4.400000E-01	0.000000E+00
18	$\text{O} + \text{OH} + \text{M} \leftrightarrow \text{HO}_2 + \text{M}$	1.000000E+10	0.000000E+00	0.000000E+00
19	$\text{NH}_3 \leftrightarrow \text{H} + \text{NH}_2$	3.497000E+30	-5.224000E+00	4.651072E+08
20	$\text{H} + \text{NH}_2 \leftrightarrow \text{H}_2 + \text{NH}$	4.000000E+10	0.000000E+00	1.527160E+07
21	$\text{H} + \text{NH}_3 \leftrightarrow \text{H}_2 + \text{NH}_2$	1.963000E+01	2.854000E+00	3.564852E+07
22	$\text{NH}_3 + \text{OH} \leftrightarrow \text{H}_2\text{O} + \text{NH}_2$	1.559000E+02	2.372000E+00	4.974776E+05
23	$\text{NH}_3 + \text{O} \leftrightarrow \text{NH}_2 + \text{OH}$	4.430000E-01	3.180000E+00	2.819974E+07

No.	Reaction	A	b	E_a
24	$\text{HO}_2 + \text{NH}_3 \leftrightarrow \text{H}_2\text{O}_2 + \text{NH}_2$	1.173000E-03	3.839000E+00	7.221584E+07
25	$\text{NH}_3 + \text{O}_2 \leftrightarrow \text{HO}_2 + \text{NH}_2$	1.415000E+07	1.285000E+00	2.310572E+08
26	$\text{NH}_2 + \text{O} \leftrightarrow \text{H} + \text{HNO}$	1.500000E+12	-5.470000E-01	3.500753E+06
27	$\text{NH}_2 + \text{O} \leftrightarrow \text{H} + \text{HNO}$	7.730000E+10	-2.770000E-01	2.704538E+06
28	$\text{NH}_2 + \text{O} \leftrightarrow \text{NH} + \text{OH}$	7.000000E+09	0.000000E+00	0.000000E+00
29	$\text{NH}_2 + \text{O} \leftrightarrow \text{NH} + \text{OH}$	3.300000E+05	1.500000E+00	2.124133E+07
30	$\text{NH}_2 + \text{OH} \leftrightarrow \text{H}_2\text{O} + \text{NH}$	9.600000E+03	1.970000E+00	2.803280E+06
31	$\text{NH}_2 + \text{O}_2 \leftrightarrow \text{HNO} + \text{OH}$	2.900000E-05	3.764000E+00	7.608604E+07
32	$\text{HO}_2 + \text{NH}_2 \leftrightarrow \text{H}_2\text{NO} + \text{OH}$	1.566000E+10	0.000000E+00	0.000000E+00
33	$\text{NH} + \text{NH}_2 \leftrightarrow \text{H} + \text{N}_2\text{H}_2$	1.500000E+12	-5.000000E-01	0.000000E+00
34	$\text{NH} + \text{NH}_2 \leftrightarrow \text{N} + \text{NH}_3$	9.600000E+00	2.460000E+00	4.476880E+05
35	$2 \text{NH} \leftrightarrow \text{N} + \text{NH}_2$	5.700000E-04	3.880000E+00	1.430928E+06
36	$2 \text{NH} \rightarrow \text{H}_2 + \text{N}_2$	6.260000E+09	-3.600000E-02	-6.732056E+05
37	$2 \text{NH} \rightarrow 2 \text{H} + \text{N}_2$	5.634000E+10	-3.600000E-02	-6.732056E+05
38	$2 \text{NH}_2 \leftrightarrow \text{NH} + \text{NH}_3$	5.640000E-03	3.530000E+00	2.301200E+06
39	$2 \text{NH}_2 \leftrightarrow \text{N}_2\text{H}_4$	5.600000E+45	-1.130000E+01	4.971554E+07
40	$2 \text{NH}_2 \leftrightarrow \text{H} + \text{N}_2\text{H}_3$	1.200000E+09	-3.000000E-02	4.219146E+07
41	$\text{NH}_2 + \text{NO} \leftrightarrow \text{H}_2\text{O} + \text{N}_2$	2.600000E+16	-2.369000E+00	3.640080E+06
42	$\text{NH}_2 + \text{NO} \leftrightarrow \text{N}_2\text{H} + \text{OH}$	4.300000E+07	2.940000E-01	-3.623344E+06
43	$\text{H} + \text{NH} \leftrightarrow \text{H}_2 + \text{N}$	3.010000E+10	0.000000E+00	0.000000E+00
44	$\text{NH} + \text{O} \leftrightarrow \text{H} + \text{NO}$	3.000000E+10	0.000000E+00	0.000000E+00
45	$\text{NH} + \text{OH} \leftrightarrow \text{H} + \text{HNO}$	2.000000E+10	0.000000E+00	0.000000E+00
46	$\text{NH} + \text{OH} \leftrightarrow \text{H}_2\text{O} + \text{N}$	2.000000E+06	1.200000E+00	0.000000E+00
47	$\text{NH} + \text{O}_2 \leftrightarrow \text{HNO} + \text{O}$	4.050000E+08	9.000000E-02	4.464328E+07
48	$\text{NH} + \text{O}_2 \leftrightarrow \text{NO} + \text{OH}$	2.010000E+12	-1.380000E+00	2.372328E+07
49	$\text{N} + \text{NH} \leftrightarrow \text{H} + \text{N}_2$	6.410000E+08	5.100000E-01	8.368000E+04
50	$\text{NH} + \text{NO} \leftrightarrow \text{H} + \text{N}_2\text{O}$	5.328000E+09	2.600000E-02	-1.210808E+07
51	$\text{NH} + \text{NO} \leftrightarrow \text{N}_2 + \text{OH}$	3.635000E+07	3.610000E-01	-1.190055E+07

No.	Reaction	A	b	E_a
52	$N + OH \leftrightarrow H + NO$	2.830000E+10	0.000000E+00	0.000000E+00
53	$N + O_2 \leftrightarrow NO + O$	9.027000E+06	1.000000E+00	2.719600E+07
54	$N + NO \leftrightarrow N_2 + O$	4.280000E+10	0.000000E+00	6.568880E+06
55	$H + N_2H_4 \leftrightarrow H_2 + N_2H_3$	9.600000E+05	1.500000E+00	2.024345E+07
56	$N_2H_4 + OH \leftrightarrow H_2O + N_2H_3$	1.300000E+10	0.000000E+00	-1.330512E+06
57	$N_2H_4 + NH_2 \leftrightarrow N_2H_3 + NH_3$	3.700000E+03	1.940000E+00	6.819920E+06
58	$N_2H_3 \leftrightarrow H + N_2H_2$	3.600000E+47	-1.038000E+01	2.885864E+08
59	$H + N_2H_3 \leftrightarrow H_2 + N_2H_2$	2.400000E+05	1.500000E+00	0.000000E+00
60	$N_2H_3 + OH \leftrightarrow H_2O + N_2H_2$	1.200000E+03	2.000000E+00	-4.985654E+06
61	$N_2H_3 + NH_2 \leftrightarrow N_2H_2 + NH_3$	9.200000E+02	1.940000E+00	-4.822060E+06
62	$N_2H_2 \leftrightarrow H + N_2H$	1.800000E+40	-8.410000E+00	3.069090E+08
63	$N_2H_2 \leftrightarrow H + N_2H$	2.600000E+40	-8.530000E+00	3.049559E+08
64	$H + N_2H_2 \leftrightarrow H_2 + N_2H$	4.121000E+06	1.289000E+00	-9.376344E+05
65	$N_2H_2 + OH \leftrightarrow H_2O + N_2H$	5.923000E-02	3.400000E+00	-5.705721E+06
66	$N_2H_2 + NO \leftrightarrow N_2O + NH_2$	4.000000E+09	0.000000E+00	4.985654E+07
67	$N_2H_2 + NH \leftrightarrow NH_2 + N_2H$	2.400000E+03	2.000000E+00	-4.985654E+06
68	$N_2H_2 + NH_2 \leftrightarrow NH_3 + N_2H$	8.800000E-05	4.050000E+00	-6.736240E+06
69	$N_2H \leftrightarrow H + N_2$	1.000000E+09	0.000000E+00	0.000000E+00
70	$N_2H + O_2 \leftrightarrow HO_2 + N_2$	5.600000E+11	-3.850000E-01	-5.439200E+04
71	$N_2H + NO \leftrightarrow HNO + N_2$	5.000000E+10	0.000000E+00	0.000000E+00
72	$HNO \leftrightarrow H + NO$	1.825900E+20	-3.008000E+00	2.003299E+08
73	$H + HNO \leftrightarrow H_2 + NO$	9.680000E+08	6.200000E-01	1.506240E+06
74	$HNO + O \leftrightarrow NO + OH$	2.290000E+10	0.000000E+00	0.000000E+00
75	$HNO + OH \leftrightarrow H_2O + NO$	6.300000E+07	3.900000E-01	1.582389E+07
76	$HNO + O_2 \leftrightarrow HO_2 + NO$	2.000000E+10	0.000000E+00	6.232486E+07
77	$HNO + NH_2 \leftrightarrow NH_3 + NO$	3.670000E+04	1.630000E+00	-5.230000E+06
78	$H + H_2NO \leftrightarrow H_2 + HNO$	4.800000E+05	1.500000E+00	6.526203E+06
79	$H + H_2NO \leftrightarrow NH_2 + OH$	4.000000E+10	0.000000E+00	0.000000E+00

No.	Reaction	A	b	E_a
80	$\text{H}_2\text{NO} + \text{OH} \leftrightarrow \text{H}_2\text{O} + \text{HNO}$	2.400000E+03	2.000000E+00	4.988165E+06
81	$\text{H}_2\text{NO} + \text{NH}_2 \leftrightarrow \text{HNO} + \text{NH}_3$	1.800000E+03	1.940000E+00	-2.426720E+06
82	$\text{H}_2\text{NO} + \text{O}_2 \leftrightarrow \text{HNO} + \text{HO}_2$	2.300000E-01	2.994000E+00	6.903600E+07
83	$\text{H}_2\text{NO} + \text{HO}_2 \leftrightarrow \text{H}_2\text{O}_2 + \text{HNO}$	3.360000E+02	2.000000E+00	-5.999856E+06
84	$\text{N}_2\text{O} (+\text{M}) \leftrightarrow \text{N}_2 + \text{O} (+\text{M})$	6.020000E+11	0.000000E+00	2.403457E+08
85	$\text{H} + \text{N}_2\text{O} \leftrightarrow \text{N}_2 + \text{OH}$	2.530000E+07	0.000000E+00	1.903720E+07
86	$\text{H} + \text{N}_2\text{O} \leftrightarrow \text{N}_2 + \text{OH}$	5.000000E+11	0.000000E+00	7.573040E+07
87	$\text{N}_2\text{O} + \text{O} \leftrightarrow 2 \text{NO}$	6.620000E+10	0.000000E+00	1.114199E+08
88	$\text{N}_2\text{O} + \text{O} \leftrightarrow \text{N}_2 + \text{O}_2$	1.020000E+11	0.000000E+00	1.172357E+08

References

- [1] Q. Cazères, P. Pepiot, E. Riber, B. Cuenot, A fully automatic procedure for the analytical reduction of chemical kinetics mechanisms for computational fluid dynamics applications, *Fuel* 303 (2021) 121247.
- [2] P. Pepiot-Desjardins, H. Pitsch, An efficient error-propagation-based reduction method for large chemical kinetic mechanisms, *Combust. Flame* (2008) 67–81.
- [3] P. Pepiot-Desjardins, H. Pitsch, An automatic chemical lumping method for the reduction of large chemical kinetic mechanisms, *Combust. Theory Model.* (2008) 1089–1108.
- [4] T. Løvås, F. Mauss, C. Hasse, N. Peters, Development of adaptive kinetics for application in combustion systems, *Proc. Combust. Inst.* (2002) 1403–1410.
- [5] A. Stagni, C. Cavallotti, S. Arunthanayothin, Y. Song, O. Herbinet, F. Battin-Leclerc, T. Faravelli, An experimental, theoretical and kinetic-modeling study of the gas-phase oxidation of ammonia, *React. Chem. Eng.* 5 (2020) 696–711.

Paper II

Intrinsic instabilities of hydrogen and hydrogen/ammonia premixed flames: influence of equivalence ratio, fuel composition and pressure.

Jessica Gaucherand, Davide Laera, Corinna Schulze-Netzer, Thierry
Poinsot

Combustion and Flame, Vol. 256, Page 112986, (2023).

<https://doi.org/10.1016/j.combustflame.2023.112986>



Contents lists available at ScienceDirect

Combustion and Flame

journal homepage: www.elsevier.com/locate/combustflame

Intrinsic instabilities of hydrogen and hydrogen/ammonia premixed flames: Influence of equivalence ratio, fuel composition and pressure

Jessica Gaucherand^{a,b,*}, Davide Laera^{b,c}, Corinna Schulze-Netzer^a, Thierry Poinso^{b,d}

^a Department of Energy and Process Engineering, Norwegian University of Science and Technology, Trondheim NO-7034, Norway

^b CERFACS, 42 avenue Gaspard Coriolis, Toulouse 31057, France

^c Department of Mechanics, Mathematics and Management, Polytechnic University of Bari, Via Orabona 4, Bari 70125, Italy

^d IMFT, Allée du Professeur Camille Soula, Toulouse 31400, France



ARTICLE INFO

Article history:

Received 1 March 2023

Revised 18 July 2023

Accepted 20 July 2023

Keywords:

Direct numerical simulation

Ammonia and hydrogen

Dispersion relation

Premixed flame

Thermo-diffusive instabilities

ABSTRACT

Premixed lean hydrogen-air flames exhibit instabilities due to hydrodynamic instabilities but also thermo-diffusive instabilities. However, in the case of ammonia/hydrogen blends, the effect of ammonia addition on instabilities is still unclear. To investigate intrinsic instabilities in premixed ammonia/hydrogen-air flames, a parametric study of laminar premixed flames is performed for different fuel contents, from pure hydrogen (H_2) to a blend of 40% of H_2 and 60% of ammonia (NH_3) in volume, equivalence ratios (0.4 to 1.0) and pressures (1 and 10 bar) to investigate thermo-diffusive instabilities. Numerical simulations using detailed chemistry are performed where an initial perturbation is set to disturb the planar flame front and to compute its growth rate. During the initial linear phase, the perturbation's amplitude grows or decreases depending on the flame's mixture propensity to be unstable or stable, respectively. At small times, the linear growth rate of the perturbation can be estimated and compared to theory. As expected, the maximum growth rate obtained in the linear phase depends on the mixture's equivalence ratio, fuel ratio, and pressure. Ammonia addition leads to a reduced peak growth rate, likely due to lower reactivity leading to a higher Zel'dovich number. Very lean mixtures (equivalence ratios of 0.4 and 0.5) are thermo-diffusively unstable, regardless of the ammonia content, due to hydrogen's preferential diffusion.

© 2023 The Author(s). Published by Elsevier Inc. on behalf of The Combustion Institute. This is an open access article under the CC BY license (<http://creativecommons.org/licenses/by/4.0/>)

1. Introduction

Carbon-free fuels have recently been of interest to decarbonize energy systems such as gas turbines, internal combustion engines, boilers and furnaces [1]. Indeed, these fuels, such as hydrogen (H_2) or ammonia (NH_3) emit no CO or CO_2 as they burn with air. However, their introduction in combustors remains a challenge. Indeed, H_2 has a considerable flame speed and wide flammability range, not only requiring the redesign of chambers but also, raising safety issues [2]. Storage and transportation difficulties are also expected from the volatility and low volumetric energy density of H_2 . On the other hand, while NH_3 is easier to store and transport [3], it is characterized by a very low flame speed which limits its direct use in combustion systems. This major drawback can be offset by mixing NH_3 with H_2 : research has shown the potential of mixing these

two fuels to find a compromise in terms of each fuel's advantages and drawbacks [4,5].

To implement H_2 and NH_3 mixtures as fuels at a large scale, a fundamental understanding of the flame front structures and propagation is necessary. Experimental and numerical works have highlighted the effect of preferential diffusion in lean H_2 flames, leading to thermo-diffusive instabilities [6,7]. These flames are characterized by significant wrinkling, enhanced speed, and shortened length. Thermo-diffusive instabilities have been experimentally studied in different setups such as laminar and turbulent spherical flames [8], fan-stirred chamber and coflow jets at high Reynolds number [9]. Numerically, direct numerical simulations (DNS) are often used to investigate such phenomena. Lean H_2 -air premixed flames have been investigated using DNS, showing that thermo-diffusive effects strongly affected the flame [10,11]. These studies showed that models for turbulent premixed flame need to account for thermo-diffusive effects at two levels:

- locally, along the flame front, each unit surface of the flame can burn, on average, more than the laminar-unstrained flame speed, S_L^0 . This can be measured through an indicator I_0 defined

* Corresponding author at: Department of Energy and Process Engineering, Norwegian University of Science and Technology, Trondheim NO-7034, Norway.
E-mail address: gaucherand@cerfacs.fr (J. Gaucherand).

by the normalized, surface averaged consumption speed along the front:

$$l_0 = \frac{< s_c >}{s_l^0}. \quad (1)$$

- Cells are formed on the flame front, independently of any wrinkling due to turbulent eddies. This wrinkling due to thermo-diffusive effects is called Θ_0 and is defined by:

$$\Theta_0 = \frac{\Sigma}{L_x}. \quad (2)$$

where Σ is the flame surface and L_x the reference or initial flame surface.

The overall effects of thermo-diffusive instabilities are measured by the product $l_0\Theta_0$ which indicates the factor by which the total reaction rate increases. Values of $l_0\Theta_0$ up to 4 have been reported by Berger et al. for a turbulent lean H_2 -air flame at equivalence ratio $\phi = 0.4$ [10]. $l_0\Theta_0$ up to six were observed experimentally for premixed turbulent spherical H_2 -air flames while $l_0\Theta_0$ for CH_4 flames were close to unity [8]. Increasing the pressure also increases $l_0\Theta_0$ as demonstrated for a premixed turbulent H_2 -air at $\phi = 0.7$ for pressures going from 1 to 7 bar [12].

Preferential diffusion effects have also been observed for premixed turbulent $NH_3/H_2/N_2$ -air (40% NH_3 , 45% H_2 , and 15% N_2 in the fuel) flames at $\phi = 0.45$ with $l_0\Theta_0$ above 1.5 [13]. On the other hand, at $\phi = 1$, for a premixed turbulent NH_3/H_2 -air flame (54% NH_3 , and 46% H_2), unity $l_0\Theta_0$ values were found [14]. Rieth et al. [15] also found enhanced effects, at high pressure, of molecular hydrogen diffusion in leading points for premixed $NH_3/H_2/N_2$ -air when comparing initial pressures at 1 bar and 10 bar. These results indicate that equivalence ratio, fuel and composition (in the case of blends), and initial pressure affect the development of thermo-diffusive instability.

A simple solution to predict the occurrence of thermo-diffusive instabilities would be to rely on theory [16–18]. Theoretical analyses of these instabilities have been carried out for decades for laminar premixed flames undergoing a small perturbation. Matalon and Matkowsky assumed a global one-step reaction [16] for Lewis close to unity, and Sivashinsky considered a small density jump throughout the flame front but accounted for a small Lewis number [19,20]. Recently, Berger et al. [21] have shown that these theories do not accurately capture the evolution of lean premixed H_2 -air flames [21]. Accounting for fuel mixtures and complex chemistry is another difficulty. This is where simulations can be introduced: a stability analysis can be performed using 2-D DNS, where a planar flame is exposed to a small perturbation. During the first instants, also called the linear phase, the perturbation's amplitude will either grow or decrease: the growth rate of a given wavelength can be evaluated to reconstruct a dispersion relation [21,22]. This dispersion relation quantifies the stability of a given mixture.

Numerical studies of dispersion relations have been carried out using DNS by Berger et al. [21] in a parametric study to investigate premixed H_2 -air flames by varying the equivalence ratio, initial pressure, and temperature using detailed chemistry. Detailed chemistry was also used by Altantzis et al. [23] to study lean premixed H_2 -air at $\phi = 0.6$ and 5 atm for different domain lengths. Frouzakis et al. [22] studied H_2 -air for $0.5 \leq \phi \leq 2.0$ and found good agreement of theoretical dispersion relation for $\phi \geq 0.75$. Yuan et al. [24] used one-step chemistry to simulate flames with unity Lewis numbers to study the effect of increasing pressure up to 5 bar. Higher pressure was investigated by Yu et al. [25] for a premixed H_2 -air flame at $\phi = 0.6$ who found enhanced hydrodynamic instabilities for high-pressure cases. Studies have highlighted preferential diffusion in premixed NH_3/H_2 -air flame experimentally in expanding spherical flames [26,27]. Dampened thermo-diffusive instabilities were observed qualitatively in lean

conditions (up to $\phi = 0.6$) when increasing the amount of NH_3 [26] in NH_3/H_2 mixtures. However, increasing the initial pressure destabilized NH_3/H_2 -air flames at $\phi = 0.8$ and $\phi = 1.0$ [27]. However, to the authors' knowledge, no dispersion relation has been computed yet for NH_3/H_2 -air flames and compared to theoretical relations. In fact, due to the large difference between the Lewis number of the two fuels, as well as the possible dissociation of ammonia into hydrogen for intermediate temperature, the question of whether ammonia addition will dampen the instabilities is an open one with no definitive answer. Notably, some research has highlighted a non-monotonic evolution of the Markstein number for fixed equivalence ratio and varying H_2 content in NH_3/H_2 mixtures [28,29]. Therefore, several hypotheses can be formulated about what the effect of ammonia addition to hydrogen might lead to: 1) NH_3 dissociating into H_2 at intermediate temperature could lead to more instabilities, 2) H_2 could dominate the flame front destabilization and the NH_3/H_2 flame might behave like a pure H_2 flame, 3) or NH_3 addition might dampen the instabilities.

The present work aims to fill the literature gap by providing growth rate values for an extensive range of mixtures, varying equivalence ratios, and fuel composition from pure hydrogen to mixtures of ammonia and hydrogen up to 60% of ammonia in volume. The effect of pressure on instabilities will also be investigated for cases at $\phi = 0.5$ for pure H_2 and for a blend of 50% of NH_3 and H_2 in volume. DNS using detailed chemistry will provide quantitative information on the strength of thermo-diffusive instabilities for these mixtures, to be compared with theory. Thermo-diffusive instabilities will also be compared to hydrodynamic instabilities to investigate if NH_3/H_2 -air flames can be thermo-diffusively unstable, how does NH_3 affects the flame stability, and how high pressure affects NH_3/H_2 flames. These will provide useful insights on the mixtures' impact on thermo-diffusive instabilities, which is needed for the combustion model development for ammonia/hydrogen and supports the fuel blend selection for retrofitting. Section 2 covers the theoretical dispersion relation formulas, the numerical setup, the parametric variations performed, and the methodology to compute the numerical relation dispersion. Section 3.1 presents the results obtained for the numerical dispersion relation, Section 3.2 presents expressions for the Lewis number of NH_3/H_2 blends which are then used in Section 3.3 to compare the dispersion relation from the DNS results with theoretical predictions [16,19,30]. The impact of other global flame parameters is also investigated in Section 3.4, and a fit of the peak growth rate based on the DNS data is provided in Section 3.5 before concluding in Section 4.

2. Theory, numerical setup and methodology to compute the flame growth rate

2.1. Theoretical background of flame response to perturbation

Works by Darrieus and Landau [30,31] showed how planar flames were intrinsically unstable due to hydrodynamic instabilities caused by the density jump in the flame front from fresh to burned gases. The hydrodynamic instability ω_{DL} can be defined as:

$$\omega_{DL} = \frac{\sqrt{\sigma^3 + \sigma^2 - \sigma} - \sigma}{\sigma + 1}, \quad (3)$$

where $\sigma = \frac{\rho_u}{\rho_b}$ is the expansion ratio equal to unburned over burned density. The non-dimensional growth rate $\tilde{\omega}$ dependency with respect to non-dimensional wave number \tilde{k} can be written in a first estimation as :

$$\tilde{\omega} = \omega_{DL} \tilde{k}, \quad (4)$$

where $\tilde{\omega} = \omega \tau$ and $\tilde{k} = k \delta_L^0$. The flame time τ corresponds to the ratio of the flame thermal thickness δ_L^0 to the unstretched flame

speed s_l^0 and the thermal thickness δ_l^0 is defined by :

$$\delta_l^0 = \frac{T_{ad} - T_u}{\max(\nabla T)}, \quad (5)$$

where T_u is the initial flame temperature, and T_{ad} is the adiabatic flame temperature. However, numerical and experimental work have not observed this unconditional instability, and Eq. (4) is incomplete. New dispersion relations have been derived, such as the one by Matalon et al. [16] where a second-order term is added to account for a stabilizing or destabilizing behavior due to Lewis number effects:

$$\bar{\omega} = \omega_{DL} \bar{k} - \delta [B_1 + \beta (Le_{eff} - 1) B_2 + P_r B_3] \bar{k}^2 = \omega_{DL} \bar{k} - \omega_2 \bar{k}^2. \quad (6)$$

The diffusive flame thickness $\delta_D = D_{th}/s_l^0$, where D_{th} is the thermal diffusivity, is needed to define $\delta = \delta_D/\delta_l^0$. The coefficients B_1 , B_2 , and B_3 are functions of the expansion ratio, the thermal conductivity evolution with temperature, and ω_{DL} [32]:

$$B_1 = \frac{\sigma}{2(\sigma + (\sigma + 1)\omega_{DL})} \left(\frac{\sigma(2\omega_{DL} + \sigma + 1)}{\sigma - 1} \int_1^\sigma \frac{\bar{\lambda}(x)}{x} dx + \int_1^\sigma \bar{\lambda}(x) dx \right), \quad (7)$$

$$B_2 = \frac{\sigma(1 + \omega_{DL})(\sigma + \omega_{DL})}{2(\sigma - 1)(\sigma + (\sigma + 1)\omega_{DL})} \int_1^\sigma \log\left(\frac{\sigma - 1}{x - 1}\right) \frac{\bar{\lambda}(x)}{x} dx, \quad (8)$$

$$B_3 = \frac{\sigma}{\sigma + (\sigma + 1)\omega_{DL}} \left((\sigma - 1)\bar{\lambda}(\sigma) - \int_1^\sigma \bar{\lambda}(x) dx \right), \quad (9)$$

where $\bar{\lambda} = \lambda/\lambda_u$ is the normalised thermal conductivity and $x = T/T_u$.

The Prandtl number P_r , the Zel'dovich number β , and the effective Lewis number Le_{eff} are also needed in Eq. (6). Zel'dovich number β for detailed chemistry is computed using the approach proposed by Law et al. [33] to evaluate the overall activation energy:

$$\frac{E_a}{R} = -2 \frac{d(\rho_u S_l^0)}{d(1/T_{ad})}, \quad (10)$$

where R is the universal gas constant. To vary the adiabatic temperature and calculate Eq. (10), two 1-D flames are computed where the amount of N_2 is varied slightly ($\pm 0.3\%$). The overall activation energy is computed with the gradient of the line obtained using a linear fit of the curve given by plotting $\rho_u S_l^0$ over $1/T_{ad}$, using the results of the two 1-D flames. The values of E_a used in this work are provided in the Supplementary Material in Fig. C.1. The Zel'dovich number β is given by:

$$\beta = \frac{E_a(T_{ad} - T_u)}{RT_{ad}^2}. \quad (11)$$

Matalon et al.'s dispersion relation Eq. (6) is derived for Lewis numbers close to unity, where the second term of the expression ω_2 has a stabilizing effect. However, for lower values of Lewis number, ω_2 is positive: the dispersion relation becomes destabilizing for all wave numbers. Sivashinsky [19,20] derived a dispersion relation for the linear phase accounting for a fourth-order term that is stabilizing regardless of the Lewis number:

$$\bar{\omega} = \delta \left[\frac{\beta}{2} (1 - Le) - 1 \right] \bar{k}^2 - 4\delta^3 \bar{k}^4. \quad (12)$$

Another relation by Sivashinsky was derived for the non-linear flame evolution but is outside the scope of this work [34].

Further dispersion relations have been established by Pelce and Clavin [17], Klimentko and Class [35], Chung and Law [36] and others. Lipatnikov and Chomiak [37] reviewed the assumptions needed to derive dispersion relations and presented different theoretical relations, but the scope of our study will be limited to the theories of Darrieus-Landau (Eq. (4)), Matalon et al. (Eq. (6)),

and Sivashinsky's (Eq. (12)) dispersion relations for comparison in Section 3.3.

A critical parameter in all theoretical evaluations of $\bar{\omega}$ is the effective Lewis number Le_{eff} . Defined by Joulin and Mitani [38] for two reactant flames, Le_{eff} is given by:

$$Le_{eff} = \begin{cases} \frac{Le_f + A Le_o}{1+A}, & A = 1 + \beta(\phi^{-1} - 1) \quad \text{if } \phi < 1, \\ \frac{Le_f + A Le_o}{1+A}, & A = 1 + \beta(\phi - 1) \quad \text{if } \phi > 1, \end{cases} \quad (13)$$

where Le_f and Le_o are the fuel's and oxidant's Lewis numbers. Oxygen O_2 is taken as the oxidant. When only one fuel is considered, the effective Lewis number is straightforward to derive, using the fuel's Lewis number in Eq. (13) (i.e. in the case of pure H_2). However, for a fuel mixture, the fuel's Lewis number requires a new evaluation. Several definitions have been suggested and validated against experiment [39,40]. Three of them have been considered here. The first one (Le_V) was proposed by Muppala et al. [41], who suggested a volume-based formulation of the fuel's Lewis number (Le_V), based on the volume fraction (X_i) of each fuel in the fuel mixture:

$$Le_V = \sum_{n=1}^f X_i Le_i, \quad (14)$$

with f the number of fuels in the fuel mixture. Dinkelacker et al. [42] proposed a diffusion-based (Le_D) formula:

$$\frac{1}{Le_D} = \sum_{n=1}^f \frac{X_i}{Le_i}, \quad (15)$$

Law et al. [43] used a heat release-based formulation (Le_Q), where the Lewis number of each fuel is weighted by the nondimensional heat release (q_i) based on the consumption of each fuel:

$$Le_Q = 1 + \frac{\sum_{n=1}^f q_i (Le_i - 1)}{\sum_{n=1}^f q_i}, \quad (16)$$

with

$$q_i = \frac{Q_i Y_{i,u}}{C_p T_u}, \quad (17)$$

where Q_i is the heat of reaction of the fuel i and $Y_{i,u}$ its mass fraction far upstream. In the case of NH_3/H_2 -air flames, Zitouni et al. [29] found that the Le_V definition matched their experimental results quite well, that the Le_D formulation was more suited for lean mixtures, and Le_Q was accurate in richer conditions. In this study, an analysis of strained flame will be performed to determine the most suited definition for the Lewis number in Section 3.2 and will be used to compute the theoretical dispersion relations discussed in Section 3.3. This comes as an addition to the scarce literature on the topic of a suited Lewis number definition for mixtures of ammonia and hydrogen.

2.2. Numerical setup

The reacting Navier–Stokes equations are solved with the compressible solver AVBP¹ [44], an explicit massively parallel code solving the conservation of mass, momentum, energy equations, and species transport. The flow is gaseous and NH_3/H_2 -air chemistry is modeled using an analytically reduced chemistry mechanism derived from CRECK [45] and reduced with Arcane [46] (18 species, 6 species with QSS assumption and 150 reactions). Validation of the mechanism is presented in the Supplementary Materials in Fig. A.1. The reduced mechanism is also included in the Supplementary Materials. A power law is used to compute the molecular viscosity $\mu = \mu_{ref}(T/T_{ref})^b$. Constant Schmidt S_c and Prandtl

¹ <http://www.cerfacs.fr/avbp7x>.

Table 1

Overview of the 2-D DNS. For each case, the content of ammonia in volume in the fuel X_{NH_3} , the equivalence ratio ϕ , the initial pressure P , the laminar flame speed s_L^0 , the thermal flame thickness δ_T^0 , the diffusive flame thickness δ_D and the adiabatic temperature T_{ad} are provided.

Case name	X_{NH_3} [%]	ϕ [-]	P [bar]	s_L^0 [m/s]	δ_T^0 [μm]	δ_D [μm]	T_{ad} [K]
NH3-00-Phi-04	0	0.4	1	0.25	562	105	1416
Ref	0	0.5	1	0.56	382	49	1625
NH3-00-Phi-1	0	1.0	1	2.27	326	14	2242
NH3-03-Phi-04	30	0.4	1	0.07	1389	366	1343
NH3-03-Phi-05	30	0.5	1	0.19	686	139	1534
NH3-03-Phi-1	30	1.0	1	0.93	317	31	2222
NH3-05-Phi-04	50	0.4	1	0.02	3840	1187	1316
NH3-05-Phi-05	50	0.5	1	0.09	1277	307	1502
NH3-05-Phi-1	50	1.0	1	0.46	432	61	2169
NH3-06-Phi-04	60	0.4	1	0.01	8493	2657	1301
NH3-06-Phi-05	60	0.5	1	0.05	1983	506	1487
NH3-06-Phi-1	60	1.0	1	0.31	576	89	2147
NH3-00-Phi-05-10-bar	0	0.5	10	0.15	80	18	1633
NH3-05-Phi-05-10-bar	50	0.5	10	0.01	1099	60	1513

P_i numbers are used for species molecular diffusion: $D_k = \mu/S_{c_k}$, for species k , and for thermal conductivity: $\lambda = \mu C_p/P_i$ with C_p the specific heat capacity of the mixture. In the Supplementary Materials, a comparison between constant Lewis number assumption and varying Lewis number is illustrated for the reference case, with an overall good agreement, leading to the validity of the constant Lewis number assumption in these premixed flames.

The numerical scheme used to solve the equations is Lax–Wendroff [47], a second-order scheme in space and time. A third-order accurate in space and time Taylor–Galerkin finite-element scheme was also tested with no major difference, therefore the second-order scheme was used in the parametric study to save computational time. Simulations are performed in 2-D rectangular domains with length L_x and height L_y . Cartesian meshes are used to discretize the domain with the selected cell size to have 40 grid points in the thermal flame thickness δ_T^0 . At the inlet (bottom of the rectangular domain), fresh gases are injected at a velocity equal to the laminar flame speed of the mixture computed with Cantera [48]. The flow exits the domain at the outlet (top of the rectangular domain), where static pressure is imposed. Inlet and outlet use non-reflecting NSCBC boundary conditions [49]. Periodic conditions are imposed in the spanwise direction x . Initially, the flame front is mapped onto the domain using a 1D flame computed with Cantera and is perturbed with a sinusoidal perturbation $F(x)$:

$$F(x) = A_0 \sin(kx), \quad (18)$$

with A_0 the initial amplitude of the perturbation, selected to be 2% of δ_T^0 (to remain in the linear regime), and k is the wave number of the perturbation. L_x is selected to be equal to the wavelength of the imposed perturbation: $\lambda = 2\pi/k = 2\pi/n\delta_T^0$, with n varying between 1 and 60. L_y corresponds to $24\delta_T^0$, and the initial perturbation is imposed at $18\delta_T^0$ in the y -axis (Fig. 1(a)).

An initial temperature T_i of 300K is selected for all conditions. The reference case is set for pure hydrogen at $\phi = 0.5$ at atmospheric pressure to compare the results with literature data and validate the methodology. Parametric variations of the equivalence ratio from $\phi = 0.4$ to 1 are performed. A parametric variation of ammonia concentration in the fuel composition from $X_{\text{NH}_3} = 0\%$ to 60% in volume is also performed. Some fuel blends are selected to be computed at 10 bar to study the effect of pressure at $\phi = 0.5$. An overview of the 14 simulations performed is presented in Table 1.

2.3. Methodology for growth rate computation

The early flame propagation is investigated to compute the dispersion relation. Below a critical wave number k_c , the flame front

perturbation will either grow or decrease exponentially with time. The growth rate is computed with the flame front's amplitude evolution, tracked using the isoline $T = 3T_i$ to define the flame front. The amplitude of the first mode of the Fourier transform of the flame front is computed at each time step and tracked, providing the time evolution of the amplitude $A(t)$. The exponential growth rate ω is computed during the linear phase by:

$$\omega = \frac{d}{dt} [\ln(A(t))] \quad (19)$$

Care is taken to verify that the linear phase is well captured, as verified by the existence of a plateau at small times (between 0 and $\approx 6\tau$ in Fig. 1(c)) for ω as a function of time. The dispersion relation $\omega(k)$ is then obtained as a function of the wave number k as the procedure is repeated for different domain lengths. The numerical setup and operation for the dispersion relation extraction are described in Fig. 1. To validate the methodology, it was first applied to a pure H_2 air, $\phi = 0.5$ case and compared to the results of Berger et al. [21] and Frouzakis et al. [22] in Fig. 2. Good agreement with Frouzakis et al. [22] is obtained, whereas, at large wave numbers, a small deviation is observed with results from Berger et al. [21]. These small differences are likely due to different chemistry, transport properties, and DNS code.

3. Linear regime: linear stability analysis

3.1. Analyses of DNS database

At low equivalence ratio, characteristics of thermo-diffusive instabilities are recovered: super adiabaticity and higher heat release captured in positive curvature zones (i.e., zones where velocity streamlines are convex towards burned gases) than in negative curvature zones (i.e., zones where velocity streamlines are concave towards burned gases) as observed in Fig. 3 for pure H_2 cases at different equivalence ratios and Fig. 4 for an equivalence ratio of 0.4 at different NH_3 to H_2 ratios in the fuel. This was observed for lean pure H_2 by Howarth and Aspden [50], but we also observe this for lean NH_3/H_2 mixtures. The dispersion relations obtained by DNS are presented for different equivalence ratios and fuel compositions (Fig. 5) and pressure variations (Fig. 6). The symbols are the growth rate computed numerically for each domain size. A second-order polynomial fit of the growth rates is also plotted. Non-dimensionalized units of the growth rate versus the wave number ($\omega\tau$ versus $k\delta_T^0$) are used for all plots.

As expected, for all cases, $\omega\tau$ grows due to the destabilization of small wave numbers induced by hydrodynamic instabilities. Then $\omega\tau$ decreases for larger wave numbers $k\delta_T^0$ due to

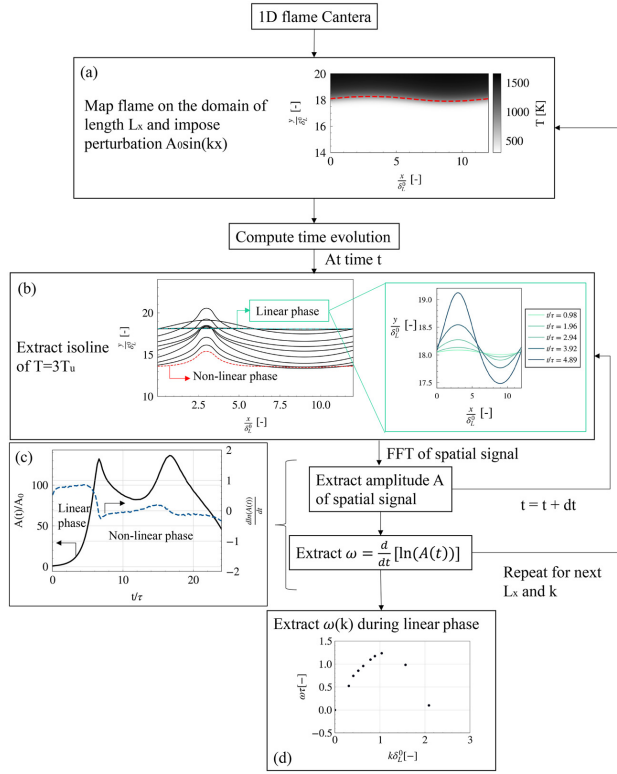


Fig. 1. Flowchart of the set up description and the extraction of $\omega(k)$.

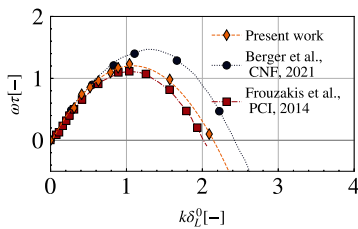


Fig. 2. Dispersion relation obtained in the methodology of Fig. 1 compared to the work by Berger et al. [21], and Frouzakis et al. [22] for pure H_2 at $\phi = 0.5$ and 1 bar.

thermo-diffusive effects within the flame front. To appreciate the effect of the hydrodynamic stability limit, $\omega_{DL}\tau$ as a function of the wave number is also plotted on the same figures for each mixture. A nearly constant expansion ratio for each fuel mixture at a given equivalence ratio leads to $\omega_{DL}\tau$ being almost superimposed.

For small wave numbers, cases at $\phi = 0.4$ have $\omega\tau$ exceeding $\omega_{DL}\tau$ which indicates that the contribution of the thermo-diffusive instability is to make the mixture more unstable (positive contribution of thermo-diffusive instabilities). On the other hand, at $\phi = 1.0$, the negative contribution of thermo-diffusive effects is observed since $\omega\tau$ are all below $\omega_{DL}\tau$. At 1 bar, the most unstable

mixture ($\omega_{max}\tau$ shown in Fig. 7(c)) corresponds to pure hydrogen at $\phi = 0.4$, with a maximum growth rate of more than twice that of $\phi = 1.0$. Figure 5 shows that the maximum growth rate obtained in the simulations diminishes with increasing equivalence ratio regardless of the fuel composition. This indicates the propensity of leaner mixtures to be more thermo-diffusively unstable, likely due to the small effective Lewis number of the mixture, indicating preferential diffusion. This had been observed by Berger et al. [21] and Frouzakis et al. [22] in the case of pure hydrogen. Figure 5 shows that these findings can be generalized for lean NH_3/H_2 flames. In Fig. 7, where the normalized maximum growth rate of each mixture is reported, we see that thermo-diffusive instabilities are reduced when the NH_3 content in the fuel increases at any given equivalence ratio, with a collapse of peak growth rate for all cases at stoichiometry.

Regarding the effects of pressure, Fig. 6 indicates a larger growth rate for 10 bar in the case of pure H_2 at $\phi = 0.5$ compared to 1 bar, as observed by Berger et al. [21] and Attili et al. [51] for CH_4 . The same trend is found for the NH_3/H_2 case experimentally by Li et al. [27]. This is caused by both the thinner flame causing more instabilities at high pressure and the enhanced reactivity. Consistent in our simulations, ammonia addition makes the flame more stable than the pure hydrogen case at high pressure. These results also highlight the importance of pressure on instability dependency and should be considered for pressurized engine-like conditions.

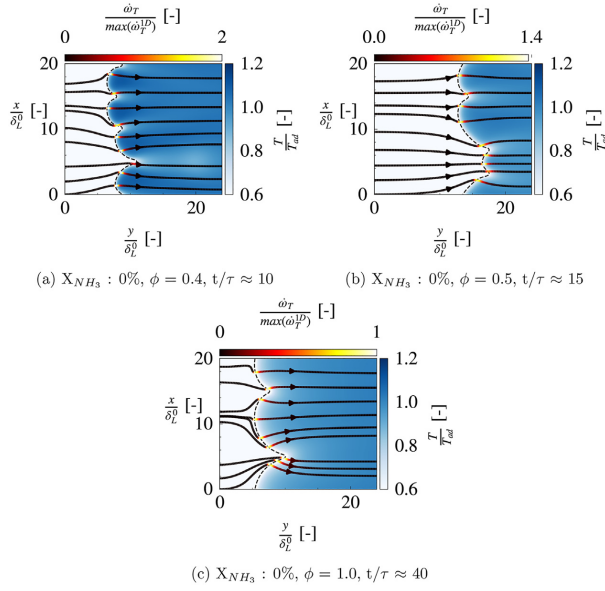


Fig. 3. Contour of normalized temperature, isocontour of temperature of $T = 3T_u$, in dashed lines, and velocity streamlines in solid lines colored by normalized heat release rate. Snapshots are taken at $t/\tau \approx 10, 15$, and 40 in the right column. Pure H_2 cases $\phi = 0.4, 0.5$ and 1.0 .

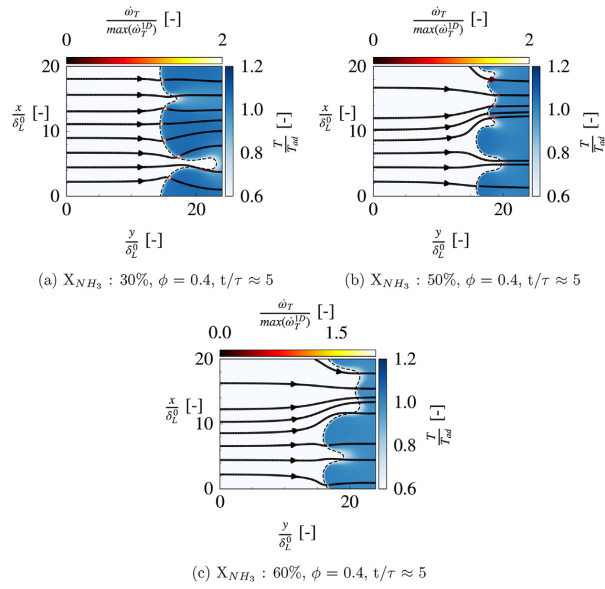


Fig. 4. Contour of normalized temperature, isocontour of temperature of $T = 3T_u$, in dashed lines, and velocity streamlines in solid lines colored by normalized heat release rate. Due to the slower flame speed, snapshots are taken at $t/\tau \approx 5$ in the right column. Mixtures with 30%, 50%, and 60% for $\phi = 0.4$.

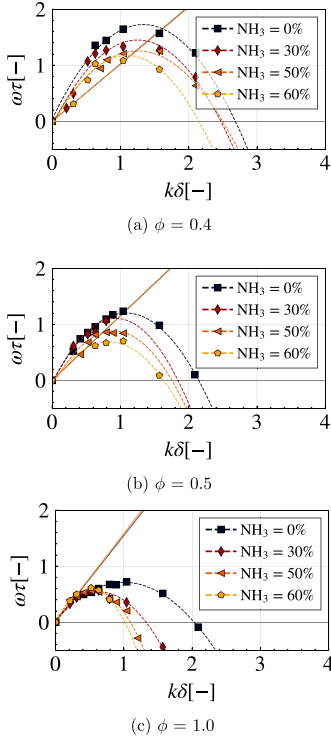


Fig. 5. Dispersion relation for varying equivalence ratio, at various NH_3 contents in volume in the fuel. Symbols correspond to the growth rates extracted from the simulations, dashed lines correspond to the second-order polynomial fit of these growth rates. The theoretical hydrodynamic growth rate $\omega_{D\ell}\tau$ is also shown in solid line for all mixtures.

A cut-off wavelength λ_c (Fig. 7(a) and (d)) associated with the cut-off wavenumber k_c where $\omega\tau$ become negative can be obtained from Figs. 5, 6. The normalized maximum growth rate $\omega_{\max}\tau$ (Fig. 7(c) and (f)) and the wavelength associated with the maximum growth rate $\lambda_{\omega_{\max}}$ (Fig. 7(b) and (e)), are also reported. The scaling of the critical wavelength λ_c and of $\lambda_{\omega_{\max}}$ depends directly on the flame thickness evolution δ_f^0 . Finally, the dispersion relation of NH_3/H_2 mixtures evolves in a similar manner with equivalence ratio and pressure as pure H_2 . NH_3 reduces the peak growth rate and, by extension, the instabilities for the investigated range of fuel content and equivalence ratio. We highlight that potentially, some proportions of ammonia and hydrogen could cause dissociation of ammonia into hydrogen, therefore leading to more instabilities, but that is not captured in the early linear phase of the flame front evolution and the peak growth rate increases with H_2 content in these cases.

3.2. Evaluation of Lewis number for NH_3/H_2 blends

For model development, finding global flame parameters to predict thermo-diffusive instabilities and computing theoretical relation dispersion instead of performing parametric sweeps with DNS would be preferred to limit the computational cost. However, these theoretical expressions still need to be verified and val-

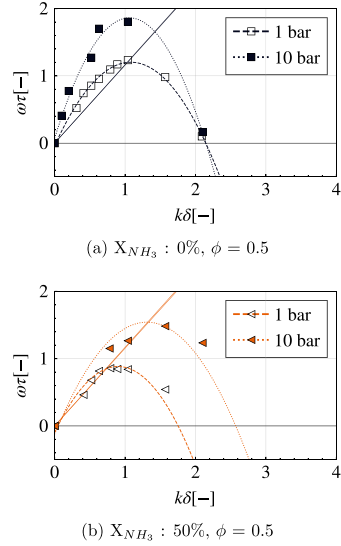


Fig. 6. Dispersion relation for varying pressures, for NH_3 at 0% and 50% content in volume in the fuel at $\phi = 0.5$. Symbols correspond to the growth rates extracted from the simulations, dashed lines correspond to the second-order polynomial fit of the growth rates of cases at 1 bar, and the dotted lines to the growth rates with at 10 bar. The theoretical hydrodynamic growth rate $\omega_{D\ell}\tau$ is also shown in solid line for all mixtures.

idated. For these compositions of ammonia/hydrogen, as discussed in Section 2, a suited definition for the effective Lewis number of a fuel blend needs to be evaluated. To do so, Cantera simulations of premixed, slightly strained flames are performed to compute the Markstein length [52] of the mixtures at different equivalence ratios. In these twin flames simulations, the premixed flame is obtained with a counterflow of two streams of fresh gases going against one another, leading to a strained flame [53]. This is done for the cases at 1 bar only. We compute the strain $\kappa = 2\dot{m}_u/\rho_u/w$ (\dot{m}_u is the mass flow rate of the reactants and w the domain width between the two streams) and the flame consumption speed s_c in order to compute the Markstein length at small strains [54,55]:

$$L_b = \frac{s_l^0 - s_c}{\kappa}. \quad (20)$$

A negative (positive) value of the Markstein number, typically indicates an unstable (stable) mixture. Theoretical relations [54–56] link the Markstein length to global flame parameters: σ , β , x , λ and Le_{eff} which were defined in Section 2 :

$$Ma = \frac{L_b}{\delta_D} = \frac{\beta(Le_{eff} - 1)}{2(\sigma - 1)} \int_1^\sigma \frac{\tilde{\lambda}(x)}{x} \ln \frac{\sigma - 1}{x - 1} dx. \quad (21)$$

By comparing the Markstein length from Cantera simulation with Eq. (21), it is possible to evaluate the best definition of the Lewis number. This is shown in Fig. 8 for three fuel compositions (30, 50 and 60% of NH_3) at atmospheric pressure. For the case with 30% NH_3 , the strained Markstein length (20) is closest to the Markstein derived with the volume-based definition of the Lewis number (Le_V) compared to the other definitions. At 50% NH_3 , the results from equivalence ratio 0.6 to 1 match very well the results using Le_V . Finally, the results for 60% NH_3 for the strained flame are between the volume-based definition (Le_V) and the diffusion-based definition (Le_D). Eq. (21) was derived for constant viscos-

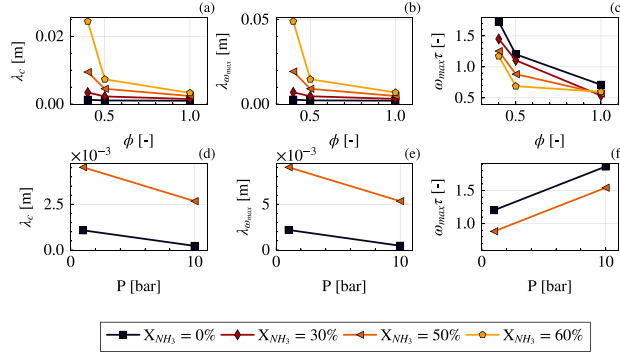


Fig. 7. Variation of the cut-off wavelength λ_c , the wavelength associated with the peak growth rate $\lambda_{\omega_{\max}}$, and the peak growth rate $\omega_{\max}\tau$. Top: Variation of equivalence ratio ϕ for different NH_3 fuel ratios. Bottom: Effect of initial pressure P for different NH_3 fuel ratios at equivalence ratio $\phi = 0.5$.

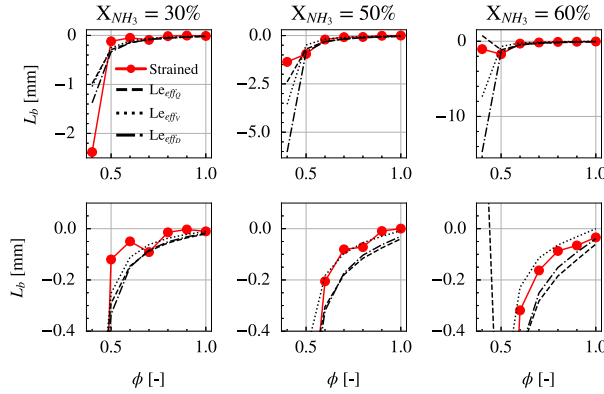


Fig. 8. Markstein length derived from Eq. (20) compared with Eq. (21) using different effective Lewis number definitions based on Le_Q , Le_V and Le_D . Top: full data points, bottom: a zoom on the y-axis to determine the most suited Lewis number definition.

ity with single-step flame, where the Zel'dovich number β was also derived with assumptions to compute the activation energy. Therefore, the computation of the theoretical formulas for β and L_b leads to uncertainty in the results to compare the Lewis numbers. We also note that at a low equivalence ratio ($\phi = 0.4$), the strained-derived Markstein number is not well reproduced with any of the Lewis definitions in the theoretical relation (21). Here we suggest that, among all the investigated definitions, Le_V best captures, overall, the instabilities of the mixtures compared to the other definitions for the NH_3/H_2 mixture for different equivalence ratios in lean to stoichiometric cases. This is a similar conclusion reached by Zitouni et al. [29] for a large range of equivalence ratio and NH_3/H_2 ratio.

3.3. Comparison of DNS-derived relation dispersion with theoretical dispersion relations

The Lewis number definition Le_V (Eq. (14)) based on volume is then used in the theoretical dispersion relations of Sivashinsky Eq. (12) and Matalon's Eq. (6). We present the results for the three equivalence ratios in this study $\phi = 0.4, 0.5, \text{ and } 1$, and for the cases with pure H_2 and 50% of NH_3 . The relation dispersions

for $\phi = 0.4, 0.5, \text{ and } 1$ for all fuel contents are presented in the Supplementary Materials in Fig. B.1.

Matalon's theory [16] captures the stabilizing effect of large wave numbers for very large values of k for cases $\phi = 0.4$ and 0.5 , not seen on the figure due to the x -axis limit. Large deviations from the DNS-derived dispersion relation are found, with the cut-off wavelength and the peak growth rate not reproduced with the two theoretical relation dispersions. This is true for leaner cases since Matalon's relation for the stoichiometric case leads to a closer cut-off wavelength and peak growth rate to the DNS results. The model by Sivashinsky [19] predicts the stabilizing effects at high wave numbers thanks to the inclusion of the fourth-order term. For all cases, the cut-off wavelength and peak growth rate are not well evaluated compared to the DNS results due to density variation throughout the flame front not being included in Sivashinsky's model. Section 3.2 showed the difficulty of the mixture's Lewis number definitions to reproduce the Markstein at these low equivalence ratios. We find that theoretical formulas for the dispersion relation also struggle to match results with DNS for pure H_2 for which the Lewis number definition is well defined. This suggests that these theories are not able to capture the flame behavior at a low equivalence ratio, even if the Lewis number is

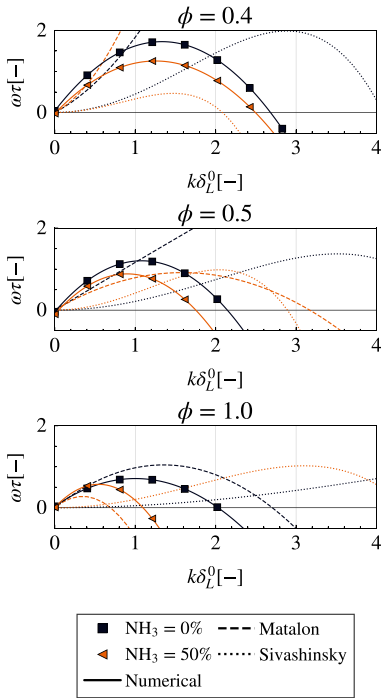


Fig. 9. Computed dispersion relation (solid line with symbol) compared with the theoretical dispersion relation using the volume-based definition of the Lewis number: Matalon's dispersion relation Eq. (6) (dashed line) and Sivashinsky's relation Eq. (12) (dotted line). ω_{DL} is not pictured as it was already in Fig. 5. Case $\phi = 0.4, 0.5$ and 1 for 0% NH_3 and 50% NH_3 .

not well defined at small equivalence ratios. Overall, these results indicate a need for theoretical dispersion relations to account for preferential diffusion effects occurring at small equivalence ratios to be suited for H_2 and mixtures of NH_3/H_2 (Fig. 9).

3.4. Impact of Zel'dovich number and expansion ratio

To assess the impact of ammonia addition on other global flame parameters, and understand its stabilizing effect seen in Section 3, Fig. 10 presents the values obtained from one-dimensional Cantera simulation for the unstretched laminar velocity, Zel'dovich number, and expansion ratio -defined Section 2- to measure the impact of these global parameters on the instabilities. We consider both cases at 1 and 10 bar. The laminar flame speed increases with equivalence ratio up to stoichiometry and increases with the hydrogen content in the fuel. At $\phi = 0.5$, the pressure increase results in a decrease of s_L^0 . Lower values of the Zel'dovich number indicate a stronger reactivity. Higher H_2 contents lead to a lower Zel'dovich number: ammonia lessens the reactivity of the mixtures. Zel'dovich number decreases with increasing equivalence ratio indicating higher reactivity towards stoichiometry as captured by higher adiabatic temperatures. The similar Zel'dovich number at $\phi = 1.0$ for all fuel blends can explain the collapse of the peak growth rate observed Fig. 7. The higher pressure leads to a thinner flame thickness and a lower flame speed, leading to more instabilities. However, based on the δ_L^0 evolution with pressure, compared with the evolution of λ_c from Fig. 7 with pressure, we can conclude that the pressure effect on the flame thickness and flame speed is not the only reason for the instability increase (if it had been, the evolution for both quantities would have been proportional, which it is not the case here for both H_2 and NH_3/H_2). Therefore, there are two mechanisms due to pressure: the instabilities increase due to the thinner flame, but the domination of chain termination reaction and the increase of reactivity also leads to larger instabilities. Indeed, the Zel'dovich number increases as we shift towards high pressure for both the pure H_2 case and the 50% of NH_3 case. Increasing the Zel'dovich number for increasing pressure is found for H_2 and NH_3/H_2 flames due to chain termination reactions becoming more important at high pressure than chain branching reactions. The domination of chain termination reactions leads to a higher temperature at higher pressure, as seen in Table 1 and to a more reactive mixture. This was also found for pure methane by Attili et al. [51]. The fuel mixture does not strongly affect the expansion ratio at a given equivalence ratio, but a larger difference appears at stoichiometry. Indeed, as the equivalence ratio increases, H_2O formation increases, leading to a large difference in density between burned and unburned gases. And as the ammonia content increases in the fuel, NO formation increases, leading to a larger unbalance between burned and unburned gas

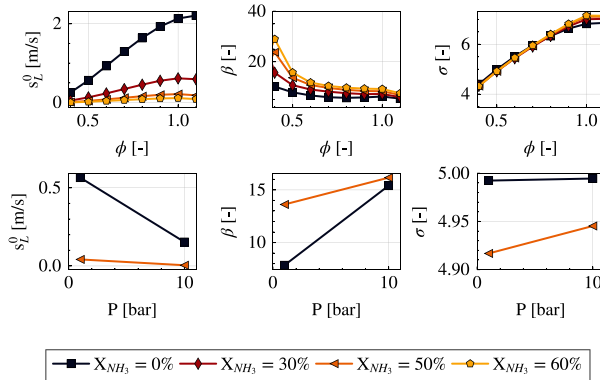


Fig. 10. Variation of laminar unstretched flame speed s_L^0 , Zel'dovich number β , and expansion ratio σ . Top: variation of equivalence ratio ϕ for different NH_3 fuel ratios. Bottom: Variation of initial pressure P for different NH_3 fuel ratios at equivalence ratio $\phi = 0.5$.

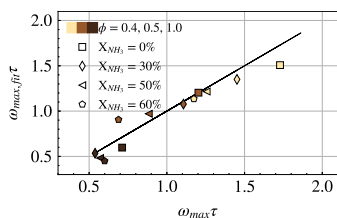


Fig. 11. Fit for $\omega_{max}\tau$ based on ϕ and X_{NH_3} .

densities. The influence of pressure on the expansion ratio is minimal.

Overall, ammonia addition in the fuel leads to a higher expansion ratio due to more products exacerbating the density difference between burned and unburned gases. Furthermore, ammonia addition reduces reactivity, reducing the Zel'dovich number. The dispersion relation and peak growth rate are impacted by these different parameters, as well as by the effective Lewis number, as they change with mixture composition, equivalence ratio, and pressure and impact the reactivity, hydrodynamic stability, and preferential diffusion.

3.5. Fit for $\omega_{max}\tau$ for atmospheric conditions

DNS data can be used to suggest a fit based on the mixture composition for atmospheric conditions to estimate the value of $\omega_{max}\tau$ for various NH_3/H_2 compositions at different equivalence ratios. This is similar to what Berger et al. [21] did for pure H_2 and Attili et al. [51] for CH_4 . Eq. (22) is derived from the observed DNS results to assess the impact of fuel content and equivalence ratio and can be used to estimate criterion for thermo-diffusive instabilities importance such as the ones suggested by Chomiak and Lipatnikov [57] and Chaudhuri et al. [58]. It can also be useful for modeling purposes to suggest such an empirical fit [21,50,59,60]. The fit is based on the composition ϕ and fuel content X_{NH_3} , and is suited only for atmospheric conditions:

$$\omega_{max,fit}\tau = \omega_{max,ref}\tau \left(\frac{\phi}{\phi_{ref}} \right)^a \left(\frac{(1 - X_{NH_3})}{(1 - X_{NH_3})_{ref}} \right)^b \quad (22)$$

with $a = -1.01$ and $b = 0.31$. Results (Fig. 11) show the fit's accuracy and indicate that an equivalence ratio increase will lead to a lower peak growth rate while an increase of X_{NH_3} will lead to a lower peak growth rate.

4. Conclusion

The dispersion relations of an extensive dataset of NH_3/H_2 /air premixed flames, with varying fuel ratios of hydrogen and ammonia, equivalence ratio, and pressure were numerically computed through high fidelity Direct Numerical Simulations. The dispersion relations were extracted from growth rate computation for varying initial wavelength perturbation. This allowed studying the effects of intrinsic instabilities on the flame front. The study leads to the following findings:

- Darrieus–Landau instabilities were found to dominate mixtures at stoichiometry, and the computed relation dispersion relation was equal to or below the Darrieus–Landau dispersion relation for all wave numbers: the thermo-diffusive mechanisms has no impact on the mixture. On the other hand, for leaner mixtures, the computed dispersion relation is above the Darrieus–Landau dispersion relation at small wave numbers: the thermo-diffusive mechanism has a positive impact on the mixture.

- An investigation of slightly strained flames has been performed to select a Lewis number definition that can be used in theoretical relations. We find the volume-based Lewis number (Le_V) to be best suited for NH_3/H_2 mixtures.
- Comparisons with theoretical dispersion relations showed the theory's difficulty in fitting the stabilizing effects at large wave numbers for lean mixtures. This indicates a need for new theoretical relations to capture lean flames behavior. This was known for pure hydrogen but is now extended to mixtures of ammonia and hydrogen.
- Within the investigated range of operating points, we use quantitative arguments to show that ammonia addition leads to more stable mixtures. The impact of ammonia dissociating into hydrogen and leading to an increase of instabilities has not been captured in this work, but it would be interesting to investigate a larger amount of operating conditions to see if, in some cases, ammonia addition might actually lead to more instability. However, the investigation of more operating conditions is outside of the scope of this study.
- Higher peak growth rates were computed for leaner mixtures, indicating that leaner flames are more unstable, even for NH_3/H_2 mixtures.
- A pressure increase resulted in a higher growth rate as chain termination reactions became more important for both NH_3/H_2 mixtures and pure H_2 .

Concluding, the present study contributes to the fundamental understanding of ammonia/hydrogen combustion and the development of thermo-diffusive effects. Furthermore, it provides unique correlations and datasets that could be used for modeling purposes following what is proposed for pure hydrogen-air flames by Berger et al. [21,59] and Aniello et al. [60].

Declaration of Competing Interest

The authors declare that they have no known competing financial interests or personal relationships that could have appeared to influence the work reported in this paper.

Acknowledgments

The Authors gratefully acknowledge the support from the Norwegian Research Council (296207) and related partners in the Low Emission Centre. This project has received funding from the European Research Council under the European Union's Horizon 2020 research and innovation program Grant Agreement 832248, SCIROCCO. The computations were performed on resources provided by Sigma2 - the National Infrastructure for High-Performance Computing and Data Storage in Norway (project nn9527k), on the BETZY supercomputer, and of GENCI-TGCC under grant agreement n° 2023-A0132B10157. CERFACS provided the software AVBP, and technical support for the software was provided by Dr. O. Vermorel and Dr. G. Staffelbach. Dr. A. Gruber is also acknowledged for providing computational resources and technical support. A. Coudray is acknowledged for the reduction of the kinetic mechanism used in this study. J.-J. Hok and N. Detomaso are also acknowledged for insightful discussion into the Markstein length definitions.

Supplementary material

Supplementary material associated with this article can be found, in the online version, at doi:10.1016/j.combustflame.2023.112986.

References

- [1] F.W. Taylor, The greenhouse effect and climate change revisited, *Rep. Prog. Phys.* 65 (2001) 1.
- [2] I. Staffell, D. Scamman, A. Velazquez Abad, P. Balcombe, P.E. Dodds, P. Ekins, N. Shah, K.R. Ward, The role of hydrogen and fuel cells in the global energy system, *Energy Environ. Sci.* 12 (2019) 463–491.
- [3] D.R. MacFarlane, P.V. Cherepanov, J. Choi, B.H. Suryanto, R.Y. Hodgetts, J.M. Bakker, F.M. Ferrero Vallana, A.N. Simonov, A roadmap to the ammonia economy, *Joule* 4 (2020) 1186–1205.
- [4] H. Kobayashi, A. Hayakawa, K. Somaratne, E. Okafor, Science and technology of ammonia combustion, *Proc. Combust. Inst.* 37 (2019) 109–133.
- [5] A. Valera-Medina, F. Amer-Hatem, A.K. Azad, I.C. Dedoussi, M. de Joannon, R.X. Fernandes, P. Glarborg, H. Hashemi, X. He, S. Mashruk, J. McGowan, C. Mounaim-Rousselle, A. Ortiz-Prado, A. Ortiz-Valera, I. Rossetti, B. Shu, M. Yehia, H. Xiao, M. Costa, Review on ammonia as a potential fuel: from synthesis to economics, *Energy Fuels* 35 (2021) 6964–7029.
- [6] H.G. Im, J.H. Chen, Preferential diffusion effects on the burning rate of interacting turbulent premixed hydrogen-air flames, *Combust. Flame* 131 (2002) 246–258.
- [7] H.C. Lee, P. Dai, M. Wan, A.N. Lipatnikov, Lewis number and preferential diffusion effects in lean hydrogen-air highly turbulent flames, *Phys. Fluids* 34 (2022) 035131.
- [8] P. Ahmed, B. Thorne, M. Lawes, S. Hochgreb, G.V. Nivarti, R.S. Cant, Three dimensional measurements of surface areas and burning velocities of turbulent spherical flames, *Combust. Flame* 233 (2021) 111586.
- [9] M.S. Wu, S. Kwon, J.F. Driscoll, G.M. Faeth, Turbulent premixed hydrogen/air flames at high Reynolds numbers, *Combust. Sci. Technol.* 73 (1990) 327–350.
- [10] L. Berger, A. Attili, H. Pitsch, Synergistic interactions of thermo-diffusive instabilities and turbulence in lean hydrogen flames, *Combust. Flame* 244 (2022) 112254.
- [11] A. Aspden, M. Day, J. Bell, Turbulence-chemistry interaction in lean premixed hydrogen combustion, *Proc. Combust. Inst.* 35 (2015) 1321–1329.
- [12] W. Song, F.E. Hernández-Pérez, H.G. Im, Diffusive effects of hydrogen on pressurized lean turbulent hydrogen-air premixed flames, *Combust. Flame* 246 (2022) 112423.
- [13] S. Wiseman, M. Rieth, A. Gruber, J.R. Dawson, J.H. Chen, A comparison of the blow-out behavior of turbulent premixed ammonia/hydrogen/nitrogen-air and methane-air flames, *Proc. Combust. Inst.* 38 (2021) 2869–2876.
- [14] V. Coulon, J. Gaucherand, V. Xing, D. Laera, C. Lapeyre, T. Poinso, Direct numerical simulations of methane, ammonia-hydrogen and hydrogen turbulent premixed flames, *Combust. Flame* 256 (2023) 112933.
- [15] M. Rieth, A. Gruber, F.A. Williams, J.H. Chen, Enhanced burning rates in hydrogen-enriched turbulent premixed flames by diffusion of molecular and atomic hydrogen, *Combust. Flame* 239 (2022) 111740.
- [16] M. Matalon, B.J. Matkowsky, Flames as gasdynamic discontinuities, *J. Fluid Mech.* 124 (1982) 239–259.
- [17] P. Pelce, P. Clavin, Influence of hydrodynamics and diffusion upon the stability limits of laminar premixed flames, *J. Fluid Mech.* 124 (1982) 219–237.
- [18] P. Clavin, J.C. Graña-Otero, Curved and stretched flames: the two Markstein numbers, *J. Fluid Mech.* 686 (2011) 187–217.
- [19] G.I. Sivashinsky, Instabilities, pattern formation, and turbulence in flames, *Annu. Rev. Fluid Mech.* 15 (1983) 179–199.
- [20] G.I. Sivashinsky, Diffusional-thermal theory of cellular flames, *Combust. Sci. Technol.* 15 (3–4) (1977) 137–145.
- [21] L. Berger, A. Attili, H. Pitsch, Intrinsic instabilities in premixed hydrogen flames: parametric variation of pressure, equivalence ratio, and temperature. Part 1 – dispersion relations in the linear regime, *Combust. Flame* 240 (2022) 111935.
- [22] C.E. Frouzakis, N. Fogla, A.G. Tomboulides, C. Altantzis, M. Matalon, Numerical study of unstable hydrogen/air flames: shape and propagation speed, *Proc. Combust. Inst.* 35 (2015) 1087–1095.
- [23] C. Altantzis, C. Frouzakis, A. Tomboulides, S. Kerkemeier, K. Boulouchos, Detailed numerical simulations of intrinsically unstable two-dimensional planar lean premixed hydrogen/air flames, *Proc. Combust. Inst.* 33 (2011) 1261–1268.
- [24] J. Yuan, Y. Ju, C.K. Law, On flame-front instability at elevated pressures, *Proc. Combust. Inst.* 31 (2007) 1267–1274.
- [25] J. Yu, R. Yu, X. Bai, M. Sun, J. Tan, Nonlinear evolution of 2D cellular lean hydrogen/air premixed flames with varying initial perturbations in the elevated pressure environment, *Int. J. Hydrog. Energy* 42 (2017) 3790–3803.
- [26] J. Lee, S. Lee, O. Kwon, Effects of ammonia substitution on hydrogen/air flame propagation and emissions, *Int. J. Hydrog. Energy* 35 (2010) 11332–11341.
- [27] Y. Li, M. Bi, B. Li, Y. Zhou, L. Huang, W. Gao, Explosion hazard evaluation of renewable hydrogen/ammonia/air fuels, *Energy* 159 (2018) 252–263.
- [28] A. Ichikawa, A. Hayakawa, Y. Kitagawa, K.K.A. Somaratne, T. Kudo, H. Kobayashi, Laminar burning velocity and Markstein length of ammonia/hydrogen/air premixed flames at elevated pressures, *Int. J. Hydrog. Energy* 40 (30) (2015) 9570–9578.
- [29] S. Zitouni, P. Brequigny, C. Mounaim-Rousselle, Influence of hydrogen and methane addition in laminar ammonia premixed flame on burning velocity, Lewis number and Markstein length, *Combust. Flame* 253 (2023) 112786.
- [30] G. Darrieus, Propagation d'un front de flamme, *Tech. Mod.* 30 (1938) 18.
- [31] L. Landau, On the theory of slow combustion, in: P. Pelcé (Ed.), *Dynamics of Curved Fronts*, Academic Press, San Diego (1988), pp. 403–411.
- [32] M. Matalon, C. Cui, J.K. Bechtold, Hydrodynamic theory of premixed flames: effects of stoichiometry, variable transport coefficients and arbitrary reaction orders, *J. Fluid Mech.* 487 (2003) 179–210.
- [33] C. Sun, C. Sung, L. He, C. Law, Dynamics of weakly stretched flames: quantitative description and extraction of global flame parameters, *Combust. Flame* 118 (1999) 108–128.
- [34] G. Sivashinsky, Nonlinear analysis of hydrodynamic instability in laminar flames—I. Derivation of basic equations, *Acta Astronaut.* 4 (11–12) (1977) 1177–1206.
- [35] A.Y. Klimenko, A.G. Class, On premixed flames as gasdynamic discontinuities: a simple approach to derive their propagation speed, *Combust. Sci. Technol.* 160 (2000) 23–33.
- [36] S. Chung, C. Law, An integral analysis of the structure and propagation of stretched premixed flames, *Combust. Flame* 72 (1988) 325–336.
- [37] A. Lipatnikov, J. Chomiak, Molecular transport effects on turbulent flame propagation and structure, *Prog. Energy Combust. Sci.* 31 (2005) 1–73.
- [38] G. Joulin, T. Mitani, Linear stability analysis of two-reactant flames, *Combust. Flame* 40 (1981) 235–246.
- [39] D. Lapalme, R. Lemaire, P. Seers, Assessment of the method for calculating the Lewis number of H₂/CO/CH₄ mixtures and comparison with experimental results, *Int. J. Hydrog. Energy* 42 (2017) 8314–8328.
- [40] N. Bouvet, F. Halter, C. Chauveau, Y. Yoon, On the effective Lewis number formulations for lean hydrogen/hydrocarbon/air mixtures, *Int. J. Hydrog. Energy* 38 (2013) 5949–5960.
- [41] S. Muppala, M. Nakahara, N. Aluri, H. Kido, J. Wen, M. Papalexandris, Experimental and analytical investigation of the turbulent burning velocity of two-component fuel mixtures of hydrogen, methane and propane, *Int. J. Hydrog. Energy* 34 (2009) 9258–9265.
- [42] F. Dinkelacker, B. Manickam, S. Muppala, Modelling and simulation of lean premixed turbulent methane/hydrogen/air flames with an effective Lewis number approach, *Combust. Flame* 158 (2011) 1742–1749.
- [43] C. Law, G. Jomaas, J. Bechtold, Cellular instabilities of expanding hydrogen/propane spherical flames at elevated pressures: theory and experiment, *Proc. Combust. Inst.* 30 (2005) 159–167.
- [44] T. Schönfeld, M. Rudgyard, Steady and unsteady flow simulations using the hybrid flow solver AVBP, *AIAA J.* 37 (1999) 1378–1385.
- [45] A. Stagni, C. Cavallotti, S. Arunthanayothin, Y. Song, O. Herbinet, F. Battin-Leclerc, T. Faravelli, A. Experimental, theoretical and kinetic-modeling study of the gas-phase oxidation of ammonia, *React. Chem. Eng.* 5 (2020) 696–711.
- [46] Q. Cazères, P. Peipiot, E. Riber, B. Cuenot, A fully automatic procedure for the analytical reduction of chemical kinetics mechanisms for computational fluid dynamics applications, *Fuel* 303 (2021) 121247.
- [47] P. Lax, B. Wendroff, Systems of conservation laws, *Commun. Pure Appl. Math.* 13 (1960) 217–237.
- [48] D.G. Goodwin, H.K. Moffat, J. Schoegl, R.L. Speth, B.W. Weber, Cantera: an object-oriented software toolkit for chemical kinetics, thermo-dynamics, and transport processes, 2022. Version 2.6.0.
- [49] T. Poinso, S. Lele, Boundary conditions for direct simulations of compressible viscous flows, *J. Comput. Phys.* 101 (1992) 104–129.
- [50] T. Howarth, A. Aspden, An empirical characteristic scaling model for freely-propagating lean premixed hydrogen flames, *Combust. Flame* 237 (2022) 111805.
- [51] A. Attili, R. Lamioni, L. Berger, K. Kleinheinz, P.E. Lapenna, H. Pitsch, F. Creta, The effect of pressure on the hydrodynamic stability limit of premixed flames, *Proc. Combust. Inst.* 38 (2021) 1973–1981.
- [52] G.H. Markstein, *Nonsteady Flame Propagation*: AGARDograph, Elsevier, 2014.
- [53] J. Buckmaster, D. Mikolaitis, The premixed flame in a counterflow, *Combust. Flame* 47 (1982) 191–204.
- [54] T. Poinso, D. Veynante, *Theoretical and Numerical Combustion*, Edwards, 2005.
- [55] J. Bechtold, M. Matalon, The dependence of the Markstein length on stoichiometry, *Combust. Flame* 127 (1) (2001) 1906–1913.
- [56] P. Clavin, G. Joulin, Premixed flames in large scale and high intensity turbulent flow, *J. Phys. Lett.* 44 (1) (1983).
- [57] J. Chomiak, A.N. Lipatnikov, Simple criterion of importance of laminar flame instabilities in premixed turbulent combustion of mixtures characterized by low Lewis numbers, *Phys. Rev. E* 107 (2023) 015102.
- [58] S. Chaudhuri, V. Akkerman, C.K. Law, Spectral formulation of turbulent flame speed with consideration of hydrodynamic instability, *Phys. Rev. E* 84 (2011) 026322.
- [59] L. Berger, A. Attili, H. Pitsch, Intrinsic instabilities in premixed hydrogen flames: parametric variation of pressure, equivalence ratio, and temperature. Part 2 – non-linear regime and flame speed enhancement, *Combust. Flame* 240 (2022) 111936.
- [60] A. Aniello, D. Laera, L. Berger, A. Attili, T. Poinso, Introducing thermo-diffusive effects in large-eddy simulation of turbulent combustion for lean hydrogen-air flames, *Proceedings of the 2022 Summer Program* (2022).

Intrinsic instabilities of hydrogen and hydrogen/ammonia premixed flames: influence of equivalence ratio, fuel composition and pressure. - Supplementary material

Jessica Gaucherand^{a,b,*}, Davide Laera^{a,c}, Corinna Schulze-Netzer^b, Thierry Poinso^{a,d}

^a*CERFACS, 42 avenue Gaspard Coriolis, 31057 Toulouse, France*

^b*Department of Energy and Process Engineering, Norwegian University of Science and Technology, NO-7034 Trondheim, Norway*

^c*Department of Mechanics, Mathematics and Management, Polytechnic University of Bari, Via Orabona 4, 70125 Bari, Italy*

^d*IMFT, Allée du Professeur Camille Soula, 31400 Toulouse, France*

A. Validation of ammonia hydrogen reduced scheme (ARC)

The Analytically Reduced Chemistry (ARC) used in this study was derived to achieve an accurate description of the combustion process of premixed ammonia/hydrogen-air flames. The reduction was carried out with the ARCANE code co-developed by CERFACS and Cornell University [1]. It is a fully automatic multi-step reduction tool relying on DRGEP [2], chemical lumping [3] and Quasi-Steady State assumption [4].

The CRECK [5] C1 - C3 scheme, for which carbon related species are removed, was chosen as the detailed reference mechanism. This scheme comprises 31 species and 203 reactions.

The reduced ARC mechanism generated by ARCANE comprises 18 transported species and 6 species in Quasi-Steady State:

- The transported species are N_2 , H_2 , H , O_2 , O , H_2O , OH , H_2O_2 , HO_2 , NO , N_2O , NO_2 , $HONO$, N_2H_2 , NH_3 , N_2H_4 , NH , NH_2 .
- The Quasi-Steady State species are HNO , H_2NN , N , NNH , H_2NO , N_2H_3 .

Prandtl number of all species is equal to 0.643. Species Schmidt number are listed here after in the same order as the transported species: The mixture used to com-

*Corresponding author:

Email address: gaucherand@cerfacs.fr (Jessica Gaucherand)

S_{c_E}
0.8026
0.2012
0.1324
0.7905
0.4879
0.7185
0.4972
0.7007
0.7649
0.7742
0.1022
0.9151
0.9188
0.7785
0.6907
1.0429
0.4631
0.4751

Table A.1: Schmidt number of the species.

pute the Prandtl and Schmidt of this study is selected based on an optimization where the Lewis number for a range of equivalence ratio and hydrogen content have been tested and the Lewis number most optimized to represent the range of mixture investigated is selected for the rest of the study. Both Lewis numbers in the burned and fresh gases are tested to perform this optimization. Here the Lewis number Le_F and Le_O most representative of the range investigated and kept hereafter is at 300K for the mixture 50% NH_3 and ϕ 0.6 in the burned gases.

The impact of transport assumptions is evaluated hereafter, where, for the reference case of pure H_2 and $\phi = 0.5$, we compare two one-dimensional laminar flames, one with constant, non-unity, Lewis number assumption and the other with varying Lewis number assumptions, we compare the temperature and flame speed.

We find a good agreement between the temperatures and a slight underprediction in the constant Lewis case in the burned gases. The relative error in the burned gases is still very low with a 6 % error.

A detailed description of the reactions is given in Tab. A.2.

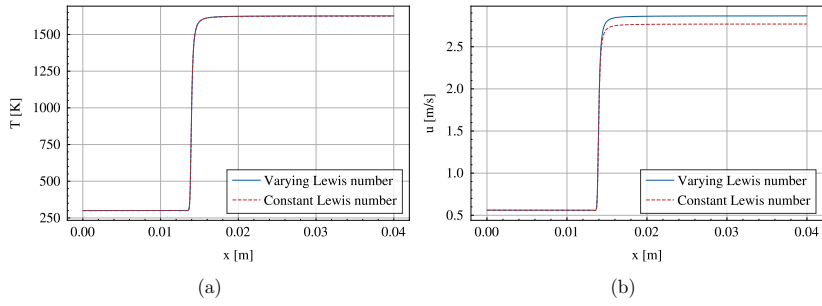


Figure A.1: Comparison between constant and varying Lewis number in one-dimensional flame.

Table A.2: List of reactions with A the pre-exponential factor in $\text{m}^{3(n-1)}/\text{kmol}^{n-1}/\text{s}$ with n the order of the reaction, b the temperature exponent and E_a the activation energy in J/kmol . In the case of fall-off reactions, two sets of Arrhenius coefficients are specified, the first one being the low-temperature set and the second one the high-temperature set.

No.	Reaction	A	b	E_a
1	$\text{H}_2 + \text{M} \leftrightarrow 2 \text{H} + \text{M}$	4.577000E+16	-1.400000E+00	4.368096E+08
2	$\text{H}_2:2.50\text{E}+00 \text{H}_2\text{O}:1.20\text{E}+01$	5.080000E+01	2.670000E+00	2.632573E+07
3	$\text{H}_2 + \text{O} \leftrightarrow \text{H} + \text{OH}$	4.380000E+10	0.000000E+00	2.924616E+07
4	$\text{H}_2 + \text{OH} \leftrightarrow \text{H} + \text{H}_2\text{O}$	6.165000E+09	-5.000000E-01	0.000000E+00
	$2 \text{O} + \text{M} \leftrightarrow \text{O}_2 + \text{M}$			
	$\text{H}_2:2.50\text{E}+00 \text{H}_2\text{O}:1.20\text{E}+01$			
5	$\text{H} + \text{O}_2 \leftrightarrow \text{O} + \text{OH}$	1.140000E+11	0.000000E+00	6.395662E+07
6	$\text{H} + \text{OH} + \text{M} \leftrightarrow \text{H}_2\text{O} + \text{M}$	3.500000E+16	-2.000000E+00	0.000000E+00
	$\text{H}_2:7.30\text{E}-01 \text{H}_2\text{O}:3.65\text{E}+00$			
7	$\text{H}_2\text{O} + \text{O} \leftrightarrow 2 \text{OH}$	6.700000E+04	1.704000E+00	6.270477E+07
8	$\text{H} + \text{O} + \text{M} \leftrightarrow \text{OH} + \text{M}$	4.714000E+12	-1.000000E+00	0.000000E+00
	$\text{H}_2:2.50\text{E}+00 \text{H}_2\text{O}:1.20\text{E}+01$			
9	$\text{H}_2\text{O}_2 (+\text{M}) \leftrightarrow 2 \text{OH} (+\text{M})$	2.490000E+21	-2.300000E+00	2.039658E+08
		2.000000E+12	9.000000E-01	2.039658E+08
	$\text{H}_2:3.70\text{E}+00 \text{H}_2\text{O}:7.65\text{E}+00 \text{H}_2\text{O}_2:7.70\text{E}+00 \text{N}_2:1.50\text{E}+00 \text{O}_2:1.20\text{E}+00$			
10	$\text{H} + \text{H}_2\text{O}_2 \leftrightarrow \text{H}_2\text{O} + \text{OH}$	2.410000E+10	0.000000E+00	1.661048E+07
11	$\text{H} + \text{H}_2\text{O}_2 \leftrightarrow \text{H}_2 + \text{HO}_2$	2.150000E+07	1.000000E+00	2.510400E+07
12	$\text{H}_2\text{O}_2 + \text{O} \leftrightarrow \text{HO}_2 + \text{OH}$	9.550000E+03	2.000000E+00	1.661048E+07
13	$\text{H}_2\text{O}_2 + \text{OH} \leftrightarrow \text{H}_2\text{O} + \text{HO}_2$	1.740000E+09	0.000000E+00	1.330512E+06
14	$\text{H}_2\text{O}_2 + \text{OH} \leftrightarrow \text{H}_2\text{O} + \text{HO}_2$	7.590000E+10	0.000000E+00	3.041350E+07
15	$\text{H} + \text{HO}_2 \leftrightarrow 2 \text{OH}$	7.079000E+10	0.000000E+00	1.234280E+06
16	$\text{H} + \text{HO}_2 \leftrightarrow \text{H}_2 + \text{O}_2$	1.140200E+07	1.082700E+00	2.317016E+06
17	$\text{HO}_2 + \text{O} \leftrightarrow \text{O}_2 + \text{OH}$	3.250000E+10	0.000000E+00	0.000000E+00
18	$\text{HO}_2 + \text{OH} \leftrightarrow \text{H}_2\text{O} + \text{O}_2$	7.000000E+09	0.000000E+00	-4.572945E+06
19	$\text{HO}_2 + \text{OH} \leftrightarrow \text{H}_2\text{O} + \text{O}_2$	4.500000E+11	0.000000E+00	4.572945E+07
20	$2 \text{HO}_2 \leftrightarrow \text{H}_2\text{O}_2 + \text{O}_2$	1.000000E+11	0.000000E+00	4.619504E+07
21	$2 \text{HO}_2 \leftrightarrow \text{H}_2\text{O}_2 + \text{O}_2$	1.900000E+08	0.000000E+00	-5.894942E+06
22	$\text{H} + \text{O}_2 (+\text{M}) \leftrightarrow \text{HO}_2 (+\text{M})$	1.737000E+13	-1.230000E+00	0.000000E+00
		4.650000E+09	4.400000E-01	0.000000E+00
	$\text{H}_2:1.30\text{E}+00 \text{H}_2\text{O}:1.00\text{E}+01$			
23	$\text{O} + \text{OH} + \text{M} \leftrightarrow \text{HO}_2 + \text{M}$	1.000000E+10	0.000000E+00	0.000000E+00
24	$\text{NH}_3 \leftrightarrow \text{H} + \text{NH}_2$	3.497000E+30	-5.224000E+00	4.651072E+08
25	$\text{H} + \text{NH}_2 \leftrightarrow \text{H}_2 + \text{NH}$	4.000000E+10	0.000000E+00	1.527160E+07

No.	Reaction	A	b	E_a
26	H + NH3 \leftrightarrow H2 + NH2	1.963000E+01	2.854000E+00	3.564852E+07
27	NH3 + OH \leftrightarrow H2O + NH2	1.559000E+02	2.372000E+00	4.974776E+05
28	NH3 + O \leftrightarrow NH2 + OH	4.430000E-01	3.180000E+00	2.819974E+07
29	HO2 + NH3 \leftrightarrow H2O2 + NH2	1.173000E-03	3.839000E+00	7.221584E+07
30	NH3 + O2 \leftrightarrow HO2 + NH2	1.415000E+07	1.285000E+00	2.310572E+08
31	NH2 + O \leftrightarrow H + HNO	1.500000E+12	-5.470000E-01	3.500753E+06
32	NH2 + O \leftrightarrow H + HNO	7.730000E+10	-2.770000E-01	2.704538E+06
33	NH2 + O \leftrightarrow NH + OH	7.000000E+09	0.000000E+00	0.000000E+00
34	NH2 + O \leftrightarrow NH + OH	3.300000E+05	1.500000E+00	2.124133E+07
35	NH2 + OH \leftrightarrow H2O + NH	9.600000E+03	1.970000E+00	2.803280E+06
36	NH2 + O2 \leftrightarrow HNO + OH	2.900000E-05	3.764000E+00	7.608604E+07
37	NH2 + O2 \leftrightarrow H2NO + O	2.600000E+08	4.870000E-01	1.215452E+08
38	HO2 + NH2 \leftrightarrow H2NO + OH	1.566000E+10	0.000000E+00	0.000000E+00
39	NH + NH2 \leftrightarrow H + N2H2	1.500000E+12	-5.000000E-01	0.000000E+00
40	NH + NH2 \leftrightarrow N + NH3	9.600000E+00	2.460000E+00	4.476880E+05
41	2 NH \leftrightarrow N + NH2	5.700000E-04	3.880000E+00	1.430928E+06
42	2 NH \rightarrow H2 + N2	6.260000E+09	-3.600000E-02	-6.732056E+05
43	2 NH \rightarrow 2 H + N2	5.634000E+10	-3.600000E-02	-6.732056E+05
44	2 NH2 \leftrightarrow NH + NH3	5.640000E-03	3.530000E+00	2.301200E+06
45	2 NH2 \leftrightarrow N2H4	5.600000E+45	-1.130000E+01	4.971554E+07
46	2 NH2 \leftrightarrow H + N2H3	1.200000E+09	-3.000000E-02	4.219146E+07
47	2 NH2 \leftrightarrow H2 + H2NN	1.200000E+18	-3.080000E+00	1.409171E+07
48	NH2 + NO2 \leftrightarrow H2NO + NO	8.600000E+08	1.100000E-01	-4.962224E+06
49	NH2 + NO2 \leftrightarrow H2O + N2O	2.200000E+08	1.100000E-01	-4.962224E+06
50	NH2 + NO \leftrightarrow H2O + N2	2.600000E+16	-2.369000E+00	3.640080E+06
51	NH2 + NO \leftrightarrow NNH + OH	4.300000E+07	2.940000E-01	-3.623344E+06
52	H + NH \leftrightarrow H2 + N	3.010000E+10	0.000000E+00	0.000000E+00
53	NH + O \leftrightarrow H + NO	3.000000E+10	0.000000E+00	0.000000E+00
54	NH + OH \leftrightarrow H + HNO	2.000000E+10	0.000000E+00	0.000000E+00
55	NH + OH \leftrightarrow H2O + N	2.000000E+06	1.200000E+00	0.000000E+00
56	NH + O2 \leftrightarrow HNO + O	4.050000E+08	9.000000E-02	4.464328E+07
57	NH + O2 \leftrightarrow NO + OH	2.010000E+12	-1.380000E+00	2.372328E+07
58	N + NH \leftrightarrow H + N2	6.410000E+08	5.100000E-01	8.368000E+04
59	NH + NO \leftrightarrow H + N2O	5.328000E+09	2.600000E-02	-1.210808E+07
60	NH + NO \leftrightarrow N2 + OH	3.635000E+07	3.610000E-01	-1.190055E+07
61	NH + NO2 \leftrightarrow N2O + OH	4.100000E+09	0.000000E+00	0.000000E+00

No.	Reaction	A	b	E_a
62	NH + NO2 \leftrightarrow HNO + NO	5.900000E+09	0.000000E+00	0.000000E+00
63	N + OH \leftrightarrow H + NO	2.830000E+10	0.000000E+00	0.000000E+00
64	N + O2 \leftrightarrow NO + O	9.027000E+06	1.000000E+00	2.719600E+07
65	N + NO \leftrightarrow N2 + O	4.280000E+10	0.000000E+00	6.568880E+06
66	N2H4 \leftrightarrow H2 + H2NN	5.300000E+39	-8.350000E+00	2.899788E+08
67	H + N2H4 \leftrightarrow H2 + N2H3	9.600000E+05	1.500000E+00	2.024345E+07
68	N2H4 + O \leftrightarrow N2H3 + OH	6.700000E+05	1.500000E+00	1.192984E+07
69	N2H4 + O \leftrightarrow H2O + N2H2	8.490000E+10	0.000000E+00	5.020800E+06
70	N2H4 + OH \leftrightarrow H2O + N2H3	1.300000E+10	0.000000E+00	-1.330512E+06
71	N2H4 + NH2 \leftrightarrow N2H3 + NH3	3.700000E+03	1.940000E+00	6.819920E+06
72	N2H4 + NO2 \leftrightarrow HONO + N2H3	8.200000E-02	3.130000E+00	3.707024E+07
73	N2H3 \leftrightarrow H + N2H2	3.600000E+47	-1.038000E+01	2.885864E+08
74	H + N2H3 \leftrightarrow H2 + N2H2	2.400000E+05	1.500000E+00	0.000000E+00
75	N2H3 + O \leftrightarrow HNO + NH2	3.000000E+10	0.000000E+00	0.000000E+00
76	N2H3 + O \leftrightarrow N2H2 + OH	1.700000E+05	1.500000E+00	-2.700772E+06
77	N2H3 + OH \leftrightarrow H2O + N2H2	1.200000E+03	2.000000E+00	-4.985654E+06
78	N2H3 + OH \leftrightarrow H2NN + H2O	3.000000E+10	0.000000E+00	0.000000E+00
79	N2H3 + NH2 \leftrightarrow N2H2 + NH3	9.200000E+02	1.940000E+00	-4.822060E+06
80	N2H3 + NH2 \leftrightarrow H2NN + NH3	3.000000E+10	0.000000E+00	0.000000E+00
81	HO2 + N2H3 \leftrightarrow H2O2 + N2H2	1.400000E+01	2.690000E+00	-6.692308E+06
82	HO2 + N2H3 \leftrightarrow N2H4 + O2	9.200000E+02	1.940000E+00	8.895602E+06
83	N2H2 \leftrightarrow H + NNH	1.800000E+40	-8.410000E+00	3.069090E+08
84	N2H2 \leftrightarrow H + NNH	2.600000E+40	-8.530000E+00	3.049559E+08
85	H + N2H2 \leftrightarrow H2 + NNH	4.121000E+06	1.289000E+00	-9.376344E+05
86	N2H2 + O \leftrightarrow NNH + OH	3.300000E+05	1.500000E+00	2.077356E+06
87	N2H2 + OH \leftrightarrow H2O + NNH	5.923000E-02	3.400000E+00	-5.705721E+06
88	N2H2 + NO \leftrightarrow N2O + NH2	4.000000E+09	0.000000E+00	4.985654E+07
89	N2H2 + NH \leftrightarrow NH2 + NNH	2.400000E+03	2.000000E+00	-4.985654E+06
90	N2H2 + NH2 \leftrightarrow NH3 + NNH	8.800000E-05	4.050000E+00	-6.736240E+06
91	N2H2 \leftrightarrow H2NN	2.000000E+41	-9.380000E+00	2.864040E+08
92	H2NN \leftrightarrow H + NNH	9.600000E+35	-7.570000E+00	2.294556E+08
93	H2NN \leftrightarrow H + NNH	3.200000E+31	-6.220000E+00	2.188973E+08
94	H2NN + O2 \leftrightarrow NH2 + NO2	1.500000E+09	0.000000E+00	2.494082E+07
95	H + H2NN \leftrightarrow H + N2H2	1.800000E+07	9.700000E-01	1.870583E+07
96	H + H2NN \leftrightarrow H2 + NNH	4.800000E+05	1.500000E+00	-3.741333E+06
97	H2NN + O \leftrightarrow NH2 + NO	3.200000E+06	1.030000E+00	1.130642E+07

No.	Reaction	A	b	E_a
98	$\text{H2NN} + \text{O} \leftrightarrow \text{NNH} + \text{OH}$	3.300000E+05	1.500000E+00	-3.741333E+06
99	$\text{H2NN} + \text{OH} \leftrightarrow \text{H2O} + \text{NNH}$	2.400000E+03	2.000000E+00	-4.988165E+06
100	$\text{H2NN} + \text{NH2} \leftrightarrow \text{NH3} + \text{NNH}$	1.800000E+03	1.940000E+00	-4.822060E+06
101	$\text{H2NN} + \text{HO2} \leftrightarrow \text{H2O2} + \text{NNH}$	2.900000E+01	2.690000E+00	-6.692308E+06
102	$\text{NNH} \leftrightarrow \text{H} + \text{N2}$	1.000000E+09	0.000000E+00	0.000000E+00
103	$\text{H} + \text{NNH} \leftrightarrow \text{H2} + \text{N2}$	2.400000E+05	1.500000E+00	-3.739241E+06
104	$\text{NNH} + \text{O} \leftrightarrow \text{H} + \text{N2O}$	1.900000E+11	-2.740000E-01	-9.204800E+04
105	$\text{NNH} + \text{O} \leftrightarrow \text{NH} + \text{NO}$	5.200000E+08	3.880000E-01	-1.711256E+06
106	$\text{NNH} + \text{O} \leftrightarrow \text{N2} + \text{OH}$	1.200000E+10	1.450000E-01	-9.079280E+05
107	$\text{NNH} + \text{OH} \leftrightarrow \text{H2O} + \text{N2}$	5.000000E+10	0.000000E+00	0.000000E+00
108	$\text{NNH} + \text{O2} \leftrightarrow \text{HO2} + \text{N2}$	5.600000E+11	-3.850000E-01	-5.439200E+04
109	$\text{NH2} + \text{NNH} \leftrightarrow \text{N2} + \text{NH3}$	9.200000E+02	1.940000E+00	-4.819550E+06
110	$\text{HO2} + \text{NNH} \leftrightarrow \text{H2O2} + \text{N2}$	1.400000E+01	2.690000E+00	-6.692308E+06
111	$\text{NNH} + \text{NO} \leftrightarrow \text{HNO} + \text{N2}$	5.000000E+10	0.000000E+00	0.000000E+00
112	$\text{HO2} + \text{NO} \leftrightarrow \text{NO2} + \text{OH}$	2.110000E+09	0.000000E+00	-2.008320E+06
113	$\text{NO} + \text{O} (+\text{M}) \leftrightarrow \text{NO2} (+\text{M})$	4.720000E+18	-2.870000E+00	6.485200E+06
		1.300000E+12	-7.500000E-01	0.000000E+00
	$\text{H2O:1.00E+01 N2:1.70E+00 O2:1.50E+00}$			
114	$\text{NO} + \text{OH} \leftrightarrow \text{HONO}$	3.090000E+20	-4.170000E+00	6.782264E+06
115	$\text{HNO} \leftrightarrow \text{H} + \text{NO}$	1.825900E+20	-3.008000E+00	2.003299E+08
116	$\text{H} + \text{HNO} \leftrightarrow \text{H2} + \text{NO}$	9.680000E+08	6.200000E-01	1.506240E+06
117	$\text{HNO} + \text{O} \leftrightarrow \text{NO} + \text{OH}$	2.290000E+10	0.000000E+00	0.000000E+00
118	$\text{HNO} + \text{OH} \leftrightarrow \text{H} + \text{HONO}$	1.480000E+00	2.720000E+00	1.905394E+07
119	$\text{HNO} + \text{OH} \leftrightarrow \text{H2O} + \text{NO}$	6.300000E+07	3.900000E-01	1.582389E+07
120	$\text{HNO} + \text{O2} \leftrightarrow \text{HO2} + \text{NO}$	2.000000E+10	0.000000E+00	6.232486E+07
121	$\text{HNO} + \text{NH2} \leftrightarrow \text{NH3} + \text{NO}$	3.670000E+04	1.630000E+00	-5.230000E+06
122	$\text{HNO} + \text{NO} \leftrightarrow \text{N2O} + \text{OH}$	8.510000E+09	0.000000E+00	1.238882E+08
123	$\text{HNO} + \text{NO2} \leftrightarrow \text{HONO} + \text{NO}$	4.420000E+01	2.640000E+00	1.691005E+07
124	$\text{H} + \text{HONO} \leftrightarrow \text{H2} + \text{NO2}$	1.890000E+00	2.830000E+00	5.952577E+06
125	$\text{H} + \text{HONO} \leftrightarrow \text{H2O} + \text{NO}$	4.300000E+06	9.800000E-01	1.702888E+07
126	$\text{HONO} + \text{O} \leftrightarrow \text{NO2} + \text{OH}$	1.210000E+10	0.000000E+00	2.493664E+07
127	$\text{HONO} + \text{OH} \leftrightarrow \text{H2O} + \text{NO2}$	1.700000E+09	0.000000E+00	-2.175680E+06
128	$\text{HONO} + \text{NH} \leftrightarrow \text{NH2} + \text{NO2}$	1.000000E+10	0.000000E+00	0.000000E+00
129	$\text{HONO} + \text{NH2} \leftrightarrow \text{NH3} + \text{NO2}$	3.170000E-01	2.830000E+00	-1.493688E+07
130	$2 \text{HONO} \rightarrow \text{H2O} + \text{NO} + \text{NO2}$	3.490000E-04	3.640000E+00	5.078790E+07
131	$\text{H2NO} + \text{M} \leftrightarrow \text{H} + \text{HNO} + \text{M}$	2.800000E+21	-2.830000E+00	2.718550E+08

No.	Reaction	A	b	E_a
132	H + H2NO \leftrightarrow H2 + HNO	4.800000E+05	1.500000E+00	6.526203E+06
133	H + H2NO \leftrightarrow NH2 + OH	4.000000E+10	0.000000E+00	0.000000E+00
134	H2NO + O \leftrightarrow HNO + OH	3.300000E+05	1.500000E+00	2.036771E+06
135	H2NO + OH \leftrightarrow H2O + HNO	2.400000E+03	2.000000E+00	4.988165E+06
136	H2NO + NO2 \leftrightarrow HNO + HONO	6.000000E+08	0.000000E+00	8.368000E+06
137	H2NO + NH2 \leftrightarrow HNO + NH3	1.800000E+03	1.940000E+00	-2.426720E+06
138	H2NO + O2 \leftrightarrow HNO + HO2	2.300000E-01	2.994000E+00	6.903600E+07
139	H2NO + HO2 \leftrightarrow H2O2 + HNO	3.360000E+02	2.000000E+00	-5.999856E+06
140	H + NO2 \leftrightarrow NO + OH	8.850000E+10	0.000000E+00	0.000000E+00
141	NO2 + O \leftrightarrow NO + O2	3.920000E+09	0.000000E+00	-9.957920E+05
142	HO2 + NO2 \leftrightarrow HONO + O2	1.900000E-03	3.320000E+00	1.273610E+07
143	2 NO2 \rightarrow 2 NO + O2	1.630000E+09	0.000000E+00	1.089095E+08
144	N2O (+M) \leftrightarrow N2 + O (+M)	6.020000E+11	0.000000E+00	2.403457E+08
		9.900000E+10	0.000000E+00	2.422578E+08
	H2O:1.20E+01 N2:1.70E+00 O2:1.40E+00			
145	H + N2O \leftrightarrow N2 + OH	2.530000E+07	0.000000E+00	1.903720E+07
146	H + N2O \leftrightarrow N2 + OH	5.000000E+11	0.000000E+00	7.573040E+07
147	N2O + O \leftrightarrow 2 NO	6.620000E+10	0.000000E+00	1.114199E+08
148	N2O + O \leftrightarrow N2 + O2	1.020000E+11	0.000000E+00	1.172357E+08
149	N2O + OH \leftrightarrow HO2 + N2	1.000000E-05	4.720000E+00	1.529670E+08
150	N2O + NO \leftrightarrow N2 + NO2	5.250000E+02	2.230000E+00	1.937192E+08

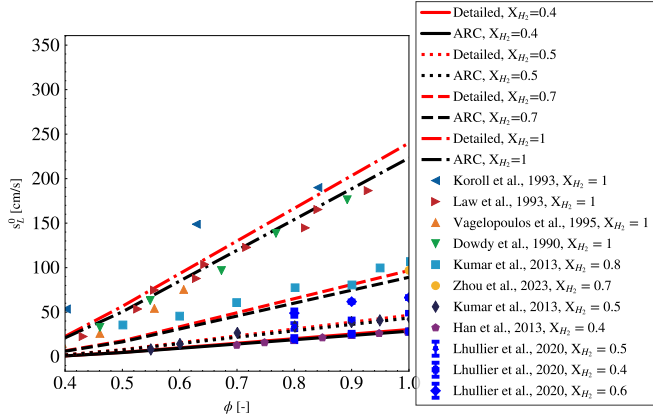


Figure A.2: Reduced scheme validation for the NH_3/H_2 mixtures. Numerical data from CRECK [5] (detailed), and ARC against experiment from Koroll et al. [6], Law et al. [7], Vagelopoulos et al. [8], Dowdy et al. [9], Kumar et al. [10], Zhou et al. [11], Han et al. [12], and Lhuillier et al. [13].

B. Theoretical dispersion relations introduced in Section 2 are compared with the computed dispersion relation for equivalence ratio $\phi = 0.4$, 0.5 and 1 for all mixtures.

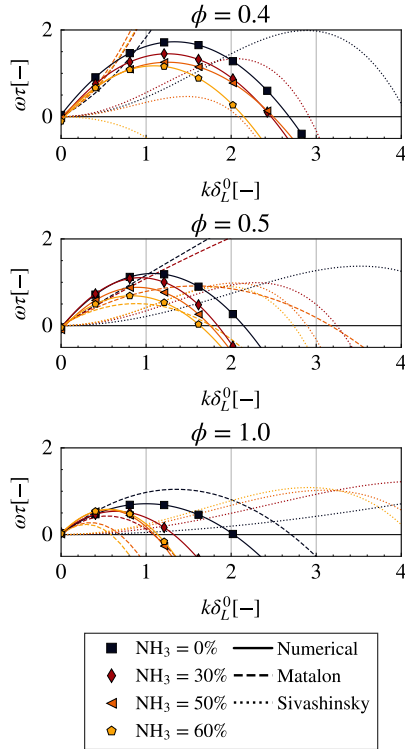


Figure B.1: Computed dispersion relation (solid line with symbol) compared with theoretical dispersion relation using volume-based definition of the Lewis number: Matalon's dispersion relation (dashed line) and Sivashinsky's relation (dotted line). ω_{DL} is not pictured. Case $\phi = 0.4$, 0.5 and 1 for 0 % NH_3 , 30 % NH_3 , 50 % NH_3 and 60 % NH_3 .

C. Activation energy

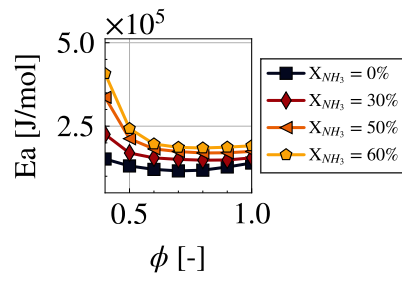


Figure C.1: Variation of activation energy with equivalence ratio ϕ for different NH_3 fuel ratios.

D. Lewis number

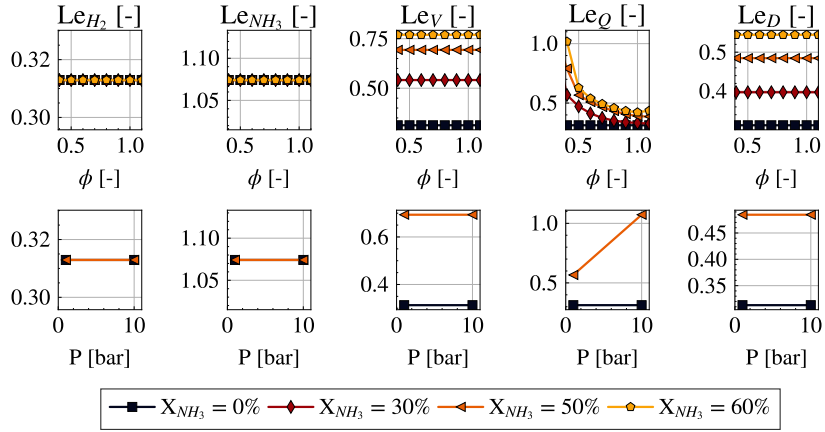


Figure D.1: Variation of Lewis number based on different fuel Lewis number definition: from left to right: H_2 , NH_3 , Q , V and D as defined Section 2. Top: variation of equivalence ratio ϕ for different NH_3 fuel ratios. Bottom: variation of initial pressure P for different NH_3 fuel ratios at equivalence ratio $\phi = 0.5$.

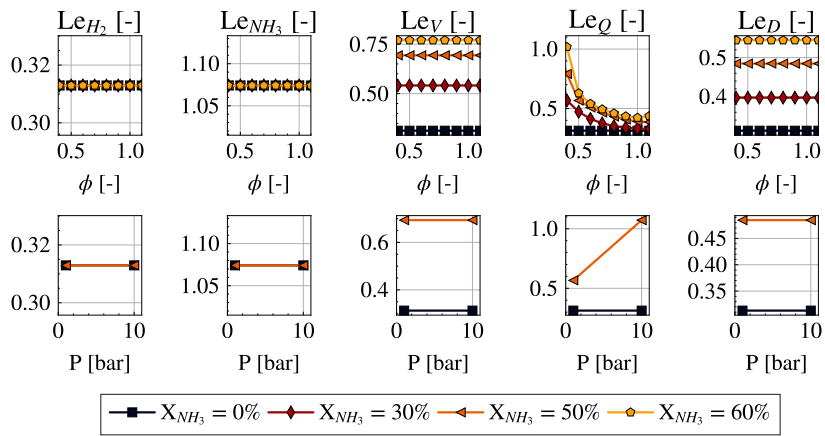


Figure D.2: Variation of effective Lewis number based on different fuel Lewis number definition: from left to right: H_2 , NH_3 , Q , V and D as defined Section 2. Top: variation of equivalence ratio ϕ for different NH_3 fuel ratios. Bottom: variation of initial pressure P for different NH_3 fuel ratios at equivalence ratio $\phi = 0.5$.

References

- [1] Q. Cazères, P. Pepiot, ARCANE, a new python-based chemistry reduction code, <https://chemistry.cerfacs.fr/en/arcane/> (2019).
- [2] P. Pepiot-Desjardins, H. Pitsch, An efficient error-propagation-based reduction method for large chemical kinetic mechanisms, *Combust. Flame* 154 (2008) 67–81.
- [3] P. Pepiot-Desjardins, H. Pitsch, An automatic chemical lumping method for the reduction of large chemical kinetic mechanisms, *Combust. Theory Model.* 12 (2008) 1089–1108.
- [4] T. Løvås, F. Mauss, C. Hasse, N. Peters, Development of adaptive kinetics for application in combustion systems, *Proc. Combust. Inst.* 29 (2002) 1403–1410.
- [5] A. Stagni, C. Cavallotti, S. Arunthanayothin, Y. Song, O. Herbinet, F. Battin-Leclerc, T. Faravelli, An experimental, theoretical and kinetic-modeling study of the gas-phase oxidation of ammonia, *React. Chem. Eng.* 5 (2020) 696–711.
- [6] G. Koroll, R. Kumar, E. Bowles, Burning velocities of hydrogen-air mixtures, *Combust. Flame* 94 (1993) 330–340.
- [7] C. K. Law, in *Reduced Kinetic Mechanisms for Applications in Combustion Systems*, Springer Berlin Heidelberg, 1993.
- [8] C. Vagelopoulos, F. Egolfopoulos, C. Law, Further considerations on the determination of laminar flame speeds with the counterflow twin-flame technique, *Proc. Comb. Inst.* 25 (1994) 1341–1347.
- [9] D. R. Dowdy, D. B. Smith, S. C. Taylor, A. Williams, The use of expanding spherical flames to determine burning velocities and stretch effects in hydrogen/air mixtures, *Proc. Comb. Inst.* 23 (1991) 325–332.
- [10] P. Kumar, T. R. Meyer, Experimental and modeling study of chemical-kinetics mechanisms for H₂-NH₃-air mixtures in laminar premixed jet flames, *Fuel* 108 (2013) 166–176.
- [11] S. Zhou, B. Cui, W. Yang, H. Tan, J. Wang, H. Dai, L. Li, Z. ur Rahman, X. Wang, S. Deng, X. Wang, An experimental and kinetic modeling study on NH₃/air, NH₃/H₂/air, NH₃/CO/air, and NH₃/CH₄/air premixed laminar flames at elevated temperature, *Combust. Flame* 248 (2023) 112536.

- [12] X. Han, Z. Wang, M. Costa, Z. Sun, Y. He, K. Cen, Experimental and kinetic modeling study of laminar burning velocities of NH₃/air, NH₃/H₂/air, NH₃/CO/air and NH₃/CH₄/air premixed flames, *Combust. Flame* 206 (2019) 214–226.
- [13] C. Lhuillier, P. Brequigny, N. Lamoureux, F. Contino, C. Mounaïm-Rousselle, Experimental investigation on laminar burning velocities of ammonia/hydrogen/air mixtures at elevated temperatures, *Fuel* 263 (2020) 116653.

Paper III

DNS of turbulent premixed ammonia/hydrogen flames: the effects of thermo-diffusive instabilities.

Jessica Gaucherand, Davide Laera, Corinna Schulze-Netzer, Thierry
Poinsot

Submitted to Flow, Turbulence and Combustion.

This paper is submitted for publication and is therefore not included.

ISBN 978-82-326-7454-1 (printed ver.)
ISBN 978-82-326-7453-4 (electronic ver.)
ISSN 1503-8181 (printed ver.)
ISSN 2703-8084 (online ver.)



NTNU

Norwegian University of
Science and Technology